# Thermal-hydraulic system evaluation of a natural circulation SMR using accident tolerant fuel


**W Zuidersma**

**orcid.org/0000-0001-8328-4237**


Dissertation accepted for the degree *Master of Engineering* in *Mechanical Engineering* at the North-West University

Supervisor: Prof. Marina du Toit

Co-supervisor: Prof. Martin van Eldik

Graduation: November 2023

# PREFACE

This dissertation marks the culmination of an extensive two-year long journey in the pursuit of knowledge. I would like to thank my supervisor Prof. Marina du Toit, and co-supervisor Prof Martin van Eldik for their contributions to the project. Their mentorship guided me throughout this journey and their insightful feedback and valuable experience helped to shape this project. My sincere gratitude goes to the National Nuclear Regulator (NNR) of South Africa who provided financial support for this project. I would like to thank my family and friends for their support and encouragement during this period. I dedicate this work to my late mother, whose belief in me remains a large driving force, propelling me forward. This dissertation is both a personal milestone and a contribution to academia, and I would like to thank all who contributed to its inception.

# ABSTRACT

A large focus of research in nuclear engineering is on improving the safety of light water reactors (LWRs). This research is driven by high-level nuclear accidents such as the events at Fukushima in March of 2011, among others. The two major factors which contributed to the severity of this accident were the failure of active cooling systems and oxidation of the cladding material which led to hydrogen explosions. Passive safety systems and new reactor concepts are considered to improve passive safety of LWRs. Furthermore, the use of accident tolerant fuel (ATF) is considered to reduce oxidation within the core. A passive LWR will be selected with ATF claddings being applied to the system to evaluate the thermal-hydraulic effects, with the goal of improving safety.

Natural circulation small modular reactors (SMRs) are new reactor concepts designed around passive safety. The naturally circulating primary coolant is only driven by buoyancy forces which improves the passive safety of the reactor for both steady state operation and accident transients. One such reactor called the NuScale SMR is chosen for the current study. A model of the NuScale SMR was developed using ASYST 3.4, a modified RELAP5/MOD3 code. Specifications of the NuScale SMR was taken from the NuScale Final Safety Analysis Report (FSAR) made available by the U.S. Nuclear Regulatory Commission (NRC), as well as previous studies reported in literature. The model was verified for steady state operation and one worst-case scenario accident transient.

The two ATF cladding materials selected for this study was FeCrAl alloy and a SiC composite. Both materials offer improvements in oxidation resistance and failure temperature. FeCrAl has favourable thermophysical properties while having a large neutron absorption cross section which negatively impacts the neutron economy. On the other hand, SiC has a small neutron absorption cross section and a very high melting temperature while having less favourable thermophysical properties.

Results showed that the use of ATF cladding materials in the NuScale SMR model had little effect on the steady state operation of the reactor. Small changes were seen in the peak cladding temperature (PCT) and peak fuel centreline temperature (PFCT) when using FeCrAl and SiC. The worst-case scenario accident transient involves the inadvertent opening of one reactor vent valve (RVV) with subsequent failure of the emergency core cooling system (ECCS) and decay heat removal system (DHRS). In the current model this led to failure of the Zr-alloy cladding after 6.42 h. This grace time was increased with the use of ATF cladding, with FeCrAl and SiC providing an increase of 0.5 h and 4.35 h, respectively.

**Keywords:** NuScale, SMR, RELAP5, ASYST 3.4, modelling, ATF, FeCrAl, SiC.

# TABLE OF CONTENTS

# LIST OF TABLES

# LIST OF FIGURES

# Nomenclature

## List of Acronyms

| | |
|---|---|
| ADS | Automatic Depressurisation System |
| ASYST | Adaptive System Thermal-hydraulics |
| ATF | Accident Tolerant Fuel |
| BDBA | Beyond Design Basis Accident |
| BOC | Beginning of Cycle |
| BWR | Boiling Water Reactor |
| CHF | Critical Heat Flux |
| CNV | Containment Vessel |
| CVD | Chemical Vapour Deposition |
| DHRS | Decay Heat Removal System |
| ECCS | Emergency Core Cooling System |
| EES | Engineering Equation Solver |
| ENSO | Energy Software Services |
| EOL | End of Life |
| FSAR | Final Safety Analysis Report |
| GUI | Graphical User Interface |
| HPC | High Pressure Containment |
| HTC | Heat Transfer Coefficient |
| HTGR | High Temperature Gas-cooled Reactor |
| IAE | Institute of Applied Energy |
| ID | Inner Diameter |
| ISS | Innovative Systems Software |
| LBLOCA | Large Break Loss of Coolant Accident |
| LOCA | Loss of Coolant Accident |
| LOFW | Loss of Feedwater Accident |
| LWR | Light Water Reactor |
| MASLWR | Multi-Application Small Light Water Reactor |
| NGNP | Next Generation Nuclear Plant |
| NPM | NuScale Power Module |
| NPP | Nuclear Power Plant |
| NRC | Nuclear Regulatory Commission |
| OD | Outer Diameter |
| OSU | Oregon State University |
| OTSG | Once Through Steam Generator |
| PCT | Peak Cladding Temperature |
| PFCT | Peak Fuel Centreline Temperature |
| PRHRS | Passive Residual Heat Removal System |
| PWR | Pressurised Water Reactor |
| RCS | Reactor Coolant System |
| RDE | Rod Ejection Accident |
| RHRS | Residual Heat Removal System |
| RPV | Reactor Pressure Vessel |
| RRV | Reactor Recirculation Valve |
| RSV | Reactor Safety Valve |
| RVV | Reactor Vent Valve |
| SBLOCA | Small Break Loss of Coolant Accident |
| SBO | Station Blackout |
| SDTP | SCDAP Development and Training Program |

| | |
|---|---|
| SG | Steam Generator |
| SI | Safe Injection |
| SMR | Small Modular Reactor |
| TRACE | TRAC/RELAP Advanced Computational Engine) |
| UHS | Ultimate Heat Sink |

# CHAPTER 1: INTRODUCTION

## 1.1 Background and rationale

In recent years, a large focus of research in the field of nuclear engineering has been on the safety of nuclear power plants (NPP) and development of various technologies to improve safety. This focus has been driven by high profile nuclear accidents such as the accident at Chernobyl and more recently the accident at Fukushima in Japan. The Fukushima Daiichi NPP has been in operation since the 1970's. The plant consists of six nuclear reactors of the boiling water reactor (BWR) type, meaning the reactor uses a single closed loop where coolant is boiled in the core to create steam which directly drives the steam turbines (IAEA, 2015).

On the 11$^{th}$ of March 2011, a large earthquake occurred off the coast of Japan. Seismic sensors of the Fukushima plant triggered the insertion of the control rods into the reactor cores, which absorb neutrons and stop most fission reactions within the reactor. This reduces the thermal load of the reactor by a large percentage. However, the core still produces residual heat which must be removed for some time before the reactor is deemed safe. For this reason, coolant pumps are used to pump coolant through the core and through external heat exchangers. Shortly after the earthquake, a large tsunami hit the coast of Japan. The tsunami was large enough to breach the flood barrier and enter the facility. This resulted in emergency generators being put out of action. The combination of the earthquake and tsunami eliminated both external power sources and emergency backup generators, which were used to drive the residual heat removal systems (RHRS) (IAEA, 2015).

With the primary coolant pumps no longer available, the emergency core cooling systems (ECCS) were used to remove the residual heat from the core. Water injection into the core commenced through various systems put in place including the ECCS. These systems failed within the first three days of the accident resulting in alternative methods being implemented. Sea water injection began through means of fire pumps. For water injection to take place, the high temperature steam was vented into the primary dry containment as well as the wet well suppression pool. Hydrogen produced from oxidation of Zirconium alloy (Zr-alloy) later accompanied the steam being vented into the primary containment. Attempts were made to vent the primary containment. Due to the station blackout, alternative methods were used for this as well, including compressed air. The primary containment was successfully vented. However, it is believed that blowback occurred to a service floor of the building resulting in a buildup of hydrogen. This led to hydrogen explosions which damaged the containment buildings of the reactors. Further progression of the accident led to complete meltdown of the core of Unit 1 and partial meltdown of the cores of Units 2 and 3 (IAEA, 2015).

To isolate the nuclear fuel from the coolant used within a nuclear reactor, fuel rods are constructed with the fuel pellets being placed within a Zr-alloy tube referred to as cladding. Zr-alloy is the most common fuel cladding material, and it is used because of its high melting point of $\sim$ 2100 K and low neutron absorption properties. The material also has high oxidation resistance at lower temperatures. However, when exposed to high temperature steam the oxidation resistance of the material dramatically decreases. Zr-alloy starts to oxidate in a high temperature steam environment at 1173 K and has a failure point of 1477 K due to this oxidation (Yu *et al.*, 2020). In accident scenarios the temperature within the core can exceed the melting temperature of the material.

Of all nuclear reactors in operation as of 2018, 82 percent are of the LWR type. Of this 82 percent, 66 percent are pressurised water reactors (PWR), and 16 percent are BWRs (Energy Education Canada, 2018). Thus, most nuclear reactors around the world are similar in function to the reactors of the Fukushima NPP. All these reactors have a risk of failure and efforts should be directed to improving the safety in LWRs.

To prevent accidents such as the one in Fukushima, researchers have been focusing on two specific topics. The first topic focusses on the improvement of passive safety systems and completely new reactor designs which provide passive cooling in the case of station blackout and loss of emergency generators. The safety systems at the Fukushima NPP failed within the first three days of the accident. Researchers aim to improve the reliability of these systems. Some reactor concepts rely on natural circulation, even for steady state operation of the reactor, making them inherently safer.

The second topic focusses on the development of accident tolerant fuel (ATF). After failure of the cooling systems at the Fukushima NPP, an increase in temperature within the reactor core occurred. This exposed the nuclear fuel rods to high temperature steam, resulting in the oxidation of the Zr-alloy cladding and production of hydrogen. Further temperature increase resulted in the melting of the fuel rods. Thus, the goals of developing an ATF material are to increase the oxidation resistance of the fuel cladding and increase the melting temperature of both the fuel and the cladding.

## 1.2 Research problem

A problem with operational LWRs such as Fukushima, is that they are prone to accidents which can result in the production of hydrogen and melting of nuclear fuel. This can lead to catastrophic accidents with hydrogen explosions, radioactive releases, and plant write-offs. Although uncommon, these accidents have an unprecedented impact on the economy of the relevant nation and result in large areas of land becoming uninhabitable and thousands of people being displaced from their homes. Accident tolerant fuels and passive safety systems each aim to improve the safety of LWRs. However, as can be seen from literature these countermeasures do not eliminate the risk of LWR failure due to a loss of coolant accident (LOCA) on their own. Thus, a combination of ATF materials with passive cooling systems is needed to further improve the safety of LWRs.

## 1.3 Research aims

The aim of this project is to identify a passive cooling system or a new reactor concept which enhances the passive safety in LWRs. Then identify candidate ATF cladding materials with increased oxidation resistance and melting points. Thermal-hydraulic evaluation of the selected system with the selected ATF cladding materials is to be performed, to evaluate if this combination would greatly increase the safety of LWRs.

## 1.4 Research objectives

1. Identify a passive cooling system or new reactor concept that is designed to improve passive safety in nuclear reactors and can benefit from the use of ATF.
2. Identify prospective ATF claddings with increased oxidation resistance and melting temperature, which could also influence the thermal-hydraulic performance of nuclear reactors.
3. Create a model of the selected system using the thermal-hydraulic system code ASYST 3.4.
4. Perform thermal-hydraulic simulations of the system during steady state operation and accident transients while using Zr-alloy cladding.
5. Verify the accuracy of the model by comparing the simulation results with data gathered from previous studies and test facilities.
6. Apply the selected ATF claddings to the model and repeat the simulations.
7. Evaluate the effects the selected ATF claddings has on the system in terms of the PFCT, PCT and coping time.
8. Draw conclusions on the use of the selected ATF cladding materials in the selected system.

## 1.5 Dissertation layout

1. Introduction.
    - Summary of the background and rationale of the project.
    - Research aims, objectives and dissertation layout.
2. Literature review.
    - Literature review on the topics of ATF, passive cooling systems and new reactor concepts, and modelling methodologies.
    - Identifying candidate ATF cladding materials.
    - Identifying a passive cooling system or new reactor concept and evaluating its behaviour during accident scenarios.
3. Reference model.
    - Detailed description of the model and its development.
    - Verification of the model using Zr-alloy for steady state operation and accident transients.
4. Results and discussion.
    - Results of simulations with ATF claddings compared with the corresponding results for Zr-alloy cladding.
    - Discussion of how the ATF claddings effected the thermal-hydraulic performance of the system.
5. Conclusion.
    - Summary of the findings from the current study.
    - Limitations of the current study and potential topics for future research.

# CHAPTER 2: LITERATUE REVIEW

Safety in nuclear engineering has become a subject of utmost importance in recent years. In this literature study two topics of research in nuclear engineering are explored. Firstly, ATF cladding materials are considered with the goal of identifying candidate ATF cladding materials and their attributes. Secondly, passive safety systems and new reactor concepts are investigated with the goal of identifying a prospective system which could improve the passive safety in LWRs. A third section will focus on the thermal-hydraulic modelling of the selected system.

## 2.1 Accident tolerant fuel

The use of ATF materials in nuclear fuel elements and claddings has many advantages as well as many challenges to overcome. Some of the goals of using ATFs are to increase oxidation resistance, improve heat transfer from the fuel element to the coolant and improve the structural integrity and melting point of the fuel element. The challenges faced with many ATFs are high neutron absorption cross sections, finding reliable manufacturing methods and unwanted mechanical properties such as brittleness.

Of all ATF candidates, traditional Zr-alloy coated with chromium is a highly promising prospect. It has been found that the coating of Zr-alloy with chromium is very successful in terms of chromium adhering to the surface of the Zr-alloy and that this improves the wettability of the cladding which could result in improved thermal-hydraulic performance (Umretiya *et al.*, 2020). Furthermore, the method of manufacturing affects the surface characteristics of the cladding, resulting in an increase in void fraction, heat transfer coefficient (HTC) and critical heat flux (CHF) which leads to better heat transfer (Lee *et al.*, 2021).

ATF cladding material research also focusses on full replacement of the traditional Zr-alloy. FeCrAl alloy cladding and silicon-carbide (SiC) cladding are among the most common in ATF research (Deng *et al.*, 2018; Lee *et al.*, 2019). FeCrAl alloy is promising because of its high oxidation resistance at high temperature and good thermal-hydraulic characteristics resulting in lower PFCT and PCT (He *et al.*, 2019). However, the material has a large neutron absorption cross section, low irradiation resistance and brittleness due to high chromium content making manufacturing difficult (Qiu *et al.*, 2020). SiC fuel claddings are considered for their small neutron absorption cross section, high melting temperature and high oxidation resistance (Qiu *et al.*, 2020). However, the material is also brittle making manufacturing difficult. The material also has a poor HTC which further degrades under irradiation, resulting in higher PFCT and PCT (He *et al.*, 2019).

A major issue in finding ATF cladding replacement materials is the large neutron absorption cross sections found in many materials which would otherwise be suitable for this purpose. An investigation was done into the safety features of PWR fuel assemblies using Zr-alloy as well as the candidate ATF cladding materials SiC, FeCrAl and stainless steel 310 (SS-310) from a neutronics perspective. The microscopic thermal neutron absorption cross section of these materials can be seen in Table 2-1. Simulations done using the MCNPX code shows that the larger neutron absorption cross sections of SS-310 and FeCrAl results in a decrease in K-infinity, while the smaller neutron absorption cross section of SiC increases K-infinity. A decrease in K-infinity results in the shortening of the fuel cycle length. The use of SS-310 and FeCrAl resulted in a 26.5 % and 21.3 % reduction in end of life (EOL) burnup, respectively, while the use of SiC increased the EOL burnup by 2.23 % (Mustafa, 2021).

**Table 2-1: Microscopic thermal neutron absorption cross section of ATF cladding materials (Mustafa, 2021)**

| Material | Density ($g/cm^3$) | Absorption cross section (barn) |
|---|---|---|
| SiC | 2.58 | 0.086 |
| Zr-alloy | 6.56 | 0.2 |
| FeCrAl | 7.1 | 2.43 |
| SS-310 | 8.03 | 3.21 |

A study was done on the properties and irradiation effects of SiC/SiC composites. These materials are made of SiC fibres embedded in a SiC matrix, with a pyro carbon (PyC) interphase between the matrix and fibres. These SiC/SiC composites are considered for their increased resistance to high radiation environments compared to other SiC composites. Results still show a decrease in the thermal conductivity of all the SiC/SiC composites tested because of neutron irradiation while there was no change in specific heat capacity. Minor effects with swelling, thermal expansion and Youngs modulus was also observed (Katoh *et al.*, 2014).

A thermal hydraulic evaluation was done comparing FeCrAl and SiC cladding as well as various ATF fuel pellet materials in a CPR1000 system during various accident transients. Results show that there is an insignificant change in temperature by using ATF in most cases. However, during a small break LOCA (SBLOCA) without safe injection (SI), Zr-alloy cladding would reach its failure temperature of 1477 K after 3690 s. FeCrAl cladding extended this time by 310 s or 8.4 %, with a failure temperature of 1773 K, while SiC did not reach its failure temperature in the simulation time. For this study SA3/PyC150-A SiC/SiC composite was considered both in unirradiated and irradiated form. The thermal conductivity of this SiC/SiC composite as a function of temperature can be seen in Figure 2-1. After irradiation, the thermal conductivity decreases to a near constant value. The thermal conductivity of Zr-alloy and FeCrAl claddings are also given in Figure 2-1. Although SiC/SiC composites have a lower thermal conductivity than Zr-alloy, the specific heat capacity is much higher as can be seen in Figure 2-2. The failure points of the ATF materials used in this study are shown in Figure 2-3 (Yu *et al.*, 2020).

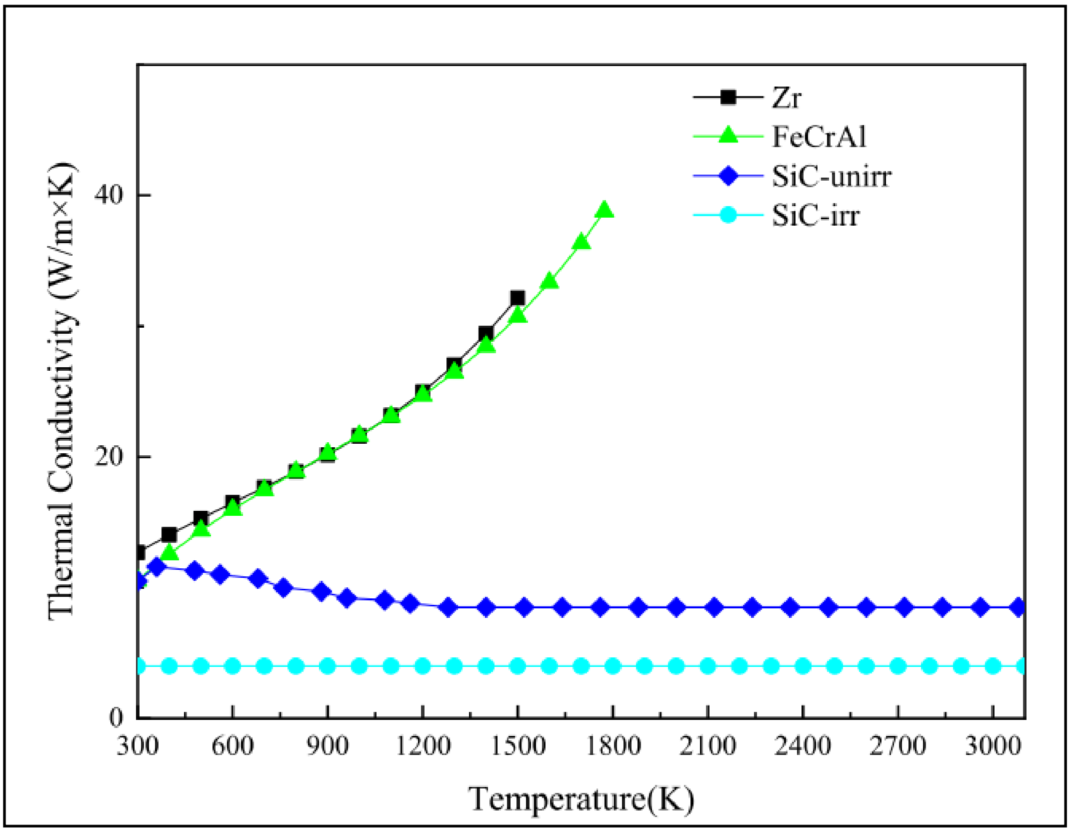


**Figure 2-1: Thermal conductivity of ATF cladding materials (Yu *et al.*, 2020)**

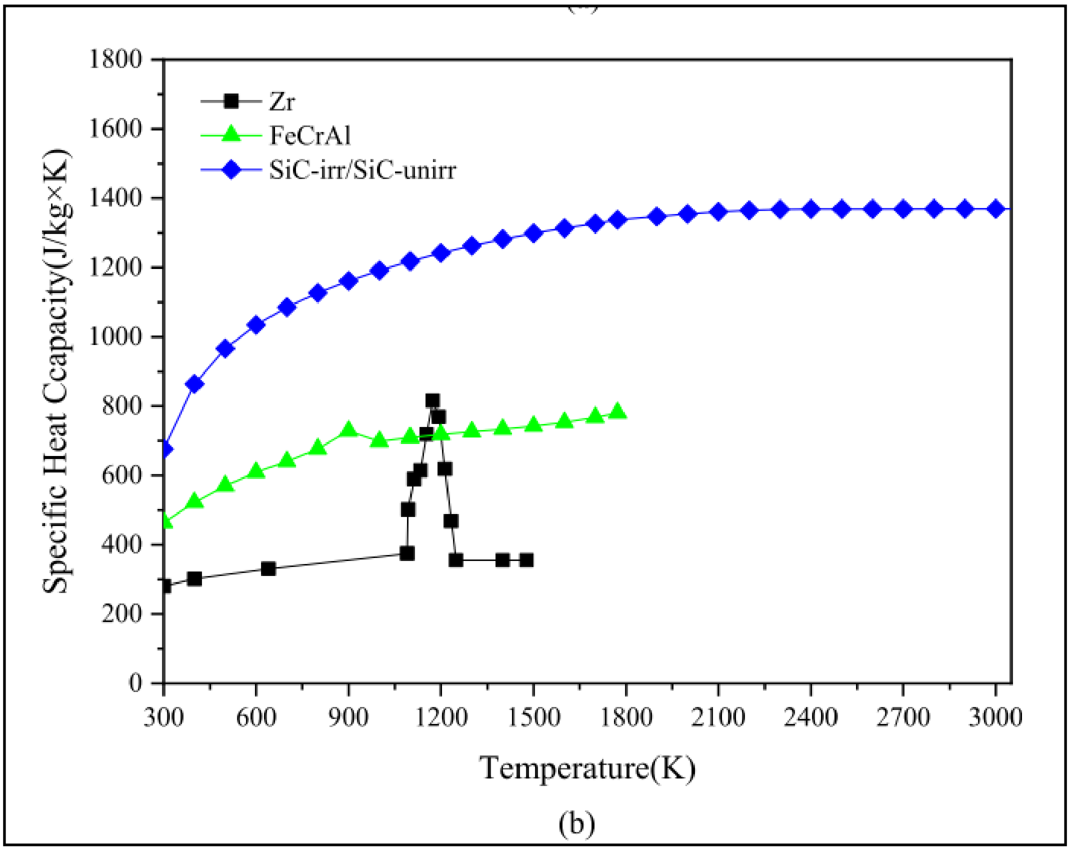


**Figure 2-2: Specific heat capacity of ATF cladding (Yu *et al.*, 2020)**

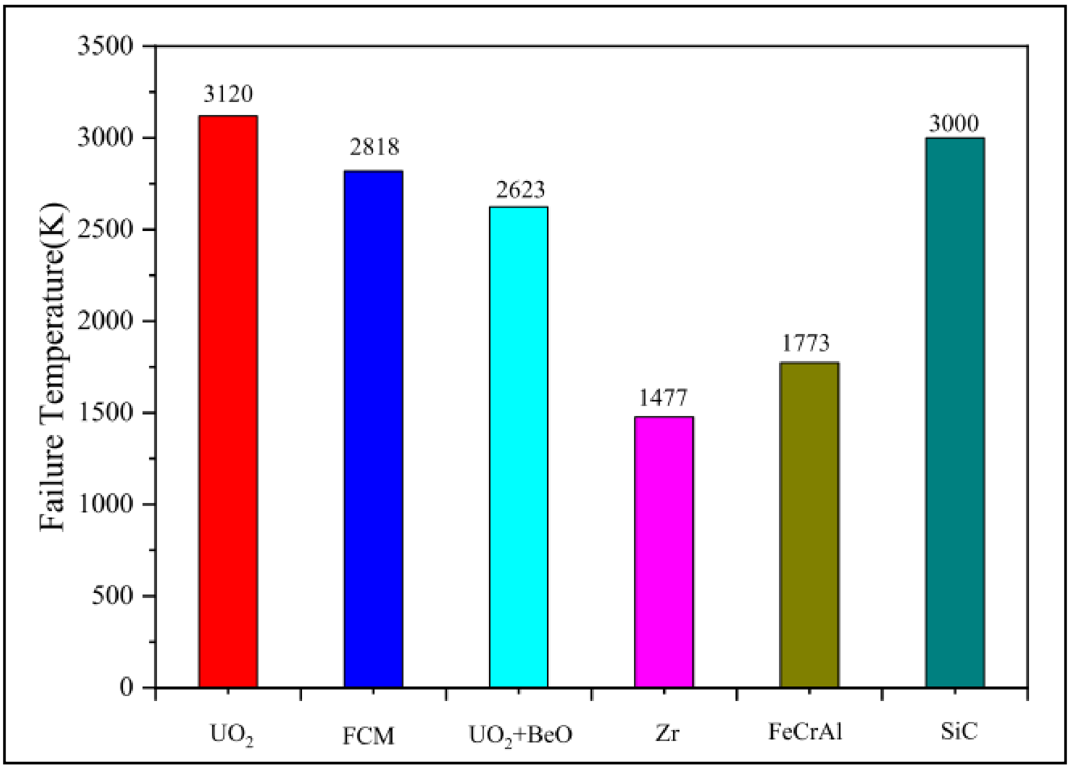


**Figure 2-3: Failure point of ATF materials (Yu *et al.*, 2020)**

The density of the SA3/PyC150-A SiC/SiC composite is uncertain due to the difference in density of the materials used in the composite. A density-temperature correlation for this material is not available, thus the density is assumed to be constant at 2.58 g/cm$^3$ (Katoh *et al.*, 2014).

ATF materials aim to improve the safety of PWRs. FeCrAl alloy cladding and Cr-coated Zr-alloy were compared with bare Zr-alloy in terms of oxidation, hydrogen production and coping time in beyond design basis accidents (BDBAs) namely large break LOCA, short term station blackout (SBO) and long term SBO. FeCrAl cladding and Cr-coated Zr-alloy cladding showed much less oxidation, resulting in lower hydrogen production. During large break LOCA without safety injection the calculated coping time for Zr-alloy cladding was 140 s while Cr-coated Zr-alloy and FeCrAl alloy claddings improved the coping time by 57 and 87 s, respectively. The coping time of Zr-alloy cladding during short term SBO was 53.4 minutes while Cr-coated Zr-alloy and FeCrAl alloy claddings improved the coping time by 1.1 and 5.5 minutes, respectively. Finally for long term SBO the coping time of Zr-alloy cladding was 3.3 h. This was improved by 6.5 minutes using Cr-coated Zr-alloy cladding and 32.4 minutes with FeCrAl alloy cladding (Gurgen and Shirvan, 2018).

## 2.2 Passive cooling systems

Many safety systems have been developed to improve the safety of nuclear reactors. The goal of many of these systems is to remove decay heat from the reactor core in the case of a reactor shut down due to a LOCA. In many cases these systems are the last safety measures used to prevent core damage or meltdown. Examples of passive systems used in conventional PWR reactors are residual heat removal systems (RHRS), condensation heat exchangers, safety injection systems, accumulators and suppression pools (Porhemmat *et al.*, 2016; Sun *et al.*, 2017; Wu *et al.*, 2020).

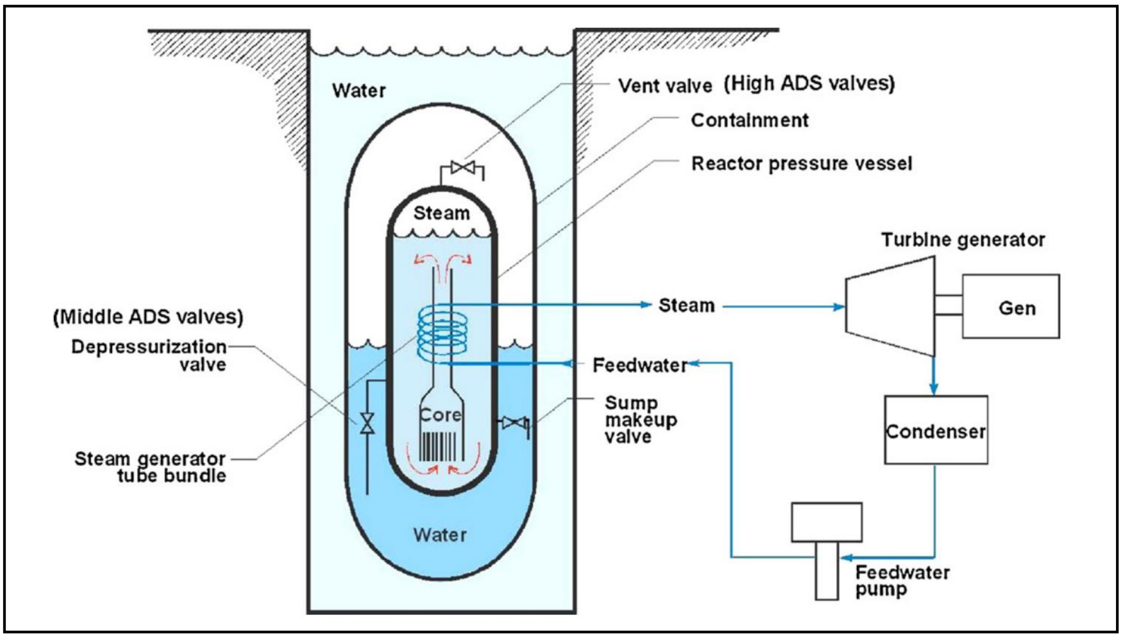


**Figure 2-4: MASLWR conceptual layout (Butt *et al.*, 2016)**

However, in recent years a new generation of reactors have been developed that are less dependent on the above-mentioned safety systems. These are new reactor concepts that are compact, modular, and designed around passive cooling systems. These reactors are referred to as small modular reactors (SMR) (Butt *et al.*, 2016; Fakhraei *et al.*, 2021; Skolik *et al.*, 2021). One such reactor design, known as the multi-application small light water reactor (MASLWR), can be seen in Figure 2-4.

### 2.2.1 MASLWR

The MASLWR is a sump natural circulation SMR which relies on buoyancy forces for coolant flow in the primary loop for steady state operation and for decay heat removal during accident scenarios. The MASLWRs reactor pressure vessel (RPV) contains the core, hot leg chimney, steam generators and pressurization space. The RPV is situated in a containment vessel (CNV), partially filled with water. The CNV provides pressure suppression and water makeup through valves connected to the RPV. Finally, the CNV is submerged in a pool of water which acts as a heatsink.

The MASLWR is a conceptual PWR with an electrical output of 35 MW (150MW thermal) and a modular design. A test facility for the MASLWR located at Oregon State University (OSU) is used to evaluate the MASLWR under full power operating conditions and to evaluate the safety features of the MASLWR under accident transiens. Two accident scenarios were tested, one design basis accident namely inadvertent opening of the middle Automatic Depressurisation system (ADS) blowdown valve and one beyond design basis accident namely inadvertent opening of the high ADS vent valve. In both these cases actuation of the remaining valves and condensation and natural circulation between the vent valve and sump makeup valve through the containment was adequate to keep the core covered for the length of the transients (Reyes *et al.*, 2007).

Tests of the passive safety systems of the MASLWR were conducted, with the worst-case scenario being inadvertent opening of ADS blowdown valve with subsequent failure of the vent valve. Actuation of the vent valve is critical for ventilation of steam created by core decay heat and to allow coolant from the sump to re-enter the reactor pressure vessel. Natural circulation should take place between the vent valve and sump makeup valve. In this worst-case scenario accident, the coolant level within the RPV decreases until the core is uncovered, resulting in a large increase in temperature of fuel elements (Butt *et al.*, 2016).

### 2.2.2 CAREM-25

Another SMR design is the CAREM-25. This reactor is very similar in layout to the MASLWR, with the core, chimney, steam generators, pressuriser and downcomer all located within the RPV. The reactor does however differ slightly in function where the natural circulation is flashing-driven, meaning the temperature and pressure in the RPV allows the water to flash to steam in the chimney promoting natural circulation. A study was done investigating flow instabilities within the reactor for steady state and low power start up transients. It was found that flow instabilities occurred at low pressure during start up in the area from the top of the core to the midpoint of the chimney. It was also found that condensation in the steam dome has an effect on the flow stability and this could be used to improve stability by increasing the pressure of the system (Marcel *et al.*, 2013).

Another study investigated flow phenomena related to the operation of the CAREM-25 reactor also applicable to other natural circulation SMR designs. Achieving adequate mass flow rates is necessary to maintain acceptable thermal margins. Condensation on the reactor structures and the steam dome also plays an important role. These phenomena result in the reactor dynamics of the CAREM-25 and other SMRs to be much different from traditional PWRs. The layout of the SMR can be seen in Figure 2-5 (Marcel *et al.*, 2013).

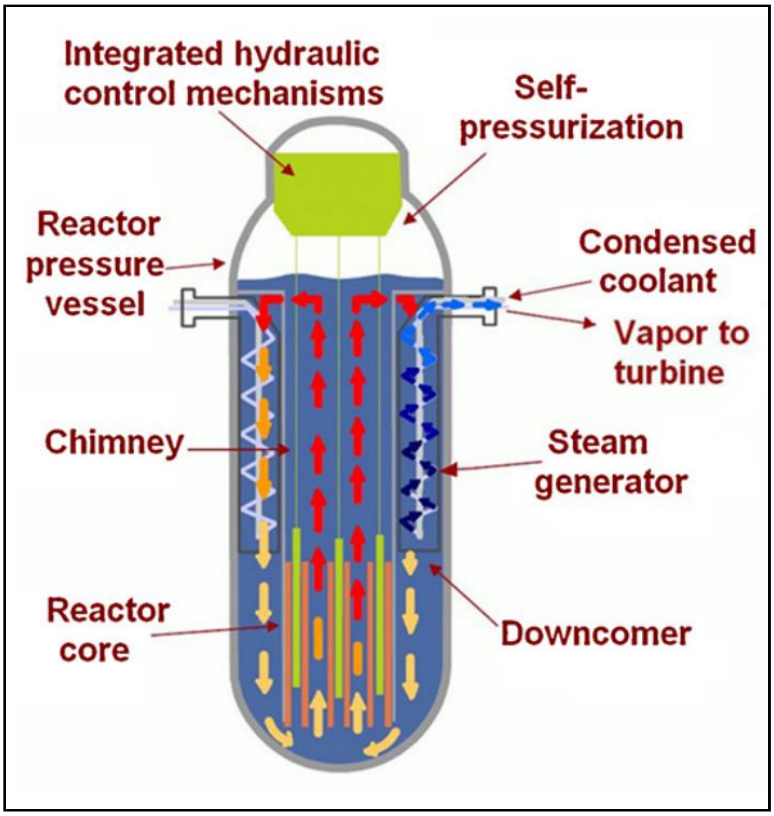


**Figure 2-5: CAREM-25 SMR layout (Marcel *et al.*, 2013)**

### 2.2.3 IP100

The IP100 reactor, like the CAREM-25 reactor, is a conceptual flashing driven natural circulation SMR. The safety of this reactor was evaluated against a loss of feedwater (LOFW) accident. It was found that the IP100 has excellent safety during a partial LOFW where 75 % of the once through steam generator (OTSG) groups were disabled. During a full LOFW accident the passive residual heat removal system (PRHRS) can provide adequate cooling capability for nine hours. Other improvements can also be made to prevent pressure and temperature spikes such as increasing the pressuriser volume and PRHRS area (Zhao *et al.*, 2020). The IP100 also experiences flow instabilities as with the CAREM-25. Flow instabilities occur during low load transients such as start up. These flow instabilities can largely be mitigated by increasing the pressurisation space volume and steam header volume and choosing a spray flow rate to control the maximum pressure in the RPV. The IP100 SMR is illustrated in Figure 2-6 (Zhao *et al.*, 2019).

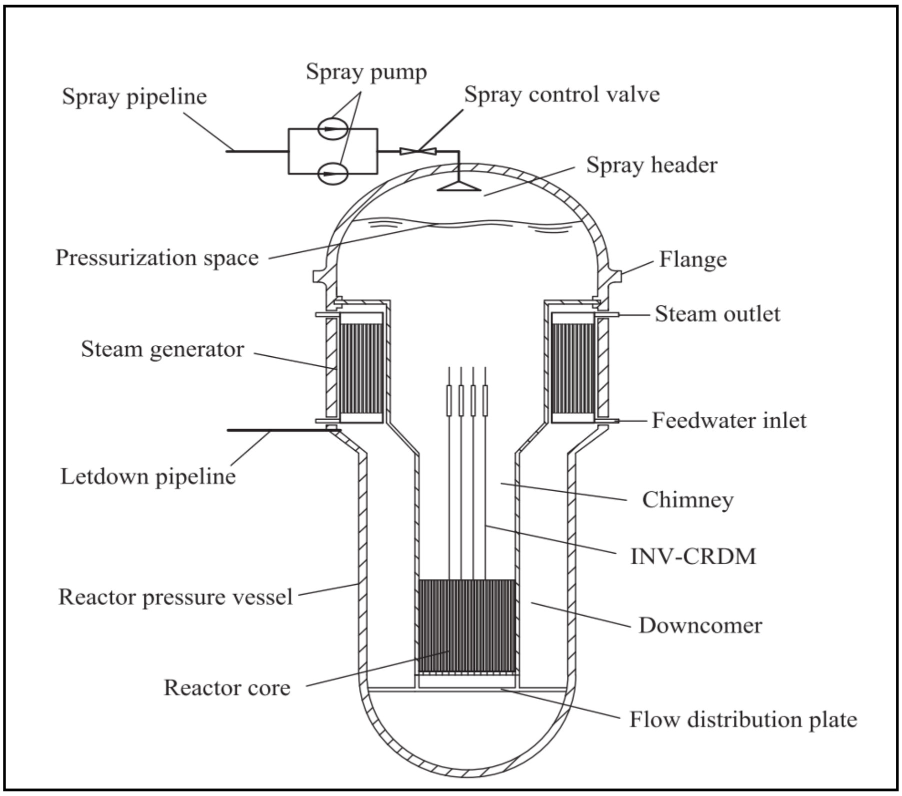


**Figure 2-6: IP100 SMR illustration (Zhao *et al.*, 2019)**

### 2.2.4 NuScale SMR

The NuScale Power Module (NPM) is a SMR with an electrical output of 50 MW (160 MW thermal) and utilizes a similar design to other natural circulation light water SMRs, with the addition of safety systems namely the emergency core cooling system (ECCS) and decay heat removal system (DHRS). The NuScale SMR is one of the most promising SMR designs, with the SMR receiving standard design approval from the U.S. NRC (US NRC, 2020). A cutaway view of the NPM can be seen in Figure 2-7.

The NPM is similar in design to the MASLWR where the RPV houses the core, riser (hot leg chimney), downcomer, steam generators and pressuriser. The RPV is situated in a larger CNV. Unlike the MASLWR the CNV does not contain any water and is placed under vacuum during normal operation. The CNV is partially submerged in the reactor pool which acts as ultimate heat sink (UHS). The ECCS consists of three reactor vent valves (RVV) located at the top of the pressuriser and two reactor recirculation valves (RRV) located on the side of the RPV just above the core. The function is similar to the ADS and sump makeup valves found in the MASLWR. During accident scenarios steam is released from the RVVs and condenses in the CNV. Condensate flows downward and is allowed to re-enter the RPV through the RRVs. The DHRS is a natural circulation heat exchanger which consists of a heat exchanger located on the outside of the CNV in the UHS and is connected to the steam generator coils.

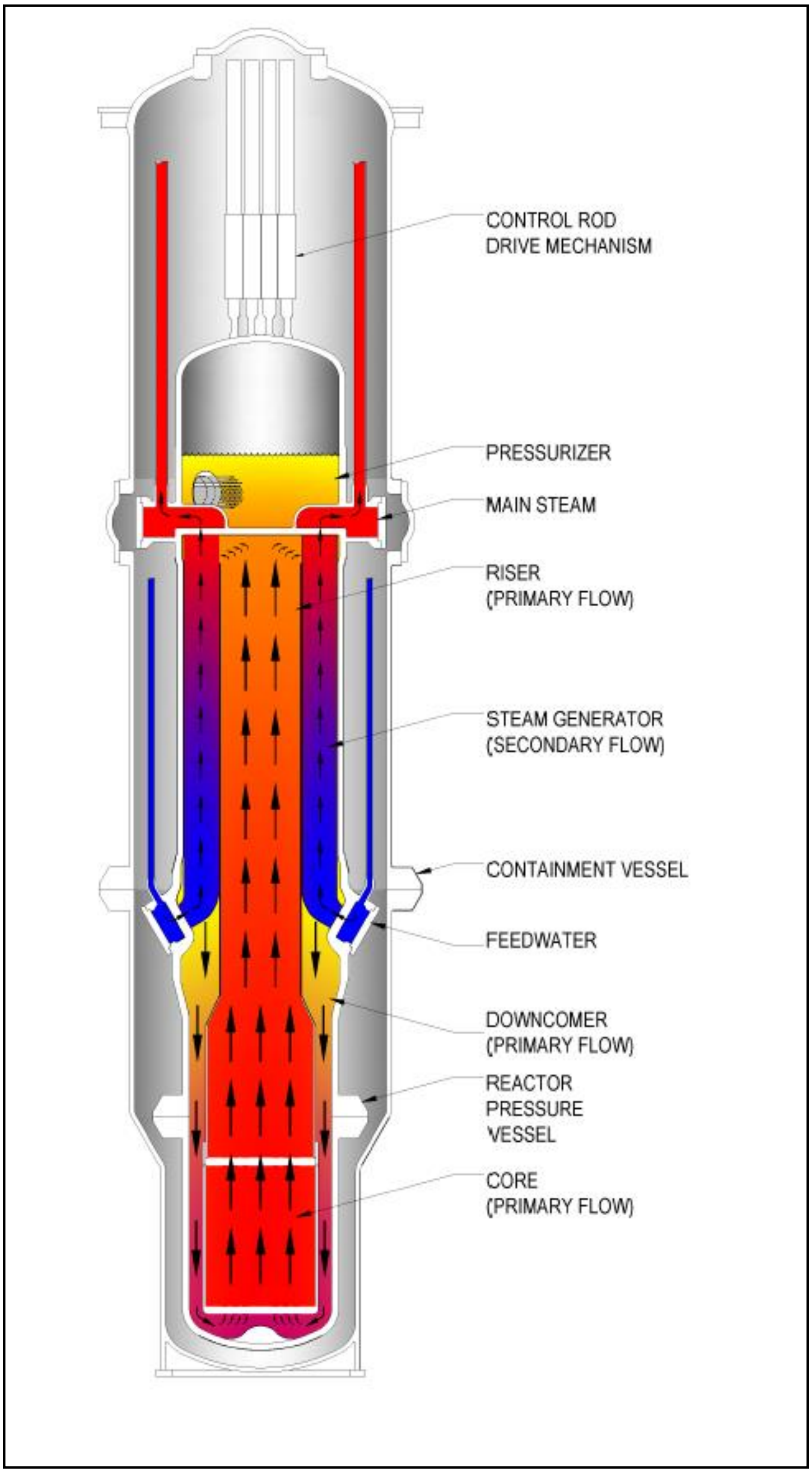


**Figure 2-7: Cutaway view of NuScale Power Module (NuScale Power LLC., 2020a)**

Assuming all the components of the NPM are functional, a SBO transient would progress as follows. The transient would be initiated by a loss of AC power to the power plant. This results in turbine trips and loss of feedwater in the secondary loop. With the loss of this heat removal from the RPV the pressure and temperature increases. A high-pressure signal results in a reactor trip, decreasing the power in the core from full load to decay power. Pressure in the RPV continues to increase until it reaches the first reactor safety valve (RSV) setpoint. The RPV depressurizes into the containment through the RSV. The SG coils are isolated from the secondary loop and the DHRS valves are actuated, connecting the DHRS heat exchanger to the SG coils. The depressurisation of the RPV and operation of the DHRS decreases the pressure and temperature in the primary loop leading to an increase in density of the coolant and a reduction in the coolant level, where the coolant level in the pressurizer will reach zero within a few hours from the start of the transient. Heat removal by the DHRS continues, resulting a decrease in pressure and coolant level in the RPV to the point where the level reaches the top of the riser. This cuts off most of the flow from the riser to the downcomer and heat removal by the DHRS is reduced. After 24h from the reactor trip the ECCS actuates the three RVVs and two RRVs. The fluid inventory from the RPV enters the CNV and pressure and coolant level between the RPV and CNV equalises. Coolant in the CNV is continuously cooled by the UHS pool through the CNV walls. Coolant flows back into the RPV through RRVs where it removes decay heat from the core and produces vapor. Vapor escapes the RPV through the RVVs and condenses on the CNV walls. This process continues to remove decay heat from the core for the remainder of the transient (Fakhraei *et al.*, 2020).

An evaluation of flow phenomena of the NuScale SMR during accident transients was conducted. Like some other SMR designs, flow instabilities were observed during a SBO accident transient. Flow instabilities start when the coolant level in the RPV reaches the top edge of the riser and flow is cut off between the riser and downcomer. The reduction in mass flow through the core and remaining decay power of the core causes density waves through the riser resulting in mass flow oscillations, temperature spikes and vibrations in the RPV, which could lead to structural damage in the steam generators and core assemblies. Changes that could be made to mitigate these flow instabilities are a safety injection system, which increases the coolant level to re-enable flow between the riser and downcomer, and valves between the riser and downcomer halfway along the steam generator which allows for adequate flow from the riser to the downcomer. These changes allow for the DHRS to effectively remove decay heat from the RPV for 72 h without activation of the ECCS (Fakhraei *et al.*, 2021)

One study performed an analysis on the NuScale SMR using RELAP/SCDAPSIM code. A model was developed using publicly available data found in the NuScale FSAR provided by the U.S. NRC (NuScale Power LLC., 2020b, 2020c, 2020d). A worst-case scenario accident was analysed which was an inside containment LOCA with subsequent failure of the ECCS and DHRS. The transient was initiated by an inadvertent opening of a RVV resulting in depressurisation of the RPV into the CNV. A low-pressure signal caused the reactor to trip, resulting in the insertion of control rods into the core. However, decay heat from the core continued heating the coolant in the RPV, gradually boiling it away into the CNV. The failure of the ECCS meant no other RVVs or RRVs opened to allow for coolant recirculation back into the RPV. SG coils were isolated from the secondary loop on the low-pressure signal, but the valves connecting the SG coils to the DHRS heat exchangers were assumed to fail. With no decay heat removal from the RPV and no coolant recirculation, the coolant level in the RPV gradually decreased until the core became uncovered. This resulted in core damage after 4.8 h from the start of the transient (Skolik *et al.*, 2021).

## 2.3 Modelling methodologies

Detailed thermal-hydraulic modelling of components and systems is not always possible. Many components in nuclear reactors such as steam generators and core fuel assemblies have intricate geometries which are outside of the capabilities of conventional thermal-hydraulic codes used in nuclear research. Furthermore, detailed modelling of intricate components of nuclear reactors comes with large penalties in processing power and time. For these reasons different modelling methodologies are implemented to simplify components and systems while maintaining an adequate level of accuracy.

### 2.3.1 Core

Erfaninia *et al.* (2017) used neutronic-thermal hydraulic coupling to analyse fuel channels and power distribution of a flashing driven natural circulation SMR called CAREM-25. A neutronic-thermal hydraulic coupling analysis of hot and average fuel channels was conducted for both hexagonal and square fuel assemblies using the neutronics code MCNPX (Los Alamos National Laboratory, 2023) and the thermal-hydraulics code CFX (Ansys, 2023). Due to symmetry of the core layout, smaller sections of the core could be considered as can be seen in Figure 2-8. MCNPX was used to determine the radial power peaking factors as seen in Figure 2-8, as well as the axial power peaking factors of 16 equally sized zones along the length of the fuel assemblies. From the radial power peaking factors, hot and average channels were determined. MCNPX was externally coupled to CFX to exchange data. This is different from internal coupling where the neutronics code is integrated into the thermal-hydraulics code. CFX was used to perform thermal-hydraulic calculations for the hot and average channels for 16 equally sized axial zones. Data from the CFX calculations was returned to MCNPX for further neutronics calculations. This process was repeated until the axial temperature distribution of the fuel centreline and the coolant along the fuel channels converge. The central fuel assemblies were determined to be the hottest channel of the proposed SMR core, with power peaking factors of 1.778 and 1.674 for the hexagonal and square fuel assemblies, respectively. Results show that the maximum axial power peaking factor along the length of the fuel rod occurred just under the mid plane of the rod as can be seen in Figure 2-9.

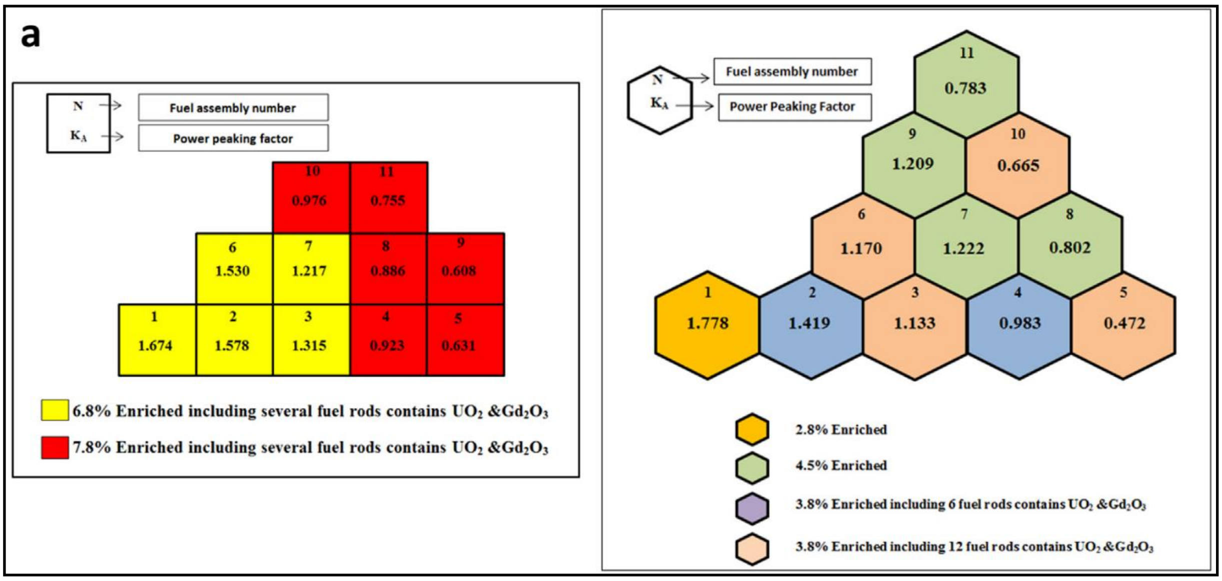


**Figure 2-8: Power peaking factors of proposed SMR fuel assemblies (Erfaninia *et al.*, 2017)**

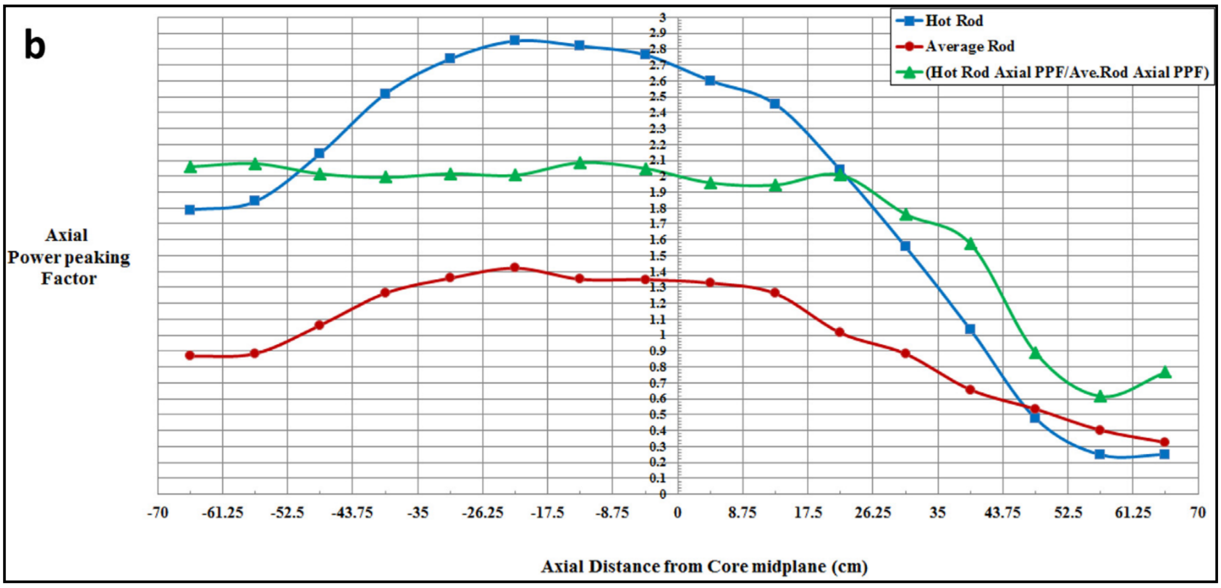


**Figure 2-9: Axial power peaking factors of hot and average fuel rod in hexagonal fuel assemblies (Erfaninia *et al.*, 2017)**

Using RELAP5 (Idaho National Engineering Laboratory, 1995), a study of a rod ejection accident (RDE) at hot zero power in a PWR was conducted. The PWR modelled was a 3411 MW (thermal) four loop Westinghouse reactor. The core of the reactor was simplified in the RELAP5 model with a hot channel representing the single hottest fuel assembly and an average channel representing all 192 other fuel assemblies. It is stated that a bypass channel was not modelled because no natural circulation was assumed. The RELAP5 reactor kinetics model was used to determine the power generation over time including core feedback effects such as Doppler reactivity and moderator reactivity (El-Sahlamy *et al.*, 2022). The nodalisation used in this study can be seen in Figure 2-10 with the following components and modelling approaches:

- 328 – Lower plenum – Time dependant volume.

- 330 – Lower assembly nozzle – Single volume.
- 336 – Core hot channel – Pipe.
- 335 – Core average channel – Pipe.
- 340 – Assembly exit – Single volume.
- 345 – Upper plenum – Time dependant volume.

Time dependent volumes were used to control the boundary conditions at the inlet and outlet of the core. The fuel channels were modelled as pipe sections with equivalent flow area and hydraulic diameter. Each pipe section was divided into 13 axial nodes. A heat structure representing the fuel elements was connected to each of the fuel channels and had 12 axial nodes and 17 radial nodes. The axial power distribution of the core had a cosine shape (El-Sahlamy *et al.*, 2022).

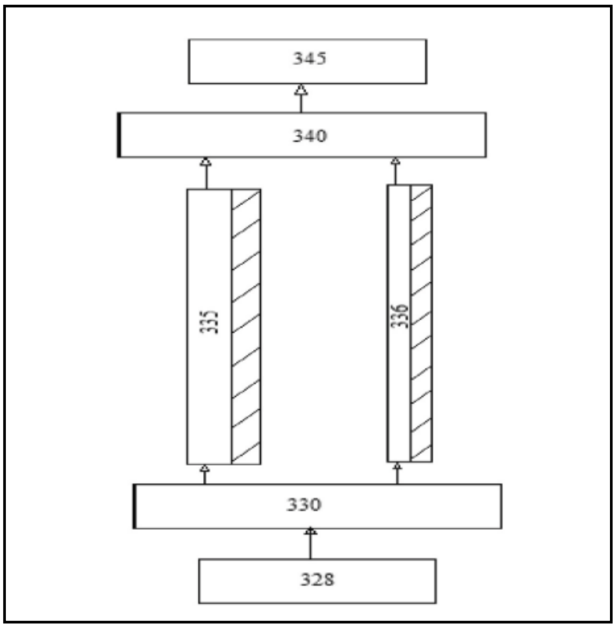


**Figure 2-10: RELAP5 model of four loop Westinghouse PWR core (El-Sahlamy *et al.*, 2022)**

In another study, modelling of the NuScale SMR was conducted with data gathered from the NuScale FSAR. RELAP5/SCDAPSIM code was used in this instance. Data gathered from the FSAR included geometrical data for the RPV, an in-depth description of the core and steam generator, parameters for the primary and secondary loop for steady state and transient analysis, a description of the instrumentation and control systems and general information on safety systems. However, the authors had to assume details such as the geometry of the DHRS, the CNV dimensions, the pressurizer heater bundle dimensions and location, the precise location of valves, and the reactor coolant pool and reactor building dimensions, as these parameters were not given by the FSAR. The nodalisation can be seen in Figure 2-11 (Skolik *et al.*, 2021).

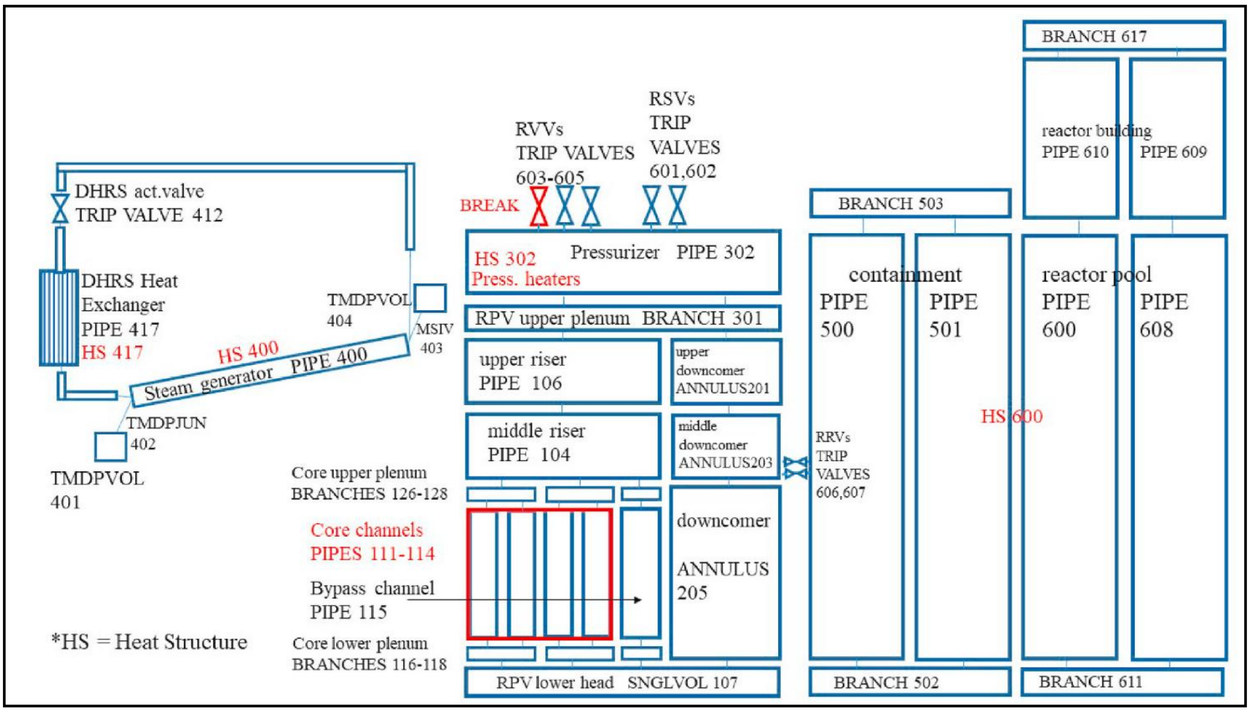


**Figure 2-11: RELAP5 model of NuScale SMR (Skolik *et al.*, 2021)**

The core was modelled with five channels: the hot channel (111) consisting of a single fuel assembly, three average channels (Channels 112, 113, and 114) consisting of eight, twelve, and sixteen fuel assemblies, respectively. Additionally, there is a bypass channel (Channel 115) with no power generation. The power factor for each of these channels was calculated from the fuel assembly power factors of the NuScale core at beginning of cycle (BOC) as taken from the NuScale FSAR and shown in Figure 2-12. The relative power and other specifications of the fuel channels are shown in Table 2-2 (Skolik *et al.*, 2021).

| | | | | | | |
|---|---|---|---|---|---|---|
| | | 0.895 | 0.911 | 0.888 | | |
| | 1.033 | 1.137 | 0.957 | 1.135 | 1.033 | |
| 0.888 | 1.135 | 1.054 | 0.967 | 1.054 | 1.136 | 0.895 |
| 0.911 | 0.957 | 0.967 | 1.091 | 0.967 | 0.957 | 0.911 |
| 0.895 | 1.136 | 1.054 | 0.967 | 1.054 | 1.135 | 0.888 |
| | 1.033 | 1.135 | 0.957 | 1.137 | 1.033 | |
| | | 0.888 | 0.911 | 0.895 | | |

**Figure 2-12: NuScale fuel assembly power factors at BOC (Skolik *et al.*, 2021)**

**Table 2-2: NuScale fuel channel RELAP5 model specifications (Skolik *et al.*, 2021)**

| Core active channels 111 – 114 and bypass channel 115 | | | | | |
|---|---|---|---|---|---|
| **Channels** | **111** | **112** | **113** | **114** | **115** |
| Flow area ($m^2$) | 0.02595 | 0.2076 | 0.3114 | 0.4152 | 0.084 |
| Coolant mass flow (kg/s) | 13.5 | 112.1 | 175.1 | 223.8 | 42.5 |
| Hydraulic diameter (m) | 0.011 | 0.011 | 0.011 | 0.011 | 0.22 |
| Number of fuel assemblies | 1 | 8 | 12 | 16 | - |
| Number of fuel rods | 264 | 2112 | 3168 | 4224 | - |
| Relative power | 1.091 | 1.0105 | 1.0762 | 0.93175 | - |
| Power fraction | 0.0296 | 0.2185 | 0.349 | 0.4029 | - |
| Heat exchange area ($m^2$) | 15.91 | 127.28 | 190.92 | 254.56 | - |

The relative power of the hot channel is the power factor of the centre fuel assembly, while the relative powers of the three average fuel channels were calculated as the average of the power factors of the fuel assemblies surrounding the hot channel, starting with the eight assemblies surrounding the centre assembly and moving outward in concentric rings. There was no heat transfer between fuel channels or the fuel channels and the downcomer. There was also no heat transfer between the RPV and CNV. Heat structures were used for heat transfer between the downcomer and steam generator as well as the CNV and reactor pool. Heat structures were also used for the pressurizer heating elements and DHRS heat exchanger. The thermal-hydraulic components of RELAP5 were used to model the primary loop, CNV, UHS and partial secondary loop, while the core components of SCDAP were used to model the fuel elements and control rods (Skolik *et al.*, 2021).

A different approach to model the NuScale SMR was followed in a study evaluating the safety of the NuScale SMR during a SBO accident using RELAP5/SCDAP (Innovative Systems Software, 2023) code. The nodalisation can be seen in Figure 2-13. The model contained two active channels. The hot channel (110P) consisted of 1 fuel assembly and the average channel (100P) consisted of the remaining 36 fuel assemblies. The model had three bypass channels making up 8.5 % of the total flow. This included flow through the guide tubes, instrument tube and cooling flow through the reflector. Channels 120P and 130P were bypass channels while the channel 140P represented cooling flow through the reflector. Heat structures existed between the active and bypass channels as well as between the average channel and the reflector coolant channel, and between the reflector coolant channel and the downcomer (Fakhraei *et al.*, 2020).

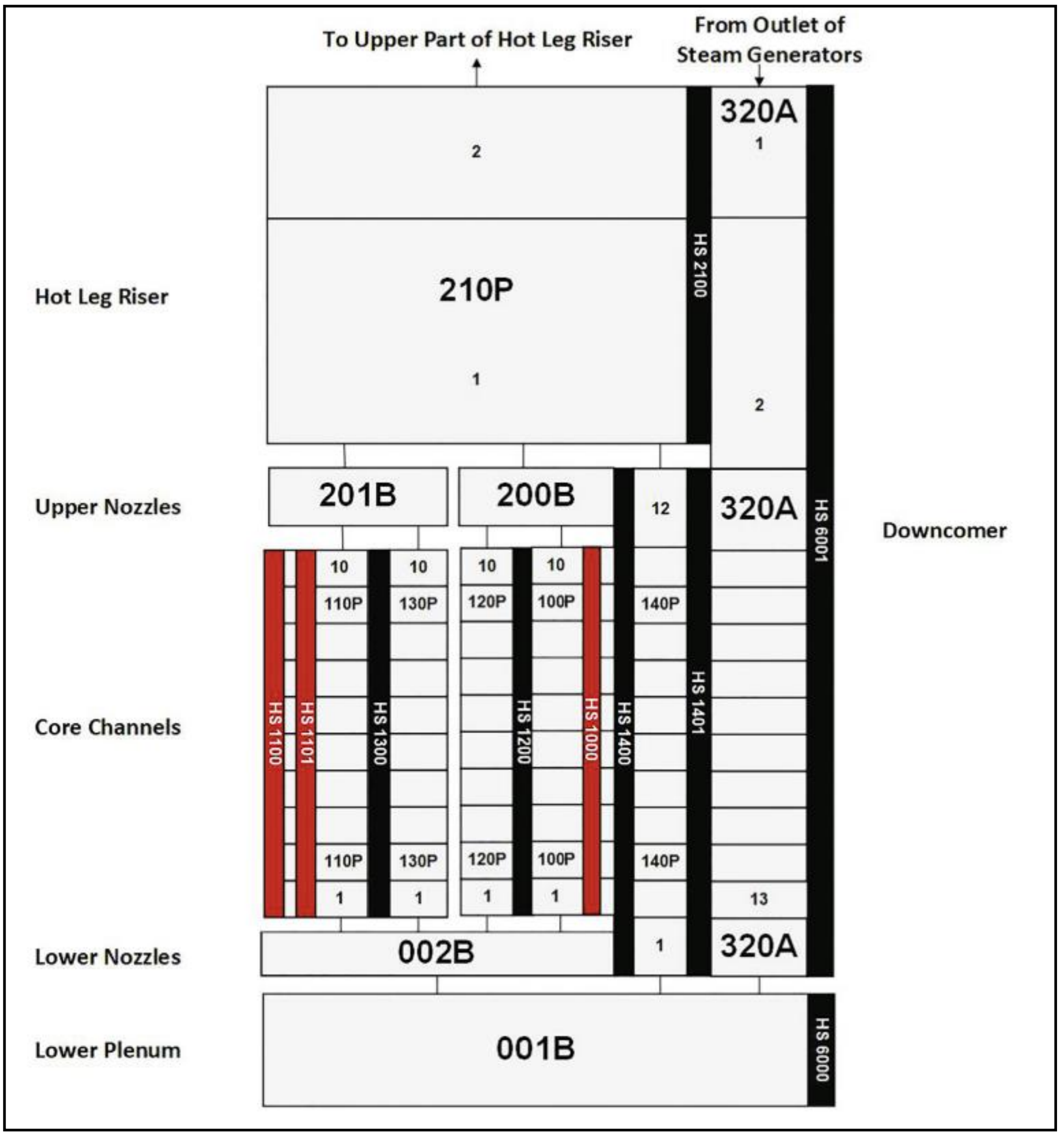


**Figure 2-13: RELAP5 model of NuScale SMR (Fakhraei *et al.*, 2020)**

Power peaking factors and other neutronic parameters were determined using the MCNP5 code (Los Alamos National Laboratory, 2023) from the proposed core loading pattern shown in Figure 2-14(a). The reference design loading pattern is shown in figure Figure 2-14(b).The heat structures representing fuel elements consisted of ten axial nodes with axial power distributions as can be seen in Figure 2-15. The power distribution was given as a fraction of the total core power. The heat structures were also divided in to ten radial nodes to achieve an accurate temperature gradient (Fakhraei *et al.*, 2020).

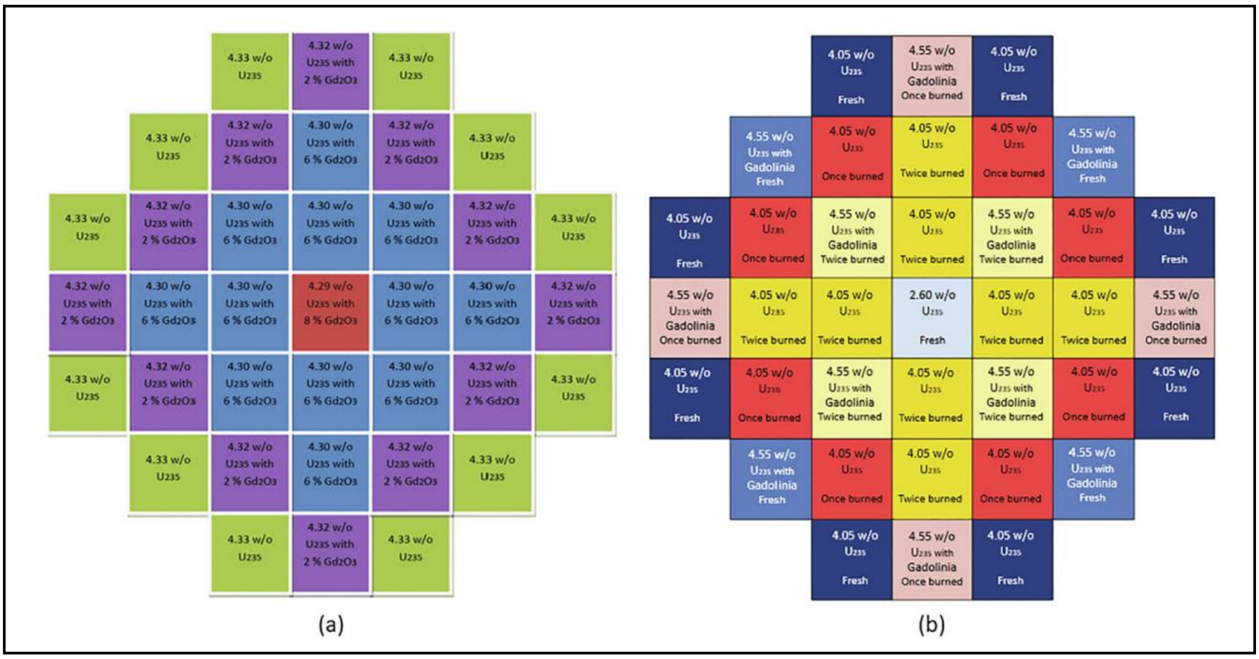


**Figure 2-14: (a) proposed loading pattern for NuScale (b) loading pattern of reference design (Fakhraei *et al.*, 2020)**

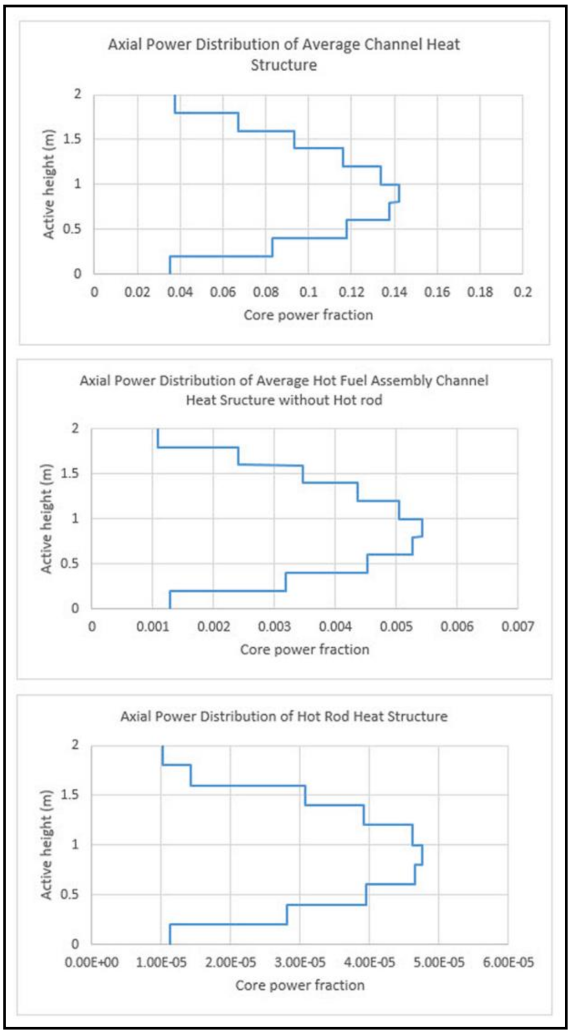


**Figure 2-15: Axial power distribution of core heat structures (Fakhraei *et al.*, 2020)**

### 2.3.2 Steam generator

Helical coil steam generators are in many cases the favoured method of heat transfer between the primary and secondary loops of next generation nuclear plants (NGNP). Helical coil steam generators provide increased heat transfer in a compact design with high levels of safety and reliability. As part of the evaluation of these SGs a once-through, shell and tube, modular high temperature gas-cooled reactor (HTGR) steam generator was modelled using RELAP5-3D (Idaho National Laboratory, 2023). As illustrated in Figure 2-16, helium enters the SG through a cross duct where it then flows downward through the central pipe. The gas is redirected at the lower plenum and flows upward through the annulus where it meets the helically wound tube bundles and flows out through the cross duct. On the secondary side feedwater enters from the bottom, flows upward through the tube bundles, and exits at the top (Hoffer *et al.*, 2011).

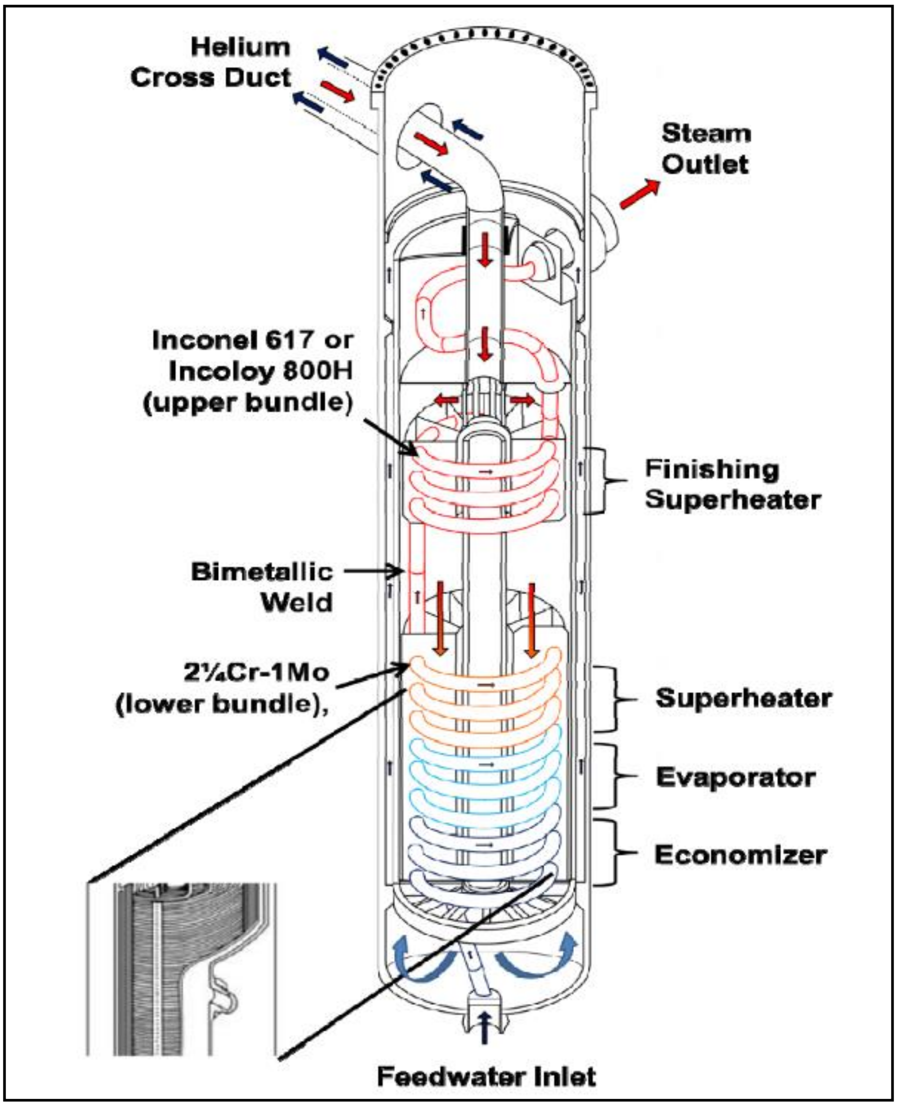


**Figure 2-16: NGNP helical coil steam generator preconceptual design (Hoffer *et al.*, 2011)**

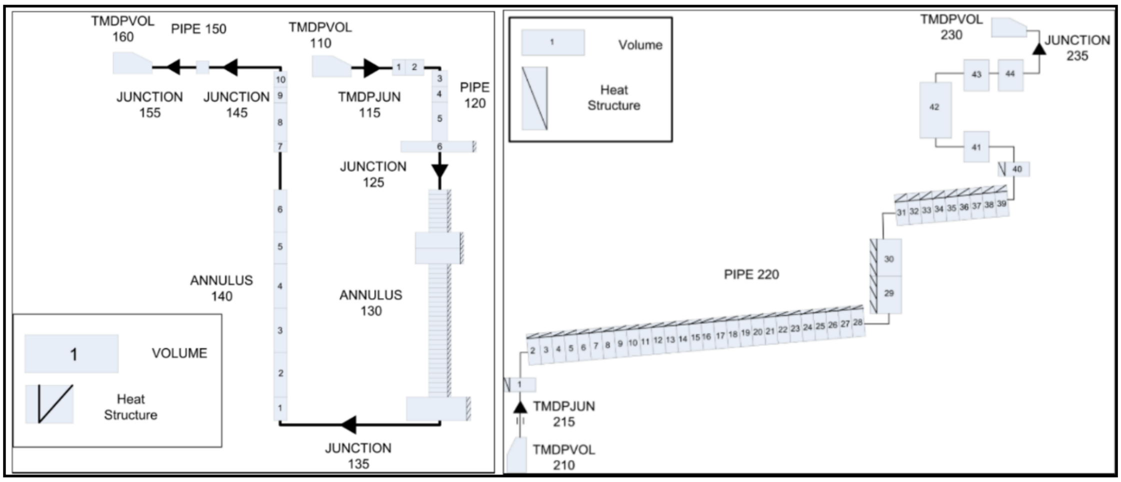


**Figure 2-17: RELAP5-3D steam generator primary and secondary node visualisation (Hoffer *et al.*, 2011)**

Modelling of the helical coil section of the steam generator was done by simplifying the 441-tube bundle to a single pipe with equivalent flow area, heat transfer area, hydraulic diameter, and heated hydraulic diameter. Further simplifications were made by modelling the coil as a straight pipe with length of a single tube and set at a slight incline to achieve the same elevation change as the tube bundle. The nodalisation of the model can be seen in Figure 2-17. The primary and secondary side of the SG was connected with heat structures between annulus 130 on the primary side and pipe 220 on the secondary side which was set at an incline as discussed. The larger area sections of annulus 130 represented sections of the annulus where there are no tube bundles, resulting in a larger flow area and these sections were connected to vertical pipe sections on the secondary side. In this case time dependent volumes were used at the inlet and outlet of both the primary and secondary sides to specify the boundary conditions namely pressure and temperature. Time dependent junctions were used to control the mass flow of the primary and secondary side (Hoffer *et al.*, 2011).

In comparison to straight pipe heat exchangers, helical coil heat exchangers have been shown to have a heat transfer coefficient which is 16 % to 43 % higher (Prabhanjan *et al.*, 2002). To replicate the effects of the increased heat transfer coefficient in helical coil heat exchangers, Hoffer *et al.* (2011) applied a heat transfer multiplier to the model, although the value of this multiplier was not specified. Hoffer *et al.* (2011) also made changes to the helical coil heated length and mass flow rates to achieve the design primary and secondary outlet temperatures.

Skolik *et al.* (2021) followed a similar approach as Hoffer *et al.* (2011) when modelling the NuScale SMR helical coil SGs. The 1380-tube bundle was simplified to a single pipe with the equivalent flow area and hydraulic diameter and was placed at an angle to account for elevation change as seen in Figure 2-11. As with Hoffer *et al.* (2011), Skolik *et al.* (2021) found that the heat removal from the straight pipe model was not adequate. Thus, the heat transfer area of the heat structure was increased by ~30 % to achieve the primary and secondary system outlet temperatures. Furthermore, the feedwater flow rate was adjusted to achieve the design parameters of the reactor.

The MASLWR conceptual SMR design utilises a helical coil SG as was seen in Figure 2-4. A sensitivity analysis of the MASLWR SG was conducted using the TRACE (US NRC, 2008) system code. TRACE was used to model the OSU MASLWR test facility, and the codes' ability to replicate the natural circulation phenomena was evaluated. Furthermore, the fidelity of various methods of modelling the OSU MASLWR SG was evaluated. The SG is located in the annulus formed between the outer surface of the riser and the inner surface of the RPV. The SG consists of 14 tubes with a total heated length of 86 m. The tubes are divided into three parallel coils with the outer and middle coils consisting of five tubes each, and the inner coil consisting of 4 tubes. The three coils share a common inlet header and a common steam drum at the outlet. The SG can be seen in Figure 2-18 (Mascari *et al.*, 2011).

**Figure 2-18: Photo of OSU MASLWR test facility steam generator (Mascari *et al.*, 2011)**

The TRACE model was developed and is illustrated using SNAP (Information Systems Laboratories, 2022) as seen in Figure 2-19. Both primary and secondary circuits were modelled as well as the high-pressure containment (HPC) and the cooling pool vessel. To enhance the codes' ability to replicate natural circulation phenomena, the "slice nodalisation" technique was used. This technique entails modelling volumes located at the same elevation with the same volume length. Three approaches were taken in modelling of the SG secondary side. The first (REF) as shown in Figure 2-19 modelled the SG with three oblique sets of pipes, representing the three parallel SG tube coils. The second approach (SEN1) modelled the SG with three vertical sets of pipes. With both REF and SEN1 models the three sets of pipes were each connected with a heat structure with an equivalent heat transfer area to the SG section of the primary circuit. The third approach (SEN2) modelled the SG with a single vertical pipe with a single heat structure connected to the primary side. In general, the results gathered from the three modelling methods of the SG agreed with each other. When compared to experimental data some differences were observed in terms of the temperature difference between the inlet and outlet of the core, the flow rate through the core and the outlet temperature of the SG on the secondary side. Differences in the data between the experimental and simulation results are most likely due to the heat transfer between the riser and downcomer in the test facility which was not replicated in the simulations. Oscillations in the outlet temperature of the secondary side was observed for the REF and SEN1 simulations. These oscillations were eliminated by modelling the SG as a single vertical pipe allowing the code to better predict the temperature at this point (Mascari *et al.*, 2011).

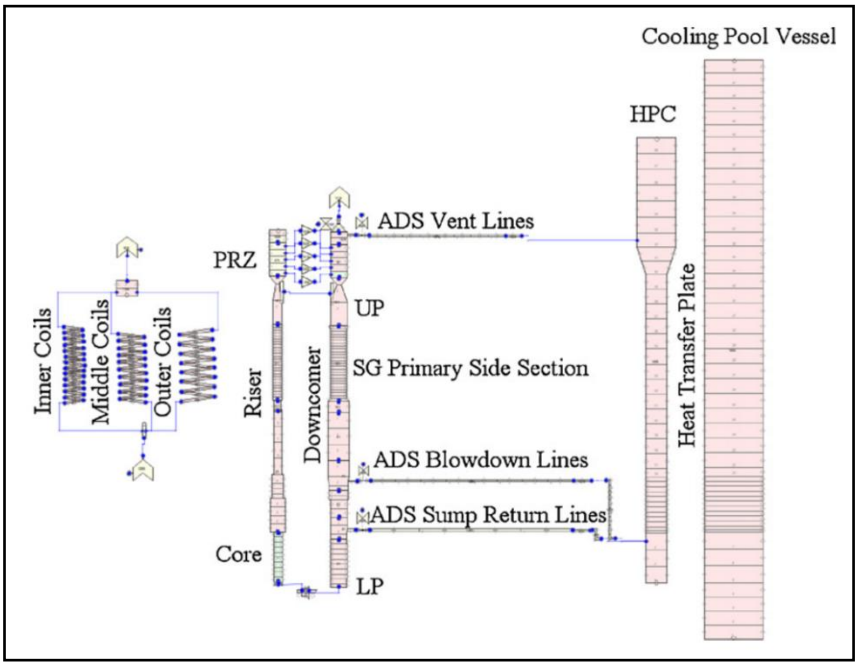


**Figure 2-19: OSU MASLWR TRACE Model (REF) (Mascari *et al.*, 2011)**

## 2.4 Thermal-hydraulic codes

The prediction of the nuclear reactor behaviour by thermal-hydraulic codes plays a crucial role in the field of nuclear safety. In general, these thermal-hydraulic codes can be grouped into two categories. Firstly, system level thermal-hydraulic codes are used to evaluate the thermal-hydraulic interaction between components to predict the system's behaviour during steady state and transient conditions. Results from the system level evaluation may be used to perform more detailed analysis of the core or other components. Sub-channel thermal-hydraulic codes are used for more detailed analysis of the reactor core to estimate the safety margins in the core during steady state and transient conditions (Moorthi *et al.*, 2018). This subsection primarily focusses on system level thermal-hydraulic codes.

RELAP5/MOD3 is an internationally recognised advanced thermal-hydraulic code used to analyse steady state operation and transients in LWRS. The code was initially developed to evaluate the complex thermal-hydraulic interactions during large or small break LOCAs in PWRs. However, expansion of the code's capabilities has allowed for the code to be used in a wide range of applications such as evaluation of operational transients in PWRs and various transients in experimental and production reactors, and to a lesser extent analysis of BWR systems. The code is a nonhomogeneous, nonequilibrium code solving for the six field equations namely the mass, energy, and momentum field equations of two phases giving a two-fluid system simulation. The code is solved by a fast, partially implicit numerical scheme. Boron and non-condensable gasses are also simulated, each having separate equations. A point kinetics model coupled with the field equations allows for feedback between the thermal-hydraulics and neutronics to be simulated. The addition of control systems and other components allow for extensive modelling of NPPs (Idaho National Engineering Laboratory, 1995).

RELAP/SCDAPSIM is a code developed by the SCDAP Development and Training Program (SDTP). The code is a best-estimate system thermal-hydraulic code used to evaluate nuclear reactors during steady state and transient conditions. The code uses publicly available RELAP5 and SCDAP models and correlations with the addition of proprietary programming and numerical methods developed by Innovative Systems Software (ISS) and other members of the SDTP. RELAP5's thermal-hydraulics models are used while SCDAP models are used to describe the behaviour of structures in the core and upper and lower plenum. Simulation of the oxidation and melting of these structures may contribute to the accuracy of models (Skolik *et al.*, 2021).

TRACE (TRAC/RELAP Advanced Computational Engine) is a newer iteration of the advanced, best-estimate reactor system codes. The code was developed by the U.S. NRC to evaluate neutronic-thermal-hydraulic behaviour in LWRs during steady state operation and transients. The code is a combination of the NRC's existing system codes namely TRAC-B, TRAC-P, RELAP5 and ROMANA. TRACE is the same as RELAP5/MOD3 as it is a nonhomogeneous, nonequilibrium code solving for the six field equations to simulate a two fluid system (US NRC, 2008).

SAMPSON is thermal-hydraulic code developed in Japan to evaluate plant behaviour during severe accident transients. The code consists of eleven modules designed analyse specific phenomena associated with the progression of severe accidents. The RELAP portion of RELAP/SCDAPSIM has been integrated into the SAMPSON code as part of the in-vessel thermal-hydraulic analysis module. The other modules of the code are used to analyse fuel rod heat-up, Fission Products (FP) release from fuel, FP transport, molten core relocation, debris cooling, debris spreading, debris-concrete reaction, CNV thermal-hydraulics, steam explosion and hydrogen transfer (Naitoh *et al.*, 2005).

ASYST (Adaptive System Thermal-hydraulics) is a new code in development by ISS, Institute of Applied Energy (IAE), Energy Software Services (ENSO), and selected international members of the SDTP. The system thermal-hydraulic models of ASYST are derived from the SAMPSON thermal-hydraulic analysis module. The SCDAPSIM model used in ASYST is derived from the SCDAPSIM module of RELAP/SCDAPSIM. ASYST aims to combine the design concepts of RELAP/SCDAPSIM, that has balanced performance and accuracy, with the detailed modelling approaches taken from SAMPSON (Allison *et al.*, 2020).

## 2.5 Conclusion

Zr-alloy has been used in PWRs as cladding material for many years. This material has a low neutron absorption cross section resulting in a good neutron economy. The material also has good thermal-hydraulic properties with a high thermal conductivity and good oxidation resistance under normal operating conditions. However, the oxidation resistance is low when the material is exposed to high temperature steam, resulting in the production of hydrogen. The melting point of the material is also low when compared to the accompanying $UO_2$ fuel. Candidate ATF cladding materials aim to improve the safety of PWRs by improving the oxidation resistance, thermal-hydraulic performance, and melting point of nuclear fuel cladding.

Chromium coating of Zr-alloy is a promising candidate for ATF cladding. It improves the oxidation resistance of Zr-alloy without having a negative impact on the neutron absorption cross section. Some surface characteristics of the chromium coating could also be beneficial in terms of thermal-hydraulic performance. FeCrAl cladding is a promising replacement for Zr-alloy cladding as it has a similar thermal conductivity, slightly better heat capacity and a higher failure temperature due to improved oxidation resistance. However, the material has a large neutron absorption cross section. On the other hand, SiC is a candidate for cladding material with a smaller neutron absorption cross section compared to Zr-alloy. The material also has a much higher melting point closer to that of $UO_2$ and a large heat capacity. However, the material has a lower thermal conductivity which further degrades with irradiation.

Apart from ATF, various passive safety systems and new reactor concepts are in development with the goal of improving safety in LWRs. Small modular reactors are one of the new reactor concepts designed around passive safety. Most SMRs of the light water type rely only on natural circulation for coolant flow through the core in both operating conditions and accident scenarios. These natural circulation SMRs tend to have excellent safety with the SMRs being able to cope with a wide range of accident transients. However, there does exist some common flow phenomena and sequences of events which are problematic for this type of SMR. Many light water SMRs exhibit some form of flow oscillation, either during startup and shutdown transients or accident transients. Furthermore, accident scenarios involving the inadvertent opening of a vent valve with subsequent failure of a recirculation valve, or vice versa, also tend to pose problems in light water SMRs, as this results in a reduction of the coolant level and the core becoming uncovered.

The NuScale SMR is chosen for this study because it is the SMR that is the furthest along in its development and it has received standard design certification by the U.S. NRC. Specifications of the NuScale SMR is also readily available in the NuScale FSAR made available by the U.S. NRC., with data being further supplemented by various articles in academic literature. Steady state operation of the NuScale SMR will be evaluated along with a worst-case scenario accident transient which is the inadvertent opening of a RVV with subsequent failure of the ECCS and DHRS. This transient is chosen as it is one of few transients which lead to failure of the cladding material and results in meltdown of the core.

In the current study, ASYST 3.4 (Innovative Systems Software, 2023) thermal-hydraulic code will be used. This code is considered the best-estimate system thermal-hydraulic code for evaluating nuclear reactors under steady state and transient conditions. It is based on well-established thermal-hydraulic codes such as SAMPSON and RELAP/SCDAPSIM. RELAP/SCDAPSIM has been successfully used to model a NuScale SMR (Fakhraei *et al.*, 2020; Skolik *et al.*, 2021). The license for ASYST 3.4 is provided by the North-West University.

Modelling of the NuScale SMR will be done, with a full primary loop and CNV, and a partial secondary loop, UHS pool and reactor building. The core will be simplified to a hot channel with one fuel assembly, an average channel with 36 fuel assemblies, and one bypass channel. The power distribution of the core is predetermined and given by the NuScale FSAR. The power produced by the core for the selected accident transient is also given by Skolik *et al.* (2021) and will be used as input. Thus, no neutronic calculations will be done. Only a partial secondary loop will be modelled as the purpose of the secondary loop in this model will be to remove heat from the primary loop to achieve an energy balance and drive the natural circulation of the primary loop during steady state operation. The SG tube bundles will be simplified to a single straight pipe with equivalent flow area, hydraulic diameter, and heat transfer area. The model will be verified with data found in the NuScale FSAR and the study by Skolik *et al.* (2021) for steady state operation and the selected accident transient.

The verified model will be used to evaluate the use of ATF cladding materials in the NuScale SMR. FeCrAl and SiC are selected as the candidate ATF cladding materials for this study. The steady state operation of the NuScale SMR with ATF cladding will be evaluated. This is important as the natural circulation is dependent on the heat transfer from the $UO_2$ fuel to the coolant through the cladding. Furthermore, the thermal-hydraulic performance of the cladding will be evaluated during a worst-case scenario accident transient, with the goal of improving the PFCT, PCT and increasing the coping time.

Development of the NuScale SMR model will commence in Chapter 3. This will include data collection of the NuScale SMR, nodalisation of the model, data collection of material properties and verification of the model for steady state operation and the selected accident transient.

# CHAPTER 3: REFERENCE MODEL

The thermal-hydraulic evaluation of ATF in the NuScale SMR is to be performed in this study. This requires the development of a reference model. The model will be based on specifications gathered from the NuScale FSAR (NuScale Power LLC., 2020b, 2020c, 2020d) as well as open literature. The model will be verified for steady state operation as well as a worst-case scenario accident transient. Once the model is verified, the evaluation of ATF in the NuScale SMR model can commence.

## 3.1 Overview

A NuScale power plant (NPP) will contain 12 NPMs, each producing 50 MW of electrical power for a total of 600 MW electrical power per NPP. All 12 NPMs are situated inside one large reactor pool which acts as UHS during accident scenarios. At full load, each NPM produces 160 MW thermal power. The naturally circulating primary coolant is only driven by buoyancy forces, eliminating the need for coolant pumps and piping. Each NPM contains two independent helical coil SGs which form part of the secondary loop. Secondary flow occurs inside the tubing while primary flow is on the outside of the tubing (Fakhraei *et al.*, 2021). A schematic view of the reactor building can be seen in Figure 3-1. The general specification of a NPM is shown in Table 3-1 as taken from the NuScale FSAR.

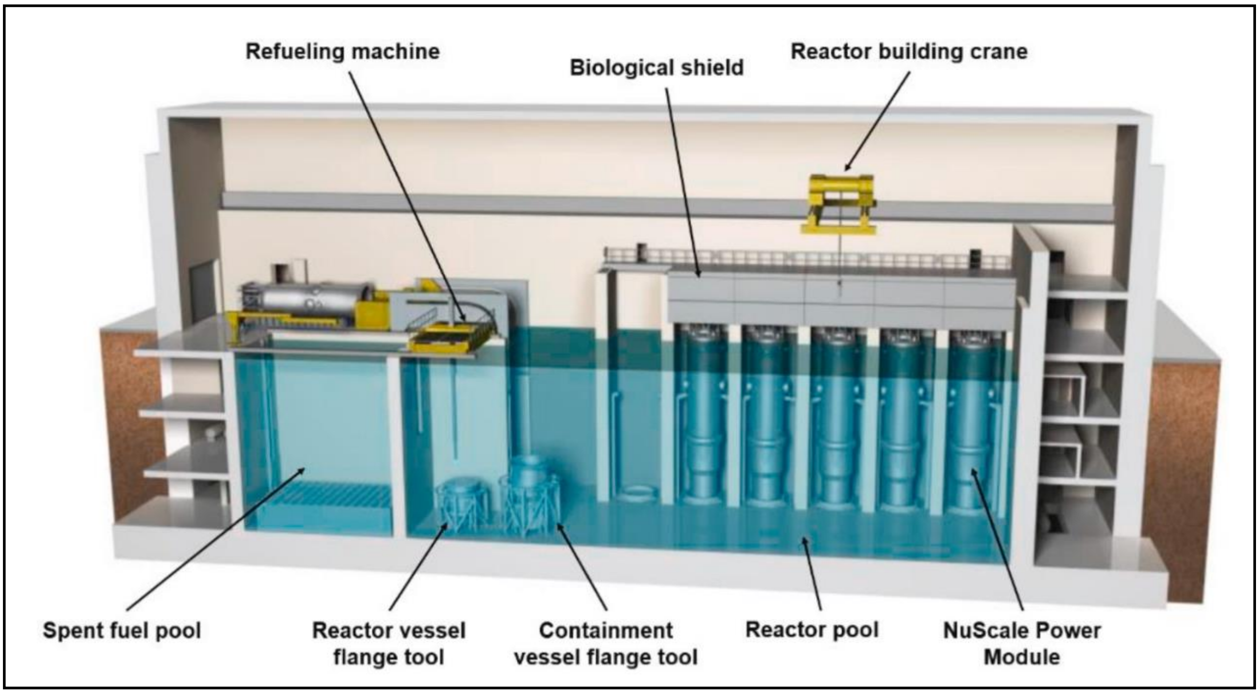


**Figure 3-1: NuScale reactor building (Fakhraei *et al.*, 2021)**

**Table 3-1: General specifications of NPM (NuScale Power LLC., 2020a)**

| NuScale specifications | | |
|---|---|---|
| **Core** | | |
| Electrical output | 50 | MW |
| Thermal output | 160 | MW |
| # fuel assemblies | 37 | - |
| Fuel assembly lattice | 17x17 | - |
| Effective fuel length | 2.00 | m |
| Fuel rods per assembly | 264 | - |
| Average linear heat rate | 8.2 | kW/m |
| # control rod assemblies | 16 | - |
| **Reactor Control system** | | |
| Operating Pressure | 12.75 | MPa |
| Hot leg temperature | 583.15 | K |
| **Reactor Vessel** | | |
| Inner diameter | 2.7 | m |
| Thermal shielding and reflector design | Stacked SS reflector blocks | - |
| **Steam generators** | | |
| Number | 2 | - |
| Type | Helical coil | - |
| Heat transfer area | 1672.25 | $m^2$ |
| Number of tubes | 1380 | - |
| **Pressurizer** | | |
| Internal Volume | 16.084 | $m^3$ |
| **Containment** | | |
| Type | Steel pressure vessel | - |
| Inner diameter | 4.318 | m |
| Height (outer) | 23.076 | m |

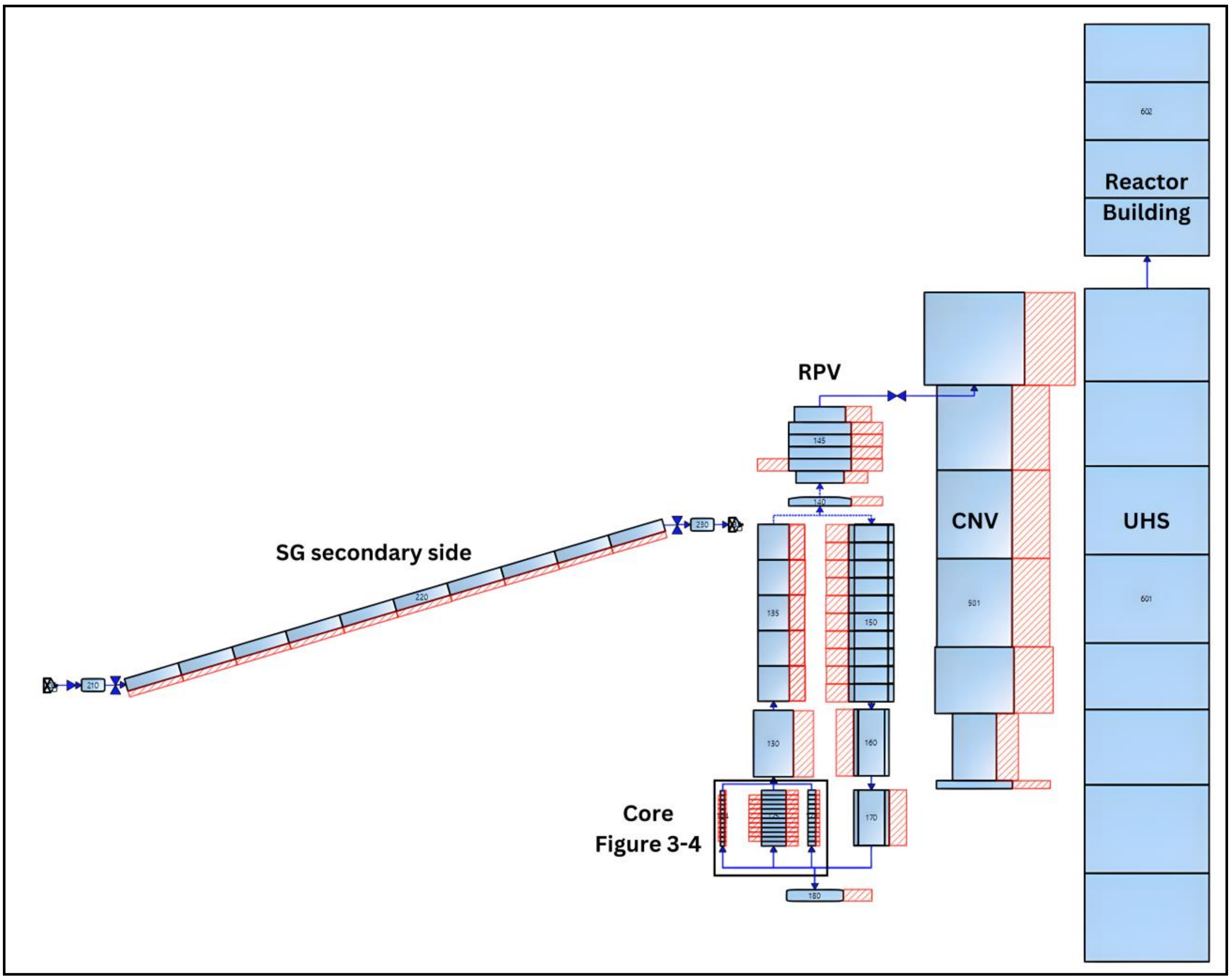


**Figure 3-2: NuScale SMR model in RHYS**

## 3.2 Thermal-hydraulic code

For this study, a single NPM is modelled using ASYST 3.4.0 (Build 03/2019) (Innovative Systems Software, 2023) system analysis code. Input files for ASYST 3.4 and RELAP5/MOD3 (Idaho National Engineering Laboratory, 1995) are interchangeable and RELAP5/MOD3 code manuals are used as guideline for the model development. RELAP5 is a transient, two phase, non-equilibrium and non-homogeneous code that solves for mass continuity, momentum, and energy field equations for two phases. The code is used for evaluation of nuclear reactor designs and to predict the behaviour of nuclear reactors during accident scenarios (Fakhraei *et al.*, 2021). The RHYS graphical user interface (GUI) is used to simplify the modelling process and to assist with interpretation and processing of results. The layout of the model developed for the NuScale SMR using RHYS can be seen in Figure 3-2. The different sub-sections of the model will be discussed in detail in the following sections.

A general modelling approach is followed as described by the RELAP5/MOD3 code manual. Firstly, a model boundary is established, which for this study surrounds one NPM. The behaviour of the primary system is to be evaluated so the full primary system must be modelled along with the CNV and a partial UHS pool. Only the portion of the secondary system that interacts with the primary system is required for the model.

With the model boundary established, the model can be nodalised, which is the process of dividing the model into control volumes forming discrete components. RELAP5 is designed to evaluate the interaction of system components rather than detailed analysis of fluid flow within components. Thus, system components are modelled as control volumes, which are essentially pipes, and connected with junctions at the inlets and outlets. The average fluid properties are calculated at the centre of each control volume with fluid vector properties being calculated at junctions (Idaho National Engineering Laboratory, 1995).

It is recommended by the RELAP5/MOD3 code manual that the system be modelled with the simplest set of nodes (control volumes) by dividing the model into roughly equally sized nodes. However, this might not be possible as the geometry of the system most likely requires nodes with various lengths, flow areas and orientations. The node size is governed by factors such as numerical stability, run time and spatial convergence. Numerical stability requires that the length to diameter ratio of nodes have a lower bound of one. Nodes should in general be made as large as possible as this directly impacts the run time. The material Courant limit prevents the time step from exceeding the node length divided by the maximum fluid velocity. Thus, smaller nodes result in smaller maximum time steps which increases the run time. It is recognized that for certain sections of the model the user might be interested in fluid behaviour which cannot be captured with one control volume. For these sections, a finer nodalisation may be used (Idaho National Engineering Laboratory, 1995).

ASYST 3.4 uses a transient solution algorithm which uses numerical methods to calculate and predict the behaviour of nuclear reactors over time. The code gives the user control over the time steps, with the user being able to specify a maximum and minimum time step for each interval, and multiple intervals may be used throughout the simulation. For each time step, the code will attempt to run the model at the maximum time step. A smaller maximum time step is recommended at the start of the simulation to help with initialisation of the problem. The code is allowed to reduce the time step up to the minimum time step based on several factors. The material Courant limit must be adhered to. The code also monitors mass, quality, fluid property and extrapolation errors, and reduces the time step if these errors exceed predetermined internal limits (Idaho National Engineering Laboratory, 1995).

## 3.3 Model description

### 3.3.1 Core

The NuScale SMR core is made up of a total of 37 fuel assemblies. As can be seen in Table 3-2 each fuel assembly is ~ 2.4 m in length and has a pitch of 215 mm. The assemblies are placed in a grid within the core of the reactor and are surrounded by the core barrel. Reflector blocks are located in between the fuel assemblies and core barrel. Coolant is allowed to flow through the fuel assemblies to cool fuel elements. Flow through the guide and instrumentation tubes and flow through the coolant channels of the reflector blocks makes up the bypass flow.

**Table 3-2: NuScale core design parameters (NuScale Power LLC., 2020b)**

| | | |
|---|---|---|
| **Core** | | |
| Diameter of active core | 1.506 | m |
| # Fuel assemblies | 37 | - |
| Height to diameter ratio of core | 1.33 | - |
| Total cross-sectional area of core | 1.711 | $m^2$ |
| Core barrel ID | 1.8796 | m |
| Core barrel OD | 1.9812 | m |
| **Reflector** | | |
| Height | 2.33 | m |
| Width | 6.35 – 30.99 | cm |
| **Fuel assembly** | | |
| Fuel design | NuFuel HTP2 | - |
| Length | 2.4 | m |
| Nominal $UO_2$ per assembly | 249.2 | kg |
| Rods per fuel assembly | 264 | - |
| Fuel assembly pitch | 215.0 | mm |
| Fuel rod pitch | 12.6 | mm |
| # of grids per assembly | 5 | - |
| Span of grid | 510.54 | mm |
| # of guide tubes per assembly | 24 | - |
| # of instrument tubes per assembly | 1 | - |
| Guide tube dashpot region ID | 10.08 | mm |
| Guide tube dashpot region OD | 12.24 | mm |
| Guide tube above dashpot ID | 11.43 | mm |
| **Fuel rod** | | |
| Peak rod exposure core design criteria for UO2 rods | 62 | GWd/MTU |
| $Gd_2O_3$ concentration | Up to 8 % | - |
| Cladding OD | 9.4996 | mm |
| Cladding ID | 8.2804 | mm |
| Cladding thickness | 0.6096 | mm |
| Pellet-Cladding diametral gap | 0.1651 | mm |
| Cladding material | M5 | - |
| Fuel column length | 2.00 | m |
| Overall fuel rod length | 2.159 | m |
| Fuel pellet material | UO2 | - |
| Fuel pellet diameter | 8.1153 | mm |
| Fuel pellet density (theoretical) | 96 | % |
| Fuel pellet length | 10.16 | mm |
| Fissile enrichment | < 4.95 | % |

Each of the 37 fuel assemblies is made up of a 17 by 17 lattice, consisting of 264 fuel pins, 24 control rod guide tubes and one instrumentation tube as shown in Figure 3-3. For this study, the core will be divided into two active fuel channels and a third channel which acts as core bypass flow. The two active fuel channels are the hot channel consisting of the hot central fuel assembly, and the average channel consisting of the remaining 36 fuel assemblies. The calculated core channel dimensions for this model can be seen in Table 3-3. The flow area of the two active channels is calculated as the total cross-sectional area of the fuel assemblies (calculated using the fuel assembly pitch) and subtracting the cross-sectional area of the fuel pins and guide tubes. The flow through the bypass channel is the combined flow through the guide tubes and flow through the reflector cooling channels. The reflector cooling channels contribute to 4.5 % of the bypass flow while the bypass flow through the guide and instrumentation tubes is 4.0 % for a maximum bypass flow of 8.5 % (NuScale Power LLC., 2019). The hydraulic diameter of the core channels is calculated as four times the flow area of the channel divided by the wetted perimeter which includes the circumference of each fuel pin and guide tube as well as the square perimeter of the channel. The hydraulic diameter of the average channel is the same as that of the hot channel due to the flow area and wetted perimeter increasing by the same factor when several fuel assemblies are considered. The geometry of the bypass channel is unknown and thus the hydraulic diameter of the bypass channel is set to 0.22 m as in the study done by Skolik *et al.* (2021).

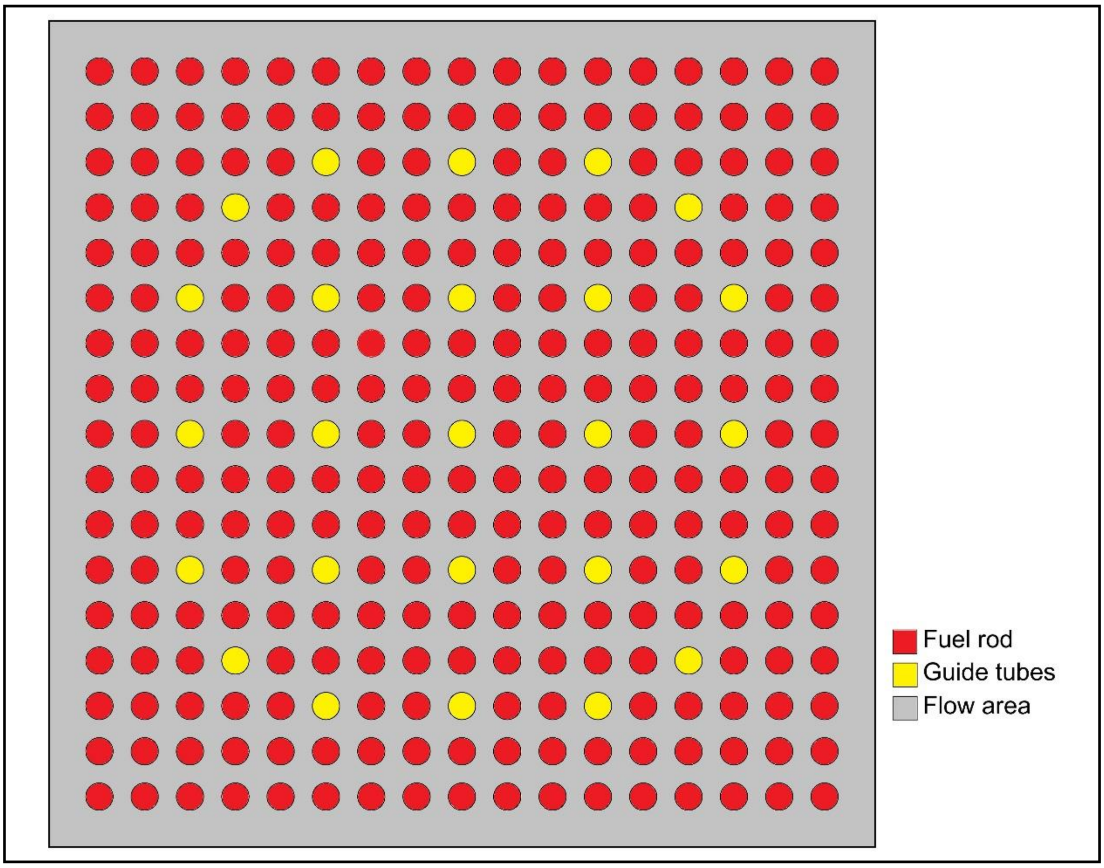


**Figure 3-3: Fuel assembly layout**

**Table 3-3: NuScale SMR model core channels**

| Fuel channel dimensions | | | |
|---|---|---|---|
| | **Hot channel 124** | **Average channel 125** | **Bypass channel 126** |
| # fuel assemblies | 1 | 36 | - |
| # fuel rods | 264 | 9504 | - |
| Flow area (m$^2$) | 0.0246 | 0.8851 | 0.0845 |
| Hydraulic diameter (m$^2$) | 0.011 | 0.011 | 0.22 |
| Length (m) | 2.0 | 2.0 | 2.0 |
| Increments | 10 | 10 | 10 |
| Increment length (m) | 0.2 | 0.2 | 0.2 |
| Estimated mass flow (kg/s) | 14.5 | 522.7 | 49.9 |

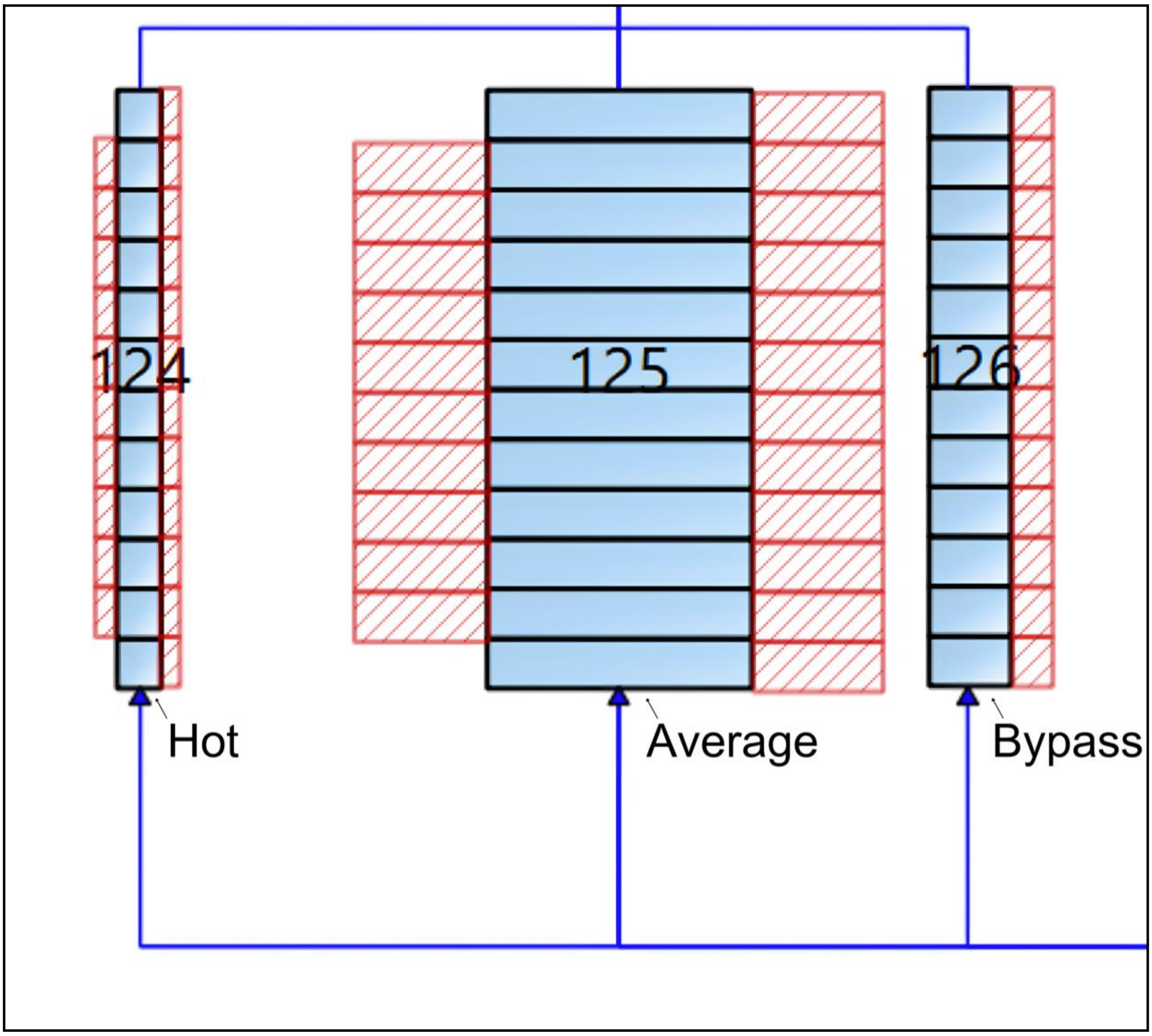


**Figure 3-4: NuScale SMR model fuel channels**

Each fuel channel is divided into 12 axial sections with a length of 0.2 m each. The central 10 axial nodes are connected to the active fuel, while one axial node on each end represent the tips of the fuel pins. Fakhraei *et al.* (2020) and Skolik *et al.* (2021) both employed similar approaches, each utilizing 10 axial nodes in the fuel element. The modelled fuel channels can be seen in Figure 3-4 as taken from RHYS.

The fuel pins are made up of cylindrical $UO_2$ fuel pellets stacked within a sealed cladding tube traditionally made of Zr-alloy. A small helium gap exists between the fuel pellets and cladding which is filled with pressurised helium. This gap allows for swelling of the fuel pellets, however for this study the dimensions of the fuel pellet and cladding will be assumed to remain constant as seen in Table 3-2.

Fuel elements are modelled in RELAP5 using the heat structure component which provides one dimensional heat transfer between the left and right boundaries of the heat structure. The heat structures representing the fuel elements in the current model can be seen on the left side of Channels 124 and 125 in Figure 3-4. The fuel element is modelled starting at the fuel centreline and moving outward. The fuel element is divided into ten radial nodal points which creates nine intervals. The heat structure radial intervals are equally spaced within each material (Idaho National Engineering Laboratory, 1995). Thus, four intervals of equal length make up the $UO_2$ fuel, two intervals of equal length make up the helium, and the remaining three intervals of the cladding are of equal length. Skolik *et al.* (2021) used a similar approach with the exception that only one interval was used for the helium gap. The heat structure is also divided into ten axial nodes with a total length of 2.0 m, matching the ten central axial nodes of the fuel channel. The left boundary of the heat structure represents the fuel centreline, and a symmetry or insulated boundary condition will be used. The right boundary of the heat structure representing the outer surface of the cladding, will be connected to the coolant channel and therefore the convective heat transfer boundary condition of ASYST 3.4 will be used. Seeing that the hot and average channels of the model have differing numbers of fuel pins, a surface area (SA) factor is used to achieve the correct heat transfer area on the right boundary of the heat structure. For a cylindrical heat structure, the SA factor is defined as the height of the cylindrical section which is 0.2 m in this case. For multiple fuel pins this should be multiplied by the number of fuel pins for each channel which is 264 and 9504 for the hot and average channel, respectively. The SA factor and other heat structure dimensions can be seen in Table 3-4.

**Table 3-4: Fuel pin heat structure dimensions**

| | Hot channel | Average channel | |
|---|---|---|---|
| $UO_2$ outer radius | 0.00406 | 0.00406 | m |
| Gap outer radius | 0.00414 | 0.00414 | m |
| Cladding outer radius | 0.00475 | 0.00475 | m |
| Length | 2.0 | 2.0 | m |
| # axial increments | 10 | 10 | - |
| Length per increment | 0.2 | 0.2 | m |
| # fuel pins | 264 | 9504 | - |
| SA factor | 52.8 | 1900.8 | - |
| Power factor | 1.091 | 0.997 | - |
| Power fraction | 0.02949 | 0.97043 | - |

The power produced by the core is spread equally across the section of the heat structure representing the $UO_2$ fuel. The power produced by the hot and average channel is dependent on the number of fuel assemblies per channel and the power factors of the fuel assemblies in each channel. The radial power distribution of the NuScale SMR core at the beginning of cycle (BOC) is shown in Figure 3-5. The power factor of the hot channel is set to be 1.091 to coincide with the hot channel in the study done by Skolik *et al.* (2021). This value was chosen to be able to compare the results of this study to the worst-case scenario accident transient of Skolik *et al.* (2021), even though there are assemblies with higher power factors in the FSAR as seen in Figure 3-5. The average channel has a power factor equal to the average of the power factors of the remaining 36 fuel assemblies. The hot and average channels will each provide a fraction of the total power of the reactor. This fraction is calculated for the hot channel as its power factor multiplied by 1/37, and for the average channel as its power factor multiplied by 36/37. The power factors and power fractions of the hot and average channels are included in Table 3-4.

| | | | | | | |
|---|---|---|---|---|---|---|
| BOC | | 0.895 | 0.911 | 0.888 | | |
| | 1.033 | 1.137 | 0.957 | 1.135 | 1.033 | |
| 0.888 | 1.135 | 1.054 | 0.967 | 1.054 | 1.136 | 0.895 |
| 0.911 | 0.957 | 0.967 | 1.091 | 0.967 | 0.957 | 0.911 |
| 0.895 | 1.136 | 1.054 | 0.967 | 1.054 | 1.135 | 0.888 |
| | 1.033 | 1.135 | 0.957 | 1.137 | 1.033 | |
| | | 0.888 | 0.911 | 0.895 | | |

**Figure 3-5: NuScale SMR assembly radial power distribution at BOC (NuScale Power LLC., 2020b)**

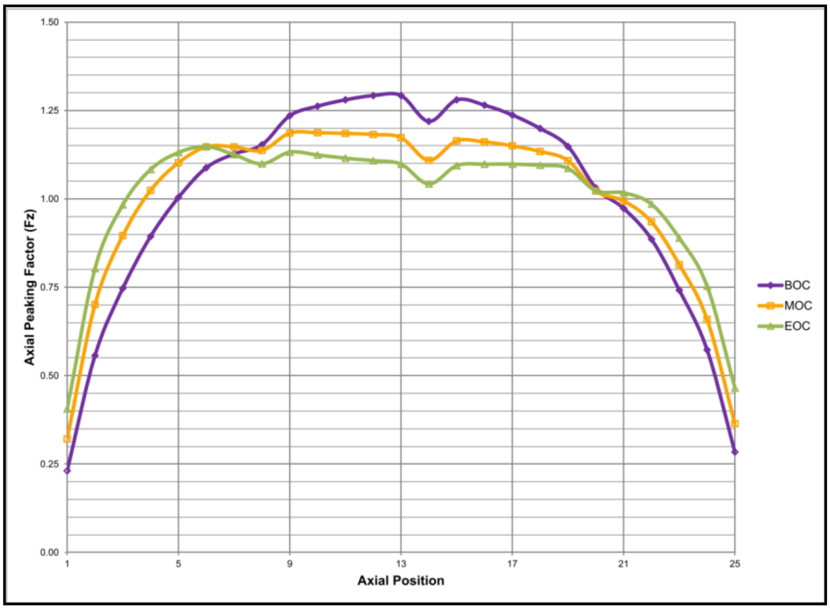


**Figure 3-6: NuScale SMR core axial power peaking factors (NuScale Power LLC., 2020b)**

The power produced by the core is further spread across the core in the axial direction. The axial power peaking factors can be seen in Figure 3-6, and the axial power peaking factors at BOC will be used. A power factor is used for each of the ten axial nodes in the heat structure to replicate the axial power distribution shown in Figure 3-6. This power factor is then divided by ten to convert it to an axial power fraction. The final power fraction for each of the ten nodes of each fuel channel is determined by multiplying the axial power fraction with the power fraction of the hot and average channels shown in Table 3-4. The final power fraction of each node of the two active fuel channels can be seen in Table 3-5, with the nodes starting from the bottom of the heat structure and moving upwards.

**Table 3-5: Core channel axial power distribution**

| Axial node | Hot channel | Average channel |
|---|---|---|
| 1 | 0.0012805 | 0.0421438 |
| 2 | 0.0027109 | 0.0892189 |
| 3 | 0.0033032 | 0.1087103 |
| 4 | 0.0036504 | 0.1201387 |
| 5 | 0.0038240 | 0.1258529 |
| 6 | 0.0037527 | 0.1235041 |
| 7 | 0.0036882 | 0.1213832 |
| 8 | 0.0032973 | 0.1085175 |
| 9 | 0.0026523 | 0.0872907 |
| 10 | 0.0013306 | 0.0437914 |

Besides the heat structures representing the fuel elements in the core, there also exists heat structures connecting the hot and average channels to the bypass channel. These heat structures are shown on the right side of Channels 124 and 125 in Figure 3-4. These heat structures represent the guide tube and instrumentation tube walls and allows for heat transfer from the two active channels to the bypass channel. The thickness of the heat structure is calculated from the inner and outer diameter of the guide tubes as shown in Table 3-2. For this heat structure a convective heat transfer boundary condition will be used for both left and right boundaries with the left boundary connected to the active fuel channel and the right boundary connected to the bypass channel. As with the fuel element heat structures a SA factor is used to achieve the true heat transfer area, with the SA factor being the height of the cylinder multiplied by the number of guide tubes per channel. A final heat structure exists in the core section representing the core barrel and allowing for heat transfer to the annular section of the downcomer. Dimensions are calculated from the core barrel ID and OD found in Table 3-2. The convective heat transfer boundary condition is used for the left and right boundaries, with the left boundary connecting to the bypass channel and the right boundary connecting to the annular section of the downcomer.

### 3.3.2 Primary loop

The primary loop of the NuScale SMR is comprised of various components, all located in the RPV and includes the core with all its associated components, the riser which is the pipe section above the core, upper and lower plenum, the downcomer which is the annular space formed between the riser outer wall and the inner wall of the RPV, and the pressurizer which is the volume located above the RPV upper plenum. The primary loop of the model can be seen in Figure 3-7 as taken from RHYS. Table 3-6 shows the main design parameters of the RPV.

Table 3-7 shows a list of all components forming the primary loop with the corresponding component numbers as well as the number of volumes in each component, the length of each volume, and the volume flow area. The volume lengths are taken from the model by Skolik *et al.*, as this gives a more detailed description of the length of each section (Skolik *et al.*, 2021). The flow area of each volume is taken from the NuScale FSAR, either directly or calculated from given dimensions (NuScale Power LLC., 2020b).

**Table 3-6: NuScale RPV design parameters (NuScale Power LLC., 2020b)**

| **RPV Design parameters** | | |
|---|---|---|
| Design pressure | 14.5 | MPa |
| Design temperature | 616.5 | K |
| ID of lower RPV section (without clad) | 2.5 | m |
| OD of lower RPV section (without clad) | 2.7 | m |
| ID of upper RPV section (without clad) | 2.7 | m |
| OD of upper RPV section (without clad) | 2.9 | m |
| ID of pressurizer (without clad) | 2.7 | m |
| OD of pressurizer (without clad) | 2.9 | m |
| ID of upper head (without clad) | 2.7 | m |
| OD of upper head (without clad) | 2.9 | m |
| Inner clad thickness | 6.4 | mm |
| Outer clad thickness | 3.2 | mm |

**Table 3-7: NuScale SMR model primary loop components**

| **Components** | **Number of volumes** | **Volume length (m)** | **Flow area ($m^2$)** |
|---|---|---|---|
| Pressurizer 145 | 1 | 0.67 | 3.828 |
| | 4 | 0.525 | 5.704 |
| | 1 | 0.53 | 3.354 |
| RPV upper plenum 140 | 1 | 0.382 | 5.704 |
| Upper riser 135 | 5 | 1.528 | 1.43 |
| Upper downcomer 150 | 10 | 0.764 | 2.9798 |
| Middle riser 130 | 1 | 2.87 | 2.313 |
| Middle downcomer 160 | 1 | 2.87 | 1.826 |
| Lower downcomer 170 | 1 | 2.4 | 1.826 |
| RPV lower plenum 180 | 1 | 0.5 | 4.719 |

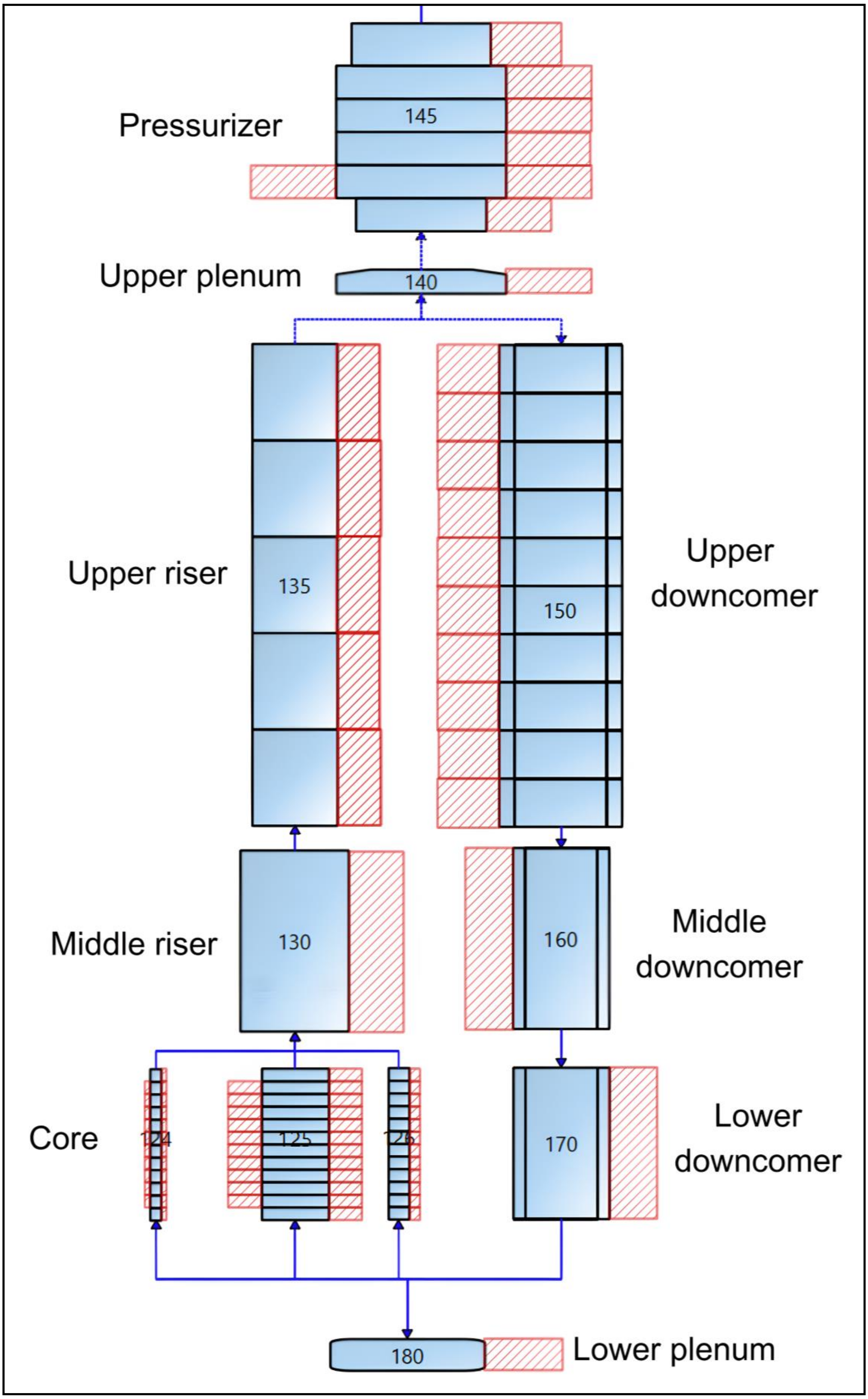


**Figure 3-7: NuScale SMR model primary loop**

The pressurizer located at the top of the RPV consists of six volumes. The topmost volume represents the RPV top head which has a dome shape and thus the volume has a longer length and reduced flow area compared to the rest of the pressurizer. The middle four sections of the pressurizer each have a length of 0.525 m for a total length of 2.1 m. The flow area is calculated from the RPV inner diameter. The bottom most section of the pressurizer has a reduced flow area compared to the rest of the pressurizer due to the secondary side steam headers being in this location. The pressurizer of the NuScale SMR includes two systems for controlling the pressure in the RPV, namely heating element bundles with a total power of 800 kW to increase pressure, and spray nozzles for decreasing pressure. The heating element bundle is represented by a heat structure connected to the second volume from the bottom of the pressurizer. Power to the heating element will be switched on if the pressure in the RPV is below the setpoint of 12.75 MPa, and switched off once the pressure is above the setpoint. The spray nozzles are not typically modelled for this reactor using ASYST 3.4 or similar codes (Fakhraei *et al.*, 2021; Skolik *et al.*, 2021). The short length of the volumes in the pressurizer allows for better control of the initial coolant level. The bottom three volumes are set to be filled with water at the start of the simulation, while the top three volumes are set to have a static quality of 1.0, meaning the mass fraction of air will be 100 %.

The RPV upper plenum is modelled using a branch component. The branch component is a single volume with multiple junction components. Junctions are used to connect volumes to each other as illustrated by the blue arrows between the volumes in Figure 3-7. When using a junction to connect volumes, the outlet face of one volume will be connected to the inlet face of another volume with no space in between them. Thus, the junction component has no volume of itself. The upper plenum connects the riser and downcomer such that the coolant flow will be turned from the upwards direction in the riser to a downward direction in the downcomer. The top of the upper plenum is connected to the pressurizer which controls the pressure in the RPV.

The upper downcomer is represented by an annulus component with a total of 10 volumes. The annulus component in ASYST 3.4 is the same as a pipe component with the exception that an annular flow regime map is used instead of the pipe flow regime map. The upper downcomer also makes up the primary side of the steam generator. The steam generator is made up of two helical coil tube bundles with 1380 tubes in total with an average length of 24.2 m. The steam generator is discussed in more detail in Section 3.3.3. The upper downcomer flow area is determined by taking the RPV cross-sectional area, calculated from the RPV ID, and subtracting the riser cross-sectional area, and further subtracting the cross-sectional area of the steam generator tubes. The assumption is made that all 1380 tubes of the steam generator intersect the cross-section of the upper downcomer at the specified angle. The hydraulic diameter of this section is 0.066 m, which is calculated by multiplying the flow area by four and dividing this number by the wetted perimeter, which includes the RPV inner wall, riser outer wall, and the outer walls of all 1380 steam generator tubes.

The upper riser is a simple pipe section with five volumes and has the same overall length as the upper downcomer. This component is reduced to five volumes to better adhere to both the L/D>1 rule and the Courant limit, and to reduce the number of volumes in the model making the simulation less processing and data intensive. It is not necessary for this component to have more volumes and the number of volumes can be even further decreased to three as seen in the model developed by Fakhraei *et al.* (2021). The upper downcomer on the other hand forms part of the primary side of the steam generator, and thus more volumes are required to achieve a more accurate temperature gradient throughout the steam generator. Other models tend to have more volumes for the upper downcomer for example 20 volumes in the model by Skolik *et al.* (2021), and 30 volumes in the model by Fakhraei *et al.* (2021). For this model, the number of volumes was reduced to ten volumes to avoid thermodynamic property errors in the upper downcomer, which typically occurred during periods of flow oscillations in accident transients. The reduction in the number of volumes has minimal impact on the thermal-hydraulic performance of the primary loop while the ten volumes still provide an adequate temperature gradient in the steam generator. The number of volumes in the riser was chosen as five to simplify the heat structures connecting the upper riser and upper downcomer, as two volumes of the downcomer will be connected to one volume of the riser.

The middle riser is the short section of pipe directly above the core. The section of pipe extends up from the core barrel and has a small cone section at the top for transition to the upper riser. Various studies in literature model this component by dividing it into sections, with one volume for the cone section having a reduced flow area creating a gradual change in flow area between the middle riser and upper riser (Fakhraei *et al.*, 2020; Skolik *et al.*, 2021). For this model however, the entire middle riser section was lumped together into one large volume with an equivalent average flow area which is directly taken from the NuScale FSAR. This was done to eliminate thermodynamic property errors once again in this section during accident transients with flow oscillations. The transition to the upper riser is purely done with the junction connecting the two volumes. The smooth area change model is used for this junction and the junctions connecting the upper and middle downcomers, and the middle and lower downcomers.

The middle and lower downcomers are both annulus components representing the annular space between the middle riser/core barrel and the lower section of the RPV. The middle downcomer has the same length as the middle riser, while the lower downcomer has the same length as the core section. The lower plenum is a single volume at the bottom of the RPV and turns the direction of flow from the downward direction in the downcomer to the upward direction into the core. Junctions with the full abrupt area change model are used between the lower downcomer and lower plenum, between the lower plenum and core channels, and between the core channels and middle riser.

### 3.3.3 Steam generator secondary side

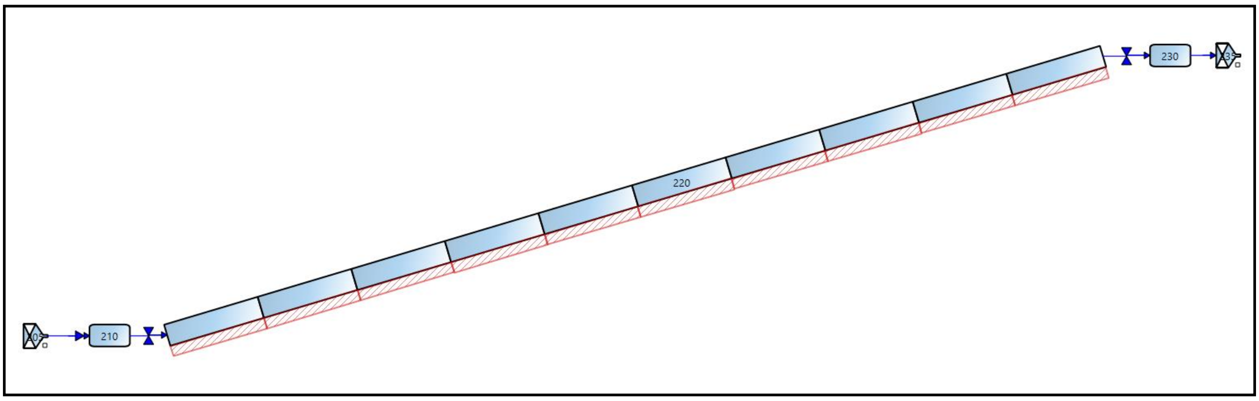


**Figure 3-8: NuScale SMR model steam generator**

The NuScale SMR SG is made up of two helical coil tube bundles with a total of 1380 tubes and average tube length of 24.2 m. To model these tube bundles several simplifications have to be made as was seen in prior studies (Hoffer *et al.*, 2011; Skolik *et al.*, 2021). Firstly the 1380 tubes are lumped together into one pipe with a length of 24.2 m and an equivalent flow area and hydraulic diameter. Then the pipe with a helical coil geometry is unwound to a simple straight pipe and is divided into ten axial nodes. To account for the vertical distance the helical coil tube bundle rises, the single straight pipe is placed at an angle. In this case an angle of 18.4 degrees is used, meaning the 24.2 m pipe will have a vertical height of 7.64 m, matching the length of the upper downcomer which forms the primary side of the steam generator. A heat structure connects the SG pipe to the upper downcomer, with dimensions calculated from the design parameters summarised in Table 3-8. The SG secondary side model of the current study is shown in Figure 3-8.

The SA factor for this heat structure should be calculated in a similar manner to the SA factor of the fuel pins in the core channels, where the SA factor is the height of the cylinder (2.42 m per axial node) multiplied by the number of SG tubes (1380). This gives a SA factor of 3339.6. However, using this SA factor results in a lower heat transfer rate than expected with lower secondary side outlet temperatures, higher primary side outlet temperatures and an energy imbalance in the primary loop. For this reason, the SA factor was increased until the secondary side outlet temperature reached the expected value as stated in the NuScale FSAR. A final SA factor of 6125.0 is used which achieves the correct outlet temperature and an energy balance in the primary loop is obtained.

The discrepancies in the SA factor of the heat structure connecting the primary and secondary side of the SG could be attributed to several factors. Firstly, the heat transfer rate of helical coil heat exchangers is typically higher than that of straight pipe heat exchangers. Skolik *et al.* (2021) increased the heat transfer area of the straight pipe SG model by ~ 30 % to achieve an adequate heat removal, while further adjusting the feedwater flow rate. Hoffer *et al.* (2011) applied a heat transfer multiplier to the model when modelling a helical coil SG as a straight pipe, while making further adjustments to the heated length and mass flow rates to achieve design temperatures. Prabhanjan *et al.* (2002) has shown that helical coil heat exchangers can provide an increase in the heat transfer coefficient of up to 43 % when compared to straight pipe heat exchangers. Further discrepancies are attributed to a lack of detail in the description of the NuScale SMR

SGs. Details such as the pitch to diameter ratio of the tube bundles and the helical coil radius are currently unknown and could impact the heat transfer.

Feedwater to the SG pipe is provided by a time dependent volume where the water temperature and pressure is specified as seen in Table 3-8, while a time dependent junction controls the flow rate through the SG pipe. Two trip valves located at the inlet and outlet of the SG pipe acts as SG isolation valves. In the case of an accident, these valves close to isolate the SG coils from the remainder of the secondary loop. A secondary set of valves would then open to connect the SG coils to the DHRS heat exchanger. For this study, the DHRS is set to fail and thus the DHRS is omitted from the model. The SG isolation valves are set to close when receiving a low pressurizer pressure signal which has a setpoint of 11.03 MPa. This will occur shortly after the inadvertent opening of the RVV resulting in depressurisation of the RPV. The SG isolation valves remain closed for the remainder of the transient.

**Table 3-8: NuScale SMR steam generator design parameters (NuScale Power LLC., 2020c)**

| Steam generator parameters | | |
|---|---|---|
| Average tube length | 24.2 | m |
| Number of tubes | 1380 | - |
| Total heat transfer area | 1672.25 | $m^2$ |
| OD of tube | 0.0159 | m |
| Tube wall thickness | 0.00127 | m |
| ID of tube | 0.01463 | m |
| Flow area per tube | 0.000168 | $m^2$ |
| Total flow area | 0.232 | $m^2$ |
| Total heat transfer | 159.13 | MWth |
| SG pressure | 3.45 | MPa |
| SG outlet temperature | 580.039 | K |
| SG inlet temperature | 421.872 | K |
| SG flow | 67.068 | kg/s |

### 3.3.4 Containment vessel

The CNV of the NuScale SMR is a large pressure vessel with the RPV located inside. The CNV is located in the reactor coolant pool (UHS) and will transfer heat to the UHS in case of an accident or shutdown of an NPM. The CNV is the depressurisation space for the RPV and the fluid inventory of the RPV will also be partially drained into the CNV in case of a shutdown or accident. Under normal operation the CNV is placed under vacuum which isolates the RPV from the UHS preventing heat from escaping the RPV. Flow paths between the RPV and CNV include two RSVs and three RVVs located at the top of the RPV, as well as two RRVs located in the downcomer just above the core. The operating conditions of the CNV, UHS and reactor building are shown in Table 3-9, with the UHS and reactor building being at atmospheric pressure (100 kPa). It is stated that the pressure of the CNV is set to be less than 0.69 kPa (NuScale Power LLC., 2020d). However, this was increased to 5 kPa for conditions to allow for saturated liquid at initialisation of the model as required by ASYST 3.4. This reduces the vacuum in the CNV from 99.3 % to 95 % and is expected to have no effect on the steady state operation of the model. The model of the CNV with the RPV and UHS is shown in Figure 3-9.

**Table 3-9: NuScale SMR CNV, UHS and reactor building operating conditions.**

| **Containment system operating conditions** | | |
|---|---|---|
| Internal CNV pressure | 5 | kPa |
| CNV temperature | 310 | K |
| UHS pool water volume | 15142 | $m^3$ |
| UHS pool water temperature | 310 | K |
| Reactor building air temperature | 300 | K |

**Table 3-10: Containment vessel model dimensions**

| **Volume** | **Length (m)** | **Flow area ($m^2$)** |
|---|---|---|
| 1 | 0.35 | 8.43 |
| 2 | 2.9 | 2.82 |
| 3 | 2.87 | 9.12 |
| 4 | 3.82 | 8.25 |
| 5 | 3.82 | 8.25 |
| 6 | 3.682 | 8.25 |
| 7 | 4.0 | 14.69 |

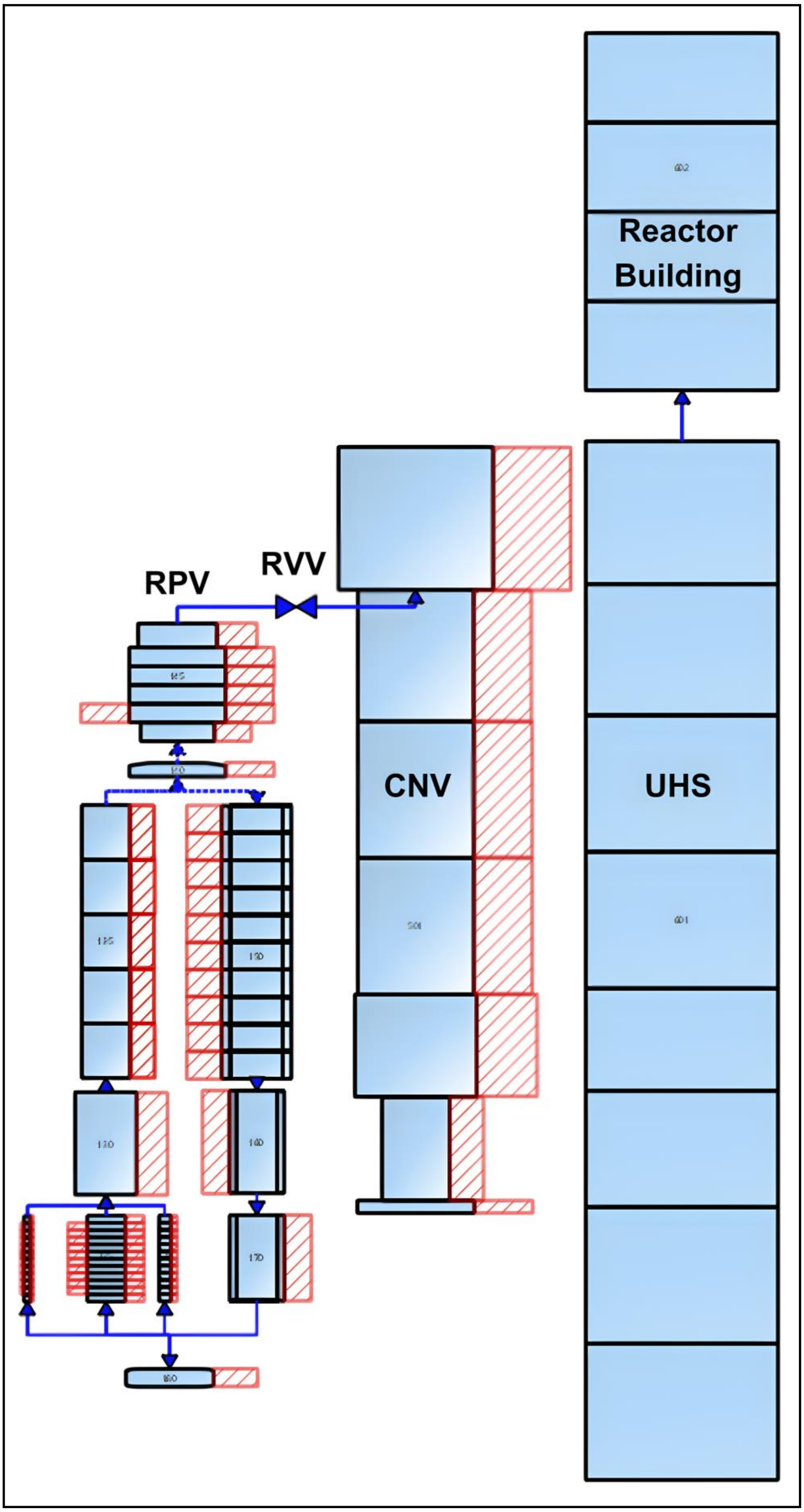


Figure 3-9: NuScale SMR model RPV, CNV, UHS and reactor building

The CNV is modelled using a pipe component with seven volumes. Volume lengths are once again taken from the study done by Skolik *et al.* to match the volume lengths used for the RPV model (Skolik *et al.*, 2021). Volume lengths match the volume lengths of the downcomer in the RPV. However, certain sections are lumped together to reduce the number of volumes of the CNV. Volume flow areas are calculated from the CNV and RPV dimensions found in the NuScale FSAR (NuScale Power LLC., 2020b, 2020d). Heat structures also exist between the RPV and CNV with the dimensions of the RPV wall as seen in Table 3-6. Volume no. 1 is the region of the CNV below the RPV. Volume no. 2 -6 represents the annular space formed between the RPV outer wall and CNV inner wall. Volume no. 2 is the section of the CNV surrounding the lower plenum and lower downcomer, while volume no. 3 surrounds the middle downcomer. Volumes no. 4 and 5 surrounds the upper downcomer with volume no. 6 surrounding the upper plenum and pressurizer. Lastly, volume no. 7 is the space above the RPV.

A heat structure connects the CNV to the UHS to represent the CNV wall. The heat structure only represents the cylindrical outer wall of the CNV and does not include the top and bottom of the CNV. The dimensions of the heat structure for each of the seven volumes of the CNV is shown in Table 3-11 as taken from the NuScale FSAR (NuScale Power LLC., 2020d).

**Table 3-11: CNV heat structure dimensions**

| Volume | ID (m) | OD (m) |
|---|---|---|
| 1 | 1.638 | 1.715 |
| 2 | 1.638 | 1.715 |
| 3 | 2.165 | 2.248 |
| 4 | 2.162 | 2.248 |
| 5 | 2.162 | 2.248 |
| 6 | 2.162 | 2.248 |
| 7 | 2.162 | 2.248 |

### 3.3.5 Reactor vent valve

The RVV included in this model forms part of the ECCS along with an additional two RVVs and two RRVs. The three RVVs are located at the top of RPV and will vent steam from the pressurizer directly into the CNV when opened. Two RRVs connect the RPV and CNV just above the core and allow for condensed coolant in the CNV to re-enter the RPV. For this study, the selected transient is initiated by the inadvertent opening of one RVV, while the ECCS is assumed to fail. Thus, the additional two RVVs and two RRVs will remain closed for the remainder of the transient. For this reason, only one RVV is included in the model with the other two RVVs and two RRVs being omitted.

The valve component used for the RVV is similar to a junction component and connects the top face of the pressurizer to the bottom face of the seventh volume of the CNV. A trip valve component is used and the flow area is set to 0.016 $m^2$ (Skolik *et al.*, 2021). The trip valve is initially closed and will open instantly when the trip setpoint is reached. The flow model flags used for the valve is choking set to “on” and the homogeneous flow option is used as prescribed by the RELAP5/MOD3 code manual. The full abrupt area change model is also used (Idaho National Engineering Laboratory, 1995).

### 3.3.6 UHS and reactor building

The UHS and reactor building are represented by two pipe components numbered 601 and 602 respectively as seen in Figure 3-9. The dimensions of the UHS and reactor building are shown in Table 3-12 based on dimensions taken from the model by Skolik *et al.* and the NuScale FSAR (NuScale Power LLC., 2020d; Skolik *et al.*, 2021). The UHS has the same volume lengths as the volumes of the CNV, with the addition of two volumes that extend below the CNV representing the 7.64 m space from the bottom of the CNV to the UHS floor. The flow area of the UHS for this model is one twelfth of the flow area of the entire UHS due to only one of twelve NuScale SMRs being modelled. The coolant level of the UHS is set to be slightly above the top of the RPV, with volume no. 8 in pipe 601 set to have a static quality of 0.5 which rises to 0.6 shortly after initialisation of the simulation.

The reactor building has a length of 20 m and is divided into four sections, while the flow area is assumed to be the same as the UHS. The reactor building is filled with air and thus the static quality is set to 1.0 at the start of the simulation. The UHS and reactor building are connected with a single junction.

**Table 3-12: UHS & reactor building model dimensions.**

| UHS pipe 601 volumes | Length (m) | Flow area ($m^2$) |
|---|---|---|
| 1 | 3.82 | 567.74 |
| 2 | 3.82 | |
| 3 | 3.25 | |
| 4 | 2.87 | |
| 5 | 3.82 | |
| 6 | 3.82 | |
| 7 | 3.667 | |
| 8 | 4.0 | |
| **Reactor building pipe 602** | **Length per volume (m)** | **Flow area ($m^2$)** |
| 4 volumes | 5.0 | 567.74 |

### 3.3.7 Control systems

The NuScale SMR uses a complex set of systems for control and operation of the reactor. However, for this model the control systems were dramatically simplified, and the only systems that are included are those that are crucial to achieve steady state operation and replicate the selected accident transient. Trips, general tables, time dependant junctions, and time dependant volumes are used to control the reactor model. The trips used in this model is shown in Table 3-13. Three variable trips are used and the trip number, measured parameter, volume where the parameter is measured, relationship, and the setpoint value for the trips are shown. Variable trips are either true or false. For example, trip 401 will be true when the pressure in the second volume of component 145 (pressurizer) is less than 12.75 MPa. Trip 402 does not have an associated volume number as time is a universal parameter. One logical trip is used with a trip number of 601 and considers trips 401 and 403 and uses the “and” operator, meaning both trips 401 and 403 must be true for trip 601 to be true.

The pressurizer heating elements are controlled by a general table linked with trip 601 which is true only when both trips 401 and 403 are true. Both trips consider the pressure in the second volume of the pressurizer as this is where the heating elements are located. The combination of these two trips results in trip 601 being true if the pressure is between 11.03 and 12.75 MPa. The general table is set to have zero power at the start with an instantaneous jump to 800 kW which is the maximum power of the heating elements. The initial pressure of the primary loop is set to 12.75 MPa with the primary loop having a negative power balance, meaning pressure will decrease without the use of the pressurizer. The heating elements switch on, increasing the pressure back to 12.75 MPa, and then the heating elements will switch on and off to maintain this pressure. A lower pressure limit of 11.03 MPa is used to switch the pressurizer off shortly after the start of the transient where the RPV was depressurised.

**Table 3-13: NuScale SMR model control system trips**

| | | **Variable trips** | | |
|---|---|---|---|---|
| **Trip number** | **Parameter** | **Volume no.** | **Relationship** | **Value** |
| 401 | Pressure (MPa) | 145-02 | less than | 12.75 |
| 402 | Time (s) | - | greater than | 10000.0 |
| 403 | Pressure (MPa) | 145-02 | greater than | 11.03 |
| | | **Logical trips** | | |
| **Trip number** | **Trip 1** | **Operator** | **Trip 2** | |
| 601 | 401 | and | 403 | |

The core power during steady state operation and the accident transient is controlled by a general table linked to trip 402, which also controls the RVV. Trip 402 is set to be true when the simulation time goes beyond 10000 s with the transient being initiated by the opening of the RVV at this time and the core following the predetermined accident transient power profile from this time onward. Steady state power of the core was reduced from 160 MW to 159 MW to achieve a better energy balance in the primary loop and achieve the desired core outlet temperature and primary loop mass flow. Five seconds after initiation of the transient, the core is set to trip and the power level decreases to decay power levels. The reactor power can be seen in Figure 3-10 and Figure 3-11 as taken from the study by Skolik *et al.* (2021).

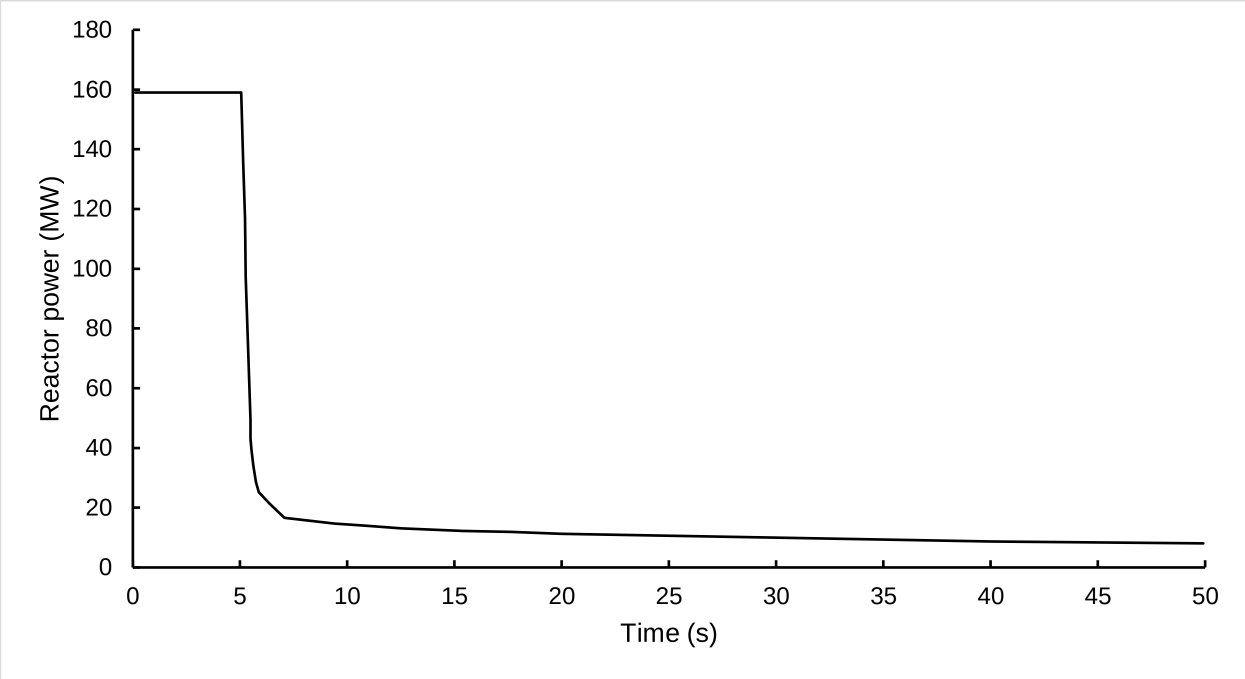


**Figure 3-10: Reactor power (short term)**

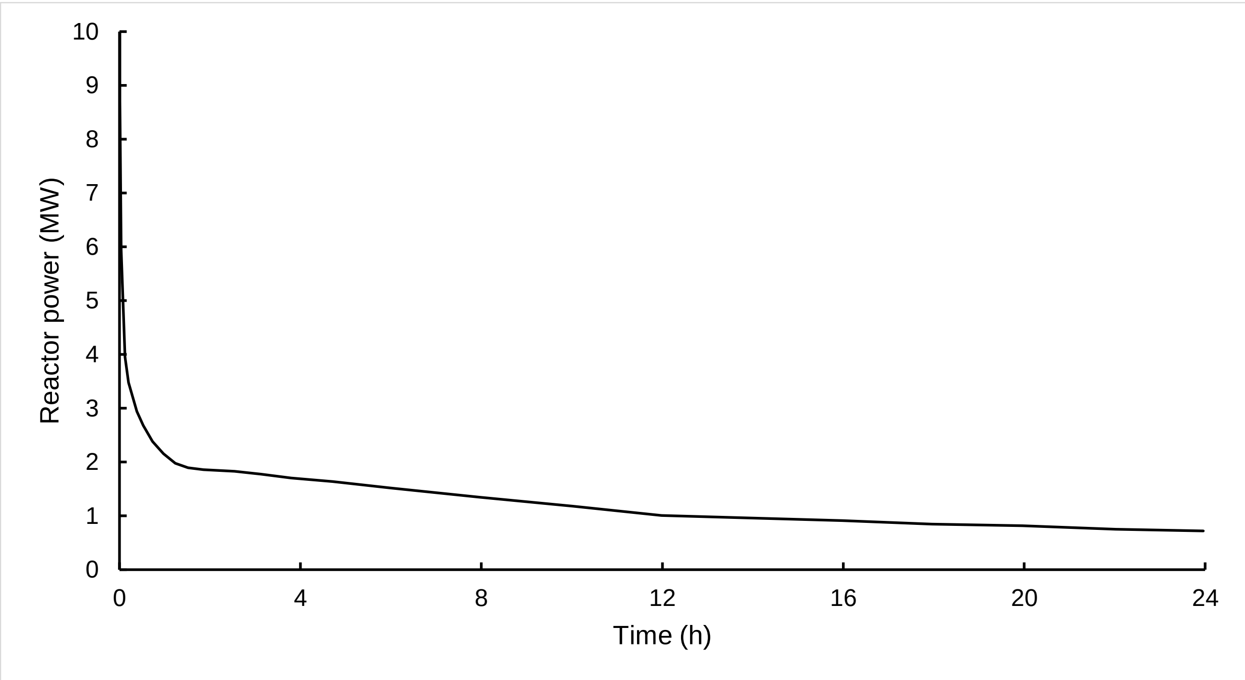


**Figure 3-11: Reactor power (long term)**

### 3.3.8 Material properties

ASYST 3.4 requires two properties to characterise a given material, which is the thermal conductivity and volumetric heat capacity. The volumetric heat capacity (J/m$^3$-K) is calculated by multiplying the density (kg/m$^3$) with the specific heat capacity (J/kg-K). The thermal conductivity and volumetric heat capacity are not constant values, but rather functions of temperature. These properties are input in table format with

ASYST 3.4 then interpolating for temperature in between the given data points. The surface roughness of materials which interact with the coolant is also required.

#### 3.3.8.1 Cladding materials

The properties of candidate ATF cladding materials FeCrAl and SiC compared to Zr-alloy were discussed in Section 2.1. For Zr-alloy the thermal conductivity and specific heat capacity are given as functions of temperature, with the volumetric heat capacity then calculated by multiplying the specific heat capacity by a constant density of 6560 kg/m$^3$ (US NRC, 2014). The peak in the volumetric heat capacity of Zr-alloy as seen in Figure 3-12 is attributed to a phase change from Alpha to Beta phase at a temperature of 1139 K (Arblaster, 2013).

The FeCrAl alloy used in this case is B136Y alloy developed by Oak Ridge National laboratory (ORNL) and containing 6 % Al and 13 % Cr as well as small quantities of Mo, Si and Nb (Gurgen and Shirvan, 2018). The thermal conductivity of B136Y alloy is given in Equation 3-1,

$$k(T) = -9.184 \times 10^{7} T^{2} + 1.368 \times 10^{-2} T + 8.187 \ \ [W/m.K] \qquad (3\text{-}1)$$

Where $T$ is the temperature in Kelvin at the geometric mesh point and $k(T)$ is the thermal conductivity.

The specific heat capacity of B136Y alloy can be seen in Equation 3-2, with coefficients shown in Table 3-14. A sharp peak exists in the specific heat capacity of B136Y alloy. This is due to a phase change from the ferromagnetic to the paramagnetic state. For this reason, the specific heat as a function of temperature is divided into two regions with the transition occurring at the Curie temperature $T_C$. The density of B136 alloy is given by Equation 3-3 with T being the temperature in K (Gurgen and Shirvan, 2018).

$$C_p(T) = \begin{cases} AT + BT^2 + CT^3 & T \leq T_C \\ AT + BT^2 + CT^3 + \dfrac{D}{T} + E\ ln\left(\dfrac{abs(T - T_C)}{T_C}\right) & T > T_c \end{cases} \quad \frac{J}{kg.K} \qquad (3\text{-}2)$$

**Table 3-14: Coefficients for Equation 2-2 (Gurgen and Shirvan, 2018)**

| Temperature range (K) | $A\ (\frac{J}{kg})$ | $B\ \left(J.\frac{K}{kg}\right) \times 10^{-3}$ | $C\ \left(J.\frac{K^2}{kg}\right) \times 10^{-6}$ | $D\ \left(J.\frac{K^2}{kg}\right) \times 10^{3}$ | $E\ (\frac{J}{K.kg})$ | $T_c\ (K)$ |
|---|---|---|---|---|---|---|
| $300 < T < T_c$ | $2.995 \pm 0.006$ | $-5.953 \pm 0.021$ | $4.516 \pm 0.018$ | - | - | 771 |
| $T_c < T < T_m$ | $1.456 \pm 0.012$ | $-1.296 \pm 0.017$ | $0.438 \pm 0.007$ | $-26.45 \pm 1.09$ | $-77.09 \pm 0.01$ | 771 |

$$\rho = 7260 - 0.5333T \quad (kg/m^3) \tag{3-3}$$

The surface roughness of Zr-alloy and FeCrAl are 1.61 µm and 4.53 µm respectively (Lee *et al.*, 2019). Properties of SiC are taken from Figure 2-1 and Figure 2-2, with a constant density of 2580 kg/m³ used to calculate the volumetric heat capacity (Katoh *et al.*, 2014; Yu *et al.*, 2020). The surface roughness of the SiC cladding is taken as the surface roughness of SiC manufactured with chemical vapour deposition (CVD) which is ~ 1.0 µm (Kim and Choi, 1997). The thermophysical properties of the three cladding materials are shown in Figure 3-12.

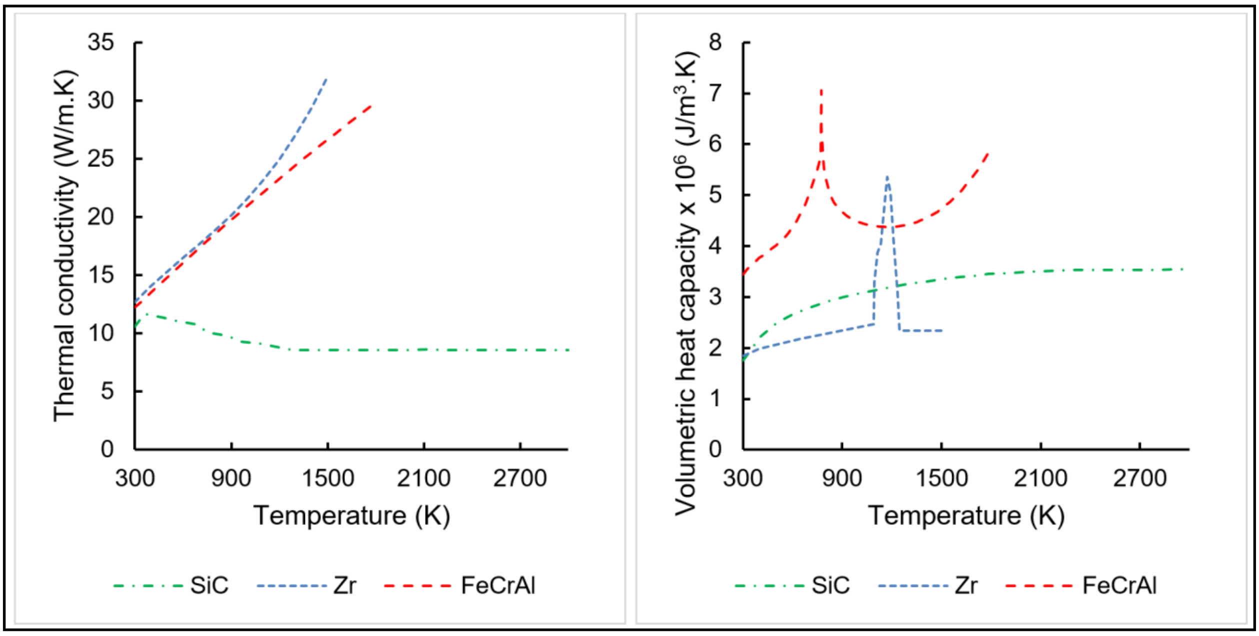


**Figure 3-12: Thermophysical properties of cladding materials**

### 3.3.8.2 $UO_2$ fuel

Thermophysical properties of $UO_2$ fuel is shown in Figure 3-13. Temperature correlations were given for the thermal conductivity, specific heat capacity and density for the temperature range of 300 K to 3100 K (Popov *et al.*, 2000).

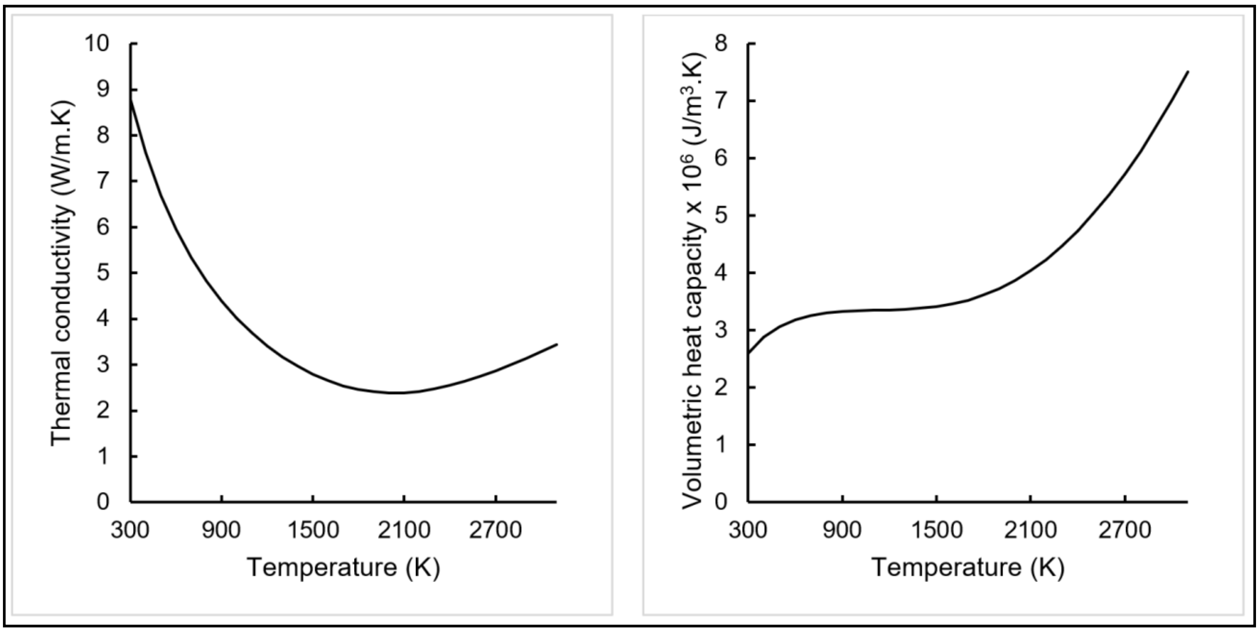


**Figure 3-13: Thermophysical properties of $UO_2$ (Popov *et al.*, 2000)**

#### 3.3.8.3 Alloy 690

The SG tubes used in the NuScale SMR are made of SB-163 Alloy 690 (UNS N06690) (NuScale Power LLC., 2020c). The properties of Inconel Alloy 690 were used in the current study, as this is a commercially available version of the same alloy and its thermophysical properties can be obtained easily. Temperature correlations for the thermal conductivity and specific heat capacity were given, with the volumetric heat capacity calculated by using a constant density of 8190 kg/m$^3$ (Special Metals Corporation, 2019). The material is used in the heat structure connecting the upper downcomer to the SG pipe. A surface roughness of 0.3 µm is used which is applied to the SG pipe and the upper downcomer. The thermophysical properties of Alloy 690 can be seen in Figure 3-14.

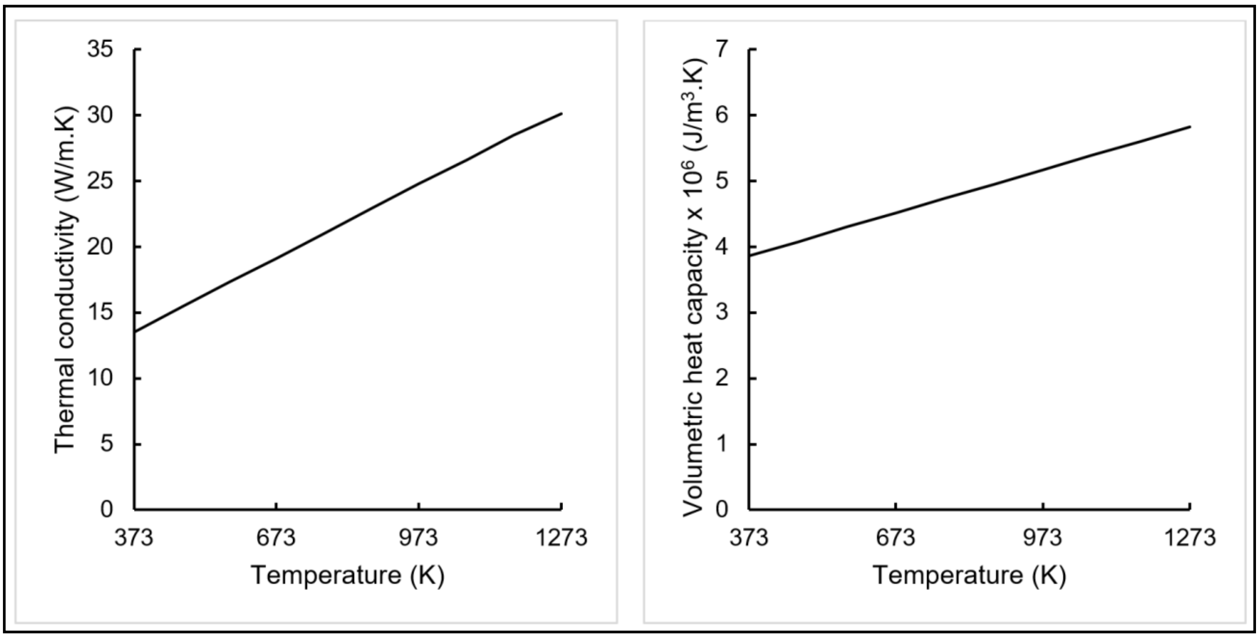


**Figure 3-14: Thermophysical properties of Alloy 690 (Special Metals Corporation, 2019)**

#### 3.3.8.4 SA-508 low alloy steel

The majority of the RPV and large sections of the CNV are made of SA-508 low alloy steel (NuScale Power LLC., 2020c, 2020d). Temperature correlations are given for the thermal conductivity, specific heat capacity and density (Jung *et al.*, 2015). The material is used for the RPV wall, all internal structures of the RPV and the CNV wall. The thermophysical properties of SA-508 are shown in Figure 3-15. The peak in the volumetric heat capacity of SA-508 is due to the phase transition from alpha to gamma phase at ~ 1000 K.

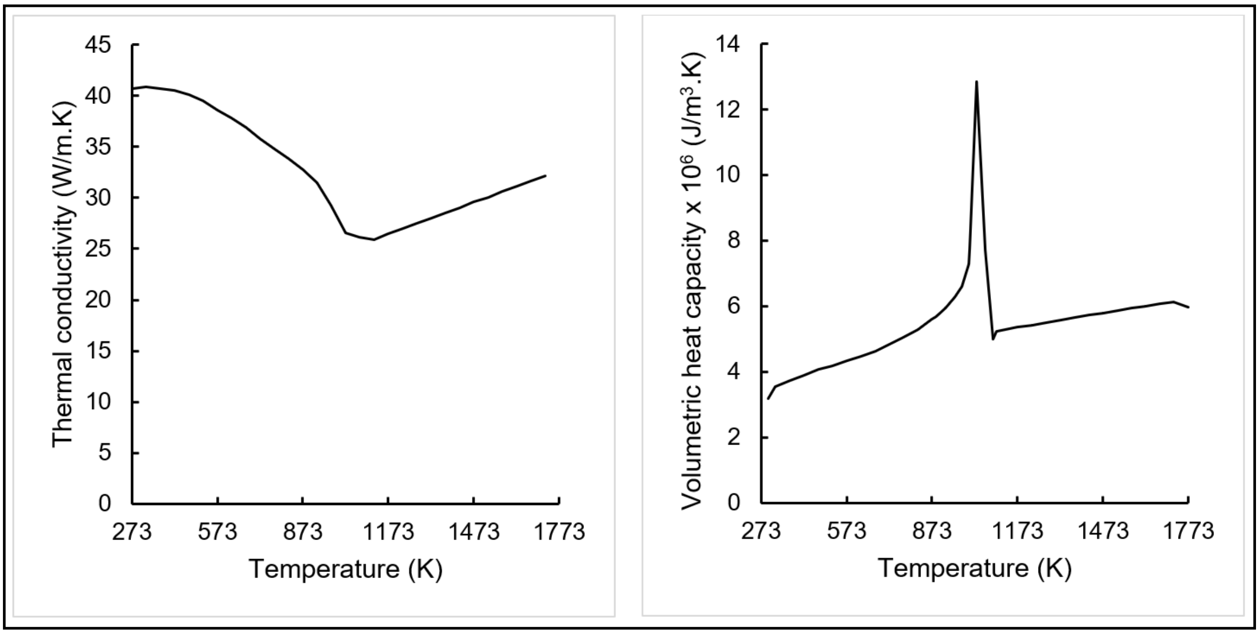


**Figure 3-15: Thermophysical properties of SA-508 (Jung *et al.*, 2015)**

#### 3.3.8.5 Helium

The thermophysical properties of helium are taken from Engineering Equation Solver (EES) (F-Chart Software, 2023). The density, thermal conductivity and specific heat capacity are calculated using EES over a temperature range at a constant pressure of 2.0 MPa. The equations of state for helium in EES is valid for temperatures of up to 1500 K. However, for the current study the temperature of helium is expected to rise close to the melting point of $UO_2$. Thermophysical properties of helium over the required temperature range at the specified pressure is also not available. Thus, the equations of state of helium in EES is assumed to be valid for the temperature range of 300 K to 3300 K. During the development of the model problems were observed in the temperature of the central node of the helium in the fuel pin heat structure. Large temperature fluctuations occurred in the temperature at this point. This problem was most likely due to an issue with interpolation and the problem was resolved by reducing the number of data points given in the input. Data points for thermal conductivity was given at 300 K, 1500 K and 3300 K. Data points for volumetric heat capacity were given at 300 K, 500 K, 1500 K and 3300K. The thermophysical properties of helium are shown in Figure 3-16, with the data used as input shown as a solid line and the actual data shown as a dotted line.

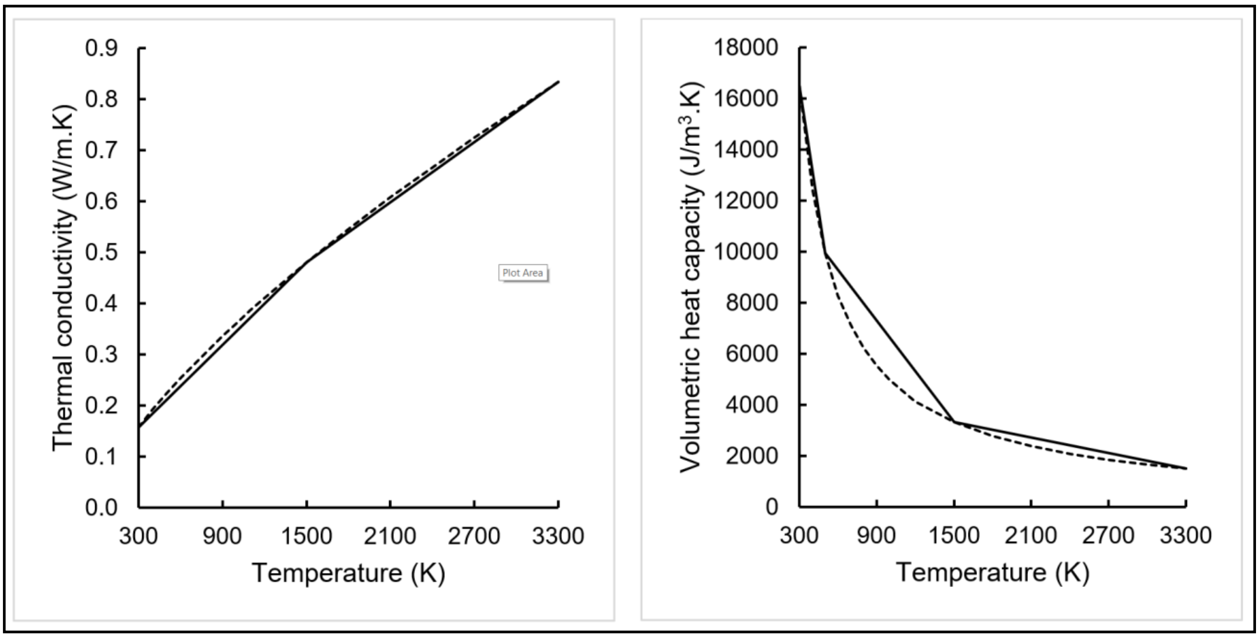


**Figure 3-16: Thermophysical properties of Helium**

## 3.4 Model verification and validation

The reference model will be verified using data taken from the NuScale FSAR and various articles from academic journals. The data used for verification are all based on simulations of the NuScale SMR as there are no experimental data available for this reactor. All data taken from the NuScale FSAR will from here onward be labelled as "Scenario 1" (NuScale Power LLC., 2020b, 2020c, 2020d, 2020e). The results taken from the study done by Skolik *et al.* (2021) will be labelled as "Scenario 2". Data gathered during the current study will be labelled with "ASYST 3.4". All other literature used will be referenced individually.

In the study by Skolik *et al.* (2021), the model was developed and verified with data from the NuScale FSAR, with revision four of the NuScale FSAR published in January 2020 being referenced. Revision five of this document published in July 2020 was used in the current study. Most steady state parameters remained the same between revision four and five of the NuScale FSAR, and there are no observable differences in the selected transient between the two revisions. However, there are several discrepancies between data taken directly from the FSAR (revision 4 or 5) and the data from the FSAR as presented by Skolik *et al.* (2021). To distinguish between these results, data taken from the FSAR as presented by Skolik *et al.* (2021) will be referred to as "Scenario 3".

### 3.4.1 Steady state operation

The main steady state parameters used to evaluate the NuScale SMR thermal-hydraulic performance is shown in Table 3-15 and compared with data taken from the NuScale FSAR and two articles (Fakhraei *et al.*, 2020; Skolik *et al.*, 2021). Some values are fixed as they are used as input parameters or controlled by the reactor control system. These values are the core thermal power, RPV pressurizer pressure, SG secondary inlet temperature, SG pressure and SG feedwater flow rate. The time-dependent volume at the outlet of the SG was set to a pressure of 3.45 MPa. However, the pressure taken from the lowest volume of the SG pipe was slightly higher at 3.51 MPa due to the pressure difference over the steam generator. A percentage error is also calculated for each data set compared to the data set gathered in this study.

The core outlet temperature of all four data sets agrees with each other with small errors. A larger difference can however be seen in the core inlet temperature when compared with Scenario 1. This leads to a large error of 9.12 % in the core temperature rise. The core inlet temperature found in Scenario 1 is difficult to replicate without changing other important parameters, as many of the parameters are dependent on each other. Scenario 2 was able to better replicate the core inlet temperature of the FSAR but has a lower coolant flow rate on the primary side and higher SG feedwater flow rate. The core inlet temperature and core temperature rise of the ASYST 3.4 model better aligns with the model of Fakhraei *et al.* (2020), while having a similar coolant flow. The higher core inlet temperature of the current model is therefore acceptable.

The SG secondary outlet temperature is very similar to that of Scenario 1 whereas the value from Scenario 2 has a larger error. Skolik *et al.* (2021) does however list the SG outlet temperature from the FSAR as 574.8 K (Scenario 3), which is much closer to the value obtained by Skolik *et al.* (2021). This different value might have been taken from an older revision of the FSAR. The SG outlet temperature of the model by Fakhraei *et al.* (2020) was not given.

**Table 3-15: Steady state parameters**

| Parameter | ASYST 3.4 | Scenario 1 | Error % | Scenario 2 | Error % | (Fakhraei *et al.*, 2020) | Error % |
|---|---|---|---|---|---|---|---|
| Core thermal power (MW) | 159 | 160 | 0.63 | 160 | 0.63 | 158.1 | 0.57 |
| Core outlet temperature (K) | 586.73 | 587.04 | 0.05 | 585.1 | 0.28 | 586 | 0.12 |
| Core inlet temperature (K) | 536.24 | 531.48 | 0.90 | 531.9 | 0.82 | 535.9 | 0.06 |
| Core temperature rise (K) | 50.49 | 55.56 | 9.12 | 53.2 | 5.09 | 50.1 | 0.78 |
| SG secondary inlet temperature (K) | 421.87 | 421.87 | 0.00 | 422 | 0.03 | 421.9 | 0.01 |
| SG secondary outlet temperature (K) | 579.76 | 580.04 | 0.05 | 574.79 | 0.86 | - | - |
| RPV pressurizer pressure (MPa) | 12.75 | 12.76 | 0.12 | 12.8 | 0.43 | 12.754 | 0.07 |
| SG pressure (MPa) | 3.51 | 3.45 | 1.79 | 3.45 | 1.79 | 3.45 | 1.79 |
| Coolant flow rate (kg/s) | 587.31 | 587.15 | 0.03 | 567 | 3.58 | 590.4 | 0.52 |
| SG feedwater flow rate (kg/s) | 67.07 | 67.07 | 0.0 | 70 | 4.19 | 67.2 | 0.20 |

### 3.4.2 Accident transient

Two sets of results are used to verify the transient behaviour of the current model. The selected transient is the inadvertent opening of a single RVV without use of the ECCS and DHRS. The first set of results is taken from the NuScale FSAR (Scenario 1) and involves the inadvertent opening of a single RVV with successful operation of the ECCS. One RVV is opened at the start of the transient with the ECCS successfully opening the remaining two RVVs and two RRVs after 3925 s. The operation of the DHRS is excluded from this transient. Thus, the transient is the same as the transient in the current study for the first 3925 s (NuScale Power LLC., 2020a).

The second set of results is taken from the study done by Skolik *et al.* (Scenario 2) which the model and transient in the current study is based on. The model by Skolik *et al.* is however more complex than the model developed for the current study as it includes a more complex core which allows for oxidation and melting of core materials. The simulation of Skolik *et al.* is also running for 24 hours which is far past the point of failure of the cladding and fuel materials, while simulations in the current study are terminated at the point of failure of the cladding materials. A third set of data is included (Scenario 3) which is the results from the NuScale FSAR presented by Skolik *et al.* (2021), which is included due to the discrepancies between these results and Scenario 1.

The transient sequence of events is shown in Table 3-16 with the ASYST 3.4 model being compared with that of Scenarios 1, 2 and 3. All three scenarios are initiated by the opening of a single RVV. The low pressurizer pressure signal is triggered after one second in both ASYST 3.4 and Scenario 2, while this takes place after only 0.5 s in Scenario 3. Reactor trip of ASYST 3.4 and Scenario 2 both happen after 5 s, while Scenario 1 is faster at 2.3 s and Scenario 3 takes 4.5 s. Maximum CNV pressure in ASYST 3.4 occurs much sooner than both Scenarios 2 and 3, with the pressure being in between that of Scenarios 2 and 3. However, the time of maximum CNV pressure aligns more with that of Scenario 1. ECCS actuation happens after 3925 s in Scenario 1 and 759 s in Scenario 3, which mitigates the accident, and the transient is terminated after 4500 s in both cases. ECCS actuation in Scenario 2 fails and the accident is free to progress resulting in oxidation of the cladding starting after 4.5 h with core damage after 4.8 h. In the case of the ASYST 3.4 model, ECCS actuation is also set to fail with core damage happening after 6.42 h. This is a 1.6-hour delay compared to Scenario 2. The discrepancies between Scenarios 1 and 3 include the time of reactor trip, maximum CNV pressure and ECCS actuation.

**Table 3-16: Transient sequence of events (NuScale Power LLC., 2020a; Skolik *et al.*, 2021)**

| Event | ASYST 3.4 | Scenario 1 | Scenario 2 | Scenario 3 |
|---|---|---|---|---|
| RVV opens | 0 s | 0 s | 0 s | 0 s |
| Low pressurizer pressure signal (11.03 MPa) | 1 s | - | 1 s | 0.5 s |
| Reactor trip | 5 s | 2.3 s | 5 s | 4.5 s |
| Maximum CNV pressure | 53s (5.03 MPa) | 52 s | 77 s (4.18 MPa) | 67 s (5.52 MPa) |
| ECCS actuation | - | 3925 s | - | 759 s |
| Cladding oxidation starts | - | - | 4.5 h | - |
| Core damage (>1477 K) | 6.41 h | - | 4.8 h | - |
| Simulation terminated | at cladding failure or 24h | 4500 s | 24 h | 4500 s |

For the current study, a maximum time step of 0.1 s was used for the entire simulation. This is the default maximum time step in ASYST 3.4 and caused no errors during initialisation of the problem. A minimum time step of $1.0 \times 10^{-7}$ s was found to be adequate for the majority of the transient. However, thermodynamic property errors occurred during two phases of the transient. These phases were most likely the periods where the fluid level transitioned from the upper riser to the middle riser, and from the middle riser to the core section. Thus, the minimum time step was gradually decreased to overcome the thermodynamic property errors. A final minimum time step of $1.0 \times 10^{-10}$ s was used for the entire duration of the transient.

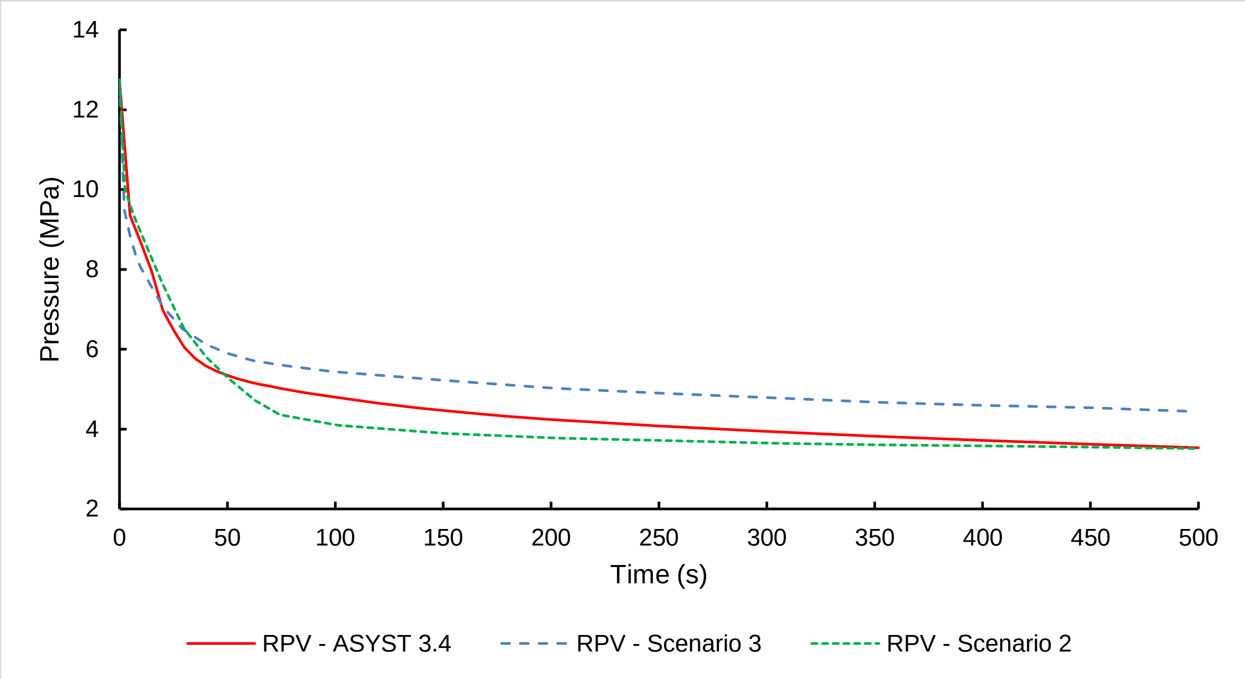


**Figure 3-17: RPV pressure**

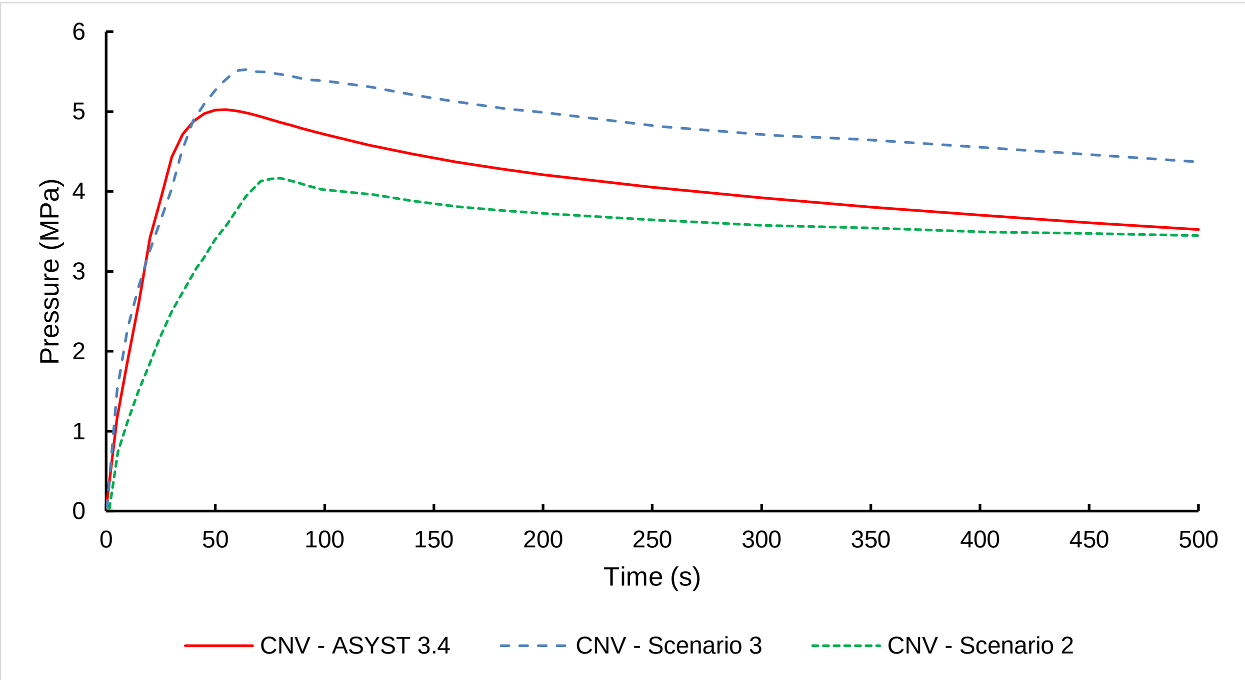


**Figure 3-18: CNV pressure**

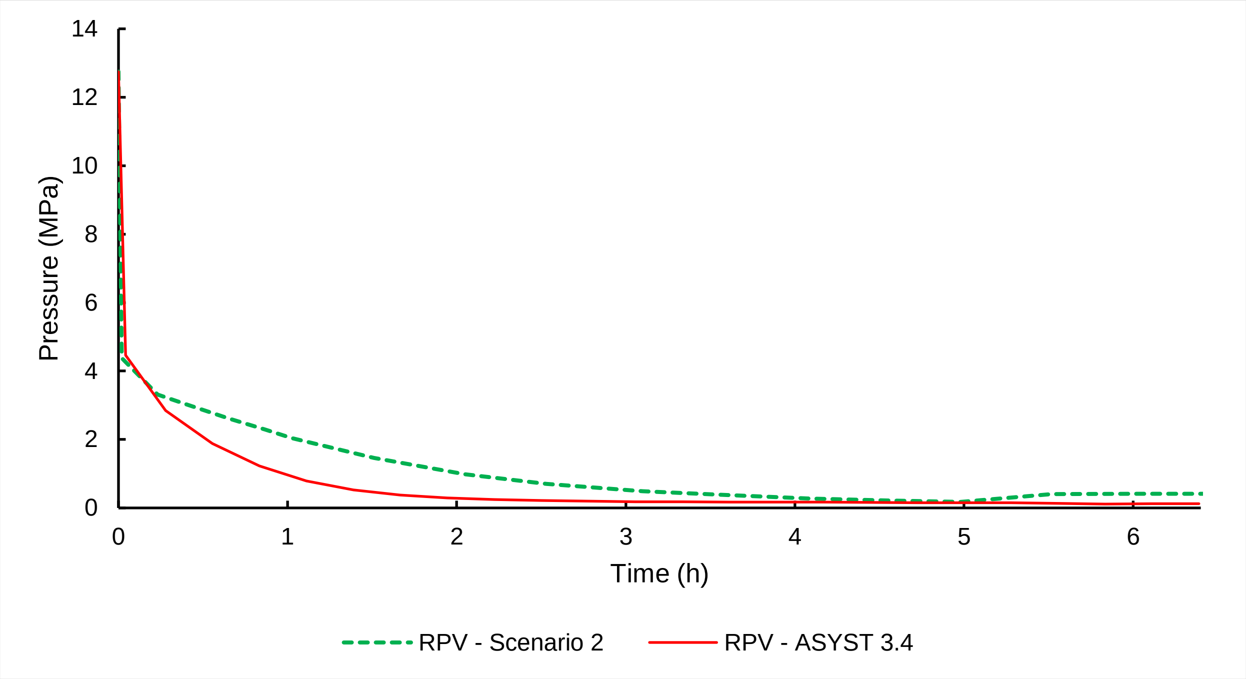


**Figure 3-19: RPV pressure until termination**

Figure 3-17 and Figure 3-18 show the RPV and CNV pressures, respectively, for the first 500 s of the transient. The general trend of depressurisation of the RPV down to 7 MPa is similar for all three scenarios, whereafter the pressures diverge to meet the corresponding rise in CNV pressure. For the three scenarios, the RPV and CNV pressures equalises roughly at the point of maximum CNV pressure, which was shown in Table 3-16. In the case of ASYST 3.4, the CNV maximum pressure was reached earlier than that of Scenario 2 and 3, with the pressure being in between that of Scenarios 2 and 3 after 100 s. After the initial depressurisation, a downward trend is observed in the RPV pressure of ASYST 3.4, and it nearly matches the RPV pressure of Scenario 2 after 500 s.

Figure 3-19 shows the RPV pressures for ASYST 3.4 and Scenario 2 for the remainder of the ASYST 3.4 transient until termination. The downward trend of the ASYST 3.4 RPV pressure is visible with the pressure decreasing faster in the first hour compared to Scenario 2. The ASYST 3.4 pressure stabilises after roughly two hours where the Scenario 2 pressure steadily decreases. After five hours the pressure is 1.76 MPa and 1.51 MPa for Scenario 2 and ASYST 3.4, respectively. The pressure of Scenario 2 starts to increase at five hours most likely due to heat generated from oxidation which is not included in the ASYST 3.4 model.

Several factors could contribute to the difference in RPV pressure between ASYST 3.4 and Scenario 2 over the first few hours of the transient. The RVV in ASYST 3.4 is set to use the default choked flow model as with Scenario 2. However, it is not specified whether the homogeneous or nonhomogeneous flow model is used for the valve in Scenario 2. Other discrepancies could include parameters such as differences in RPV and CNV dimensions, pressurizer initial water level and pressure, SG feedwater parameters and CNV parameters. Finally, a heat structure representing the RPV wall was not included in the model of Scenario 2 as in the case of the ASYST 3.4 model. This could contribute to increased energy removal from the RPV resulting in lower pressures (Skolik *et al.*, 2021).

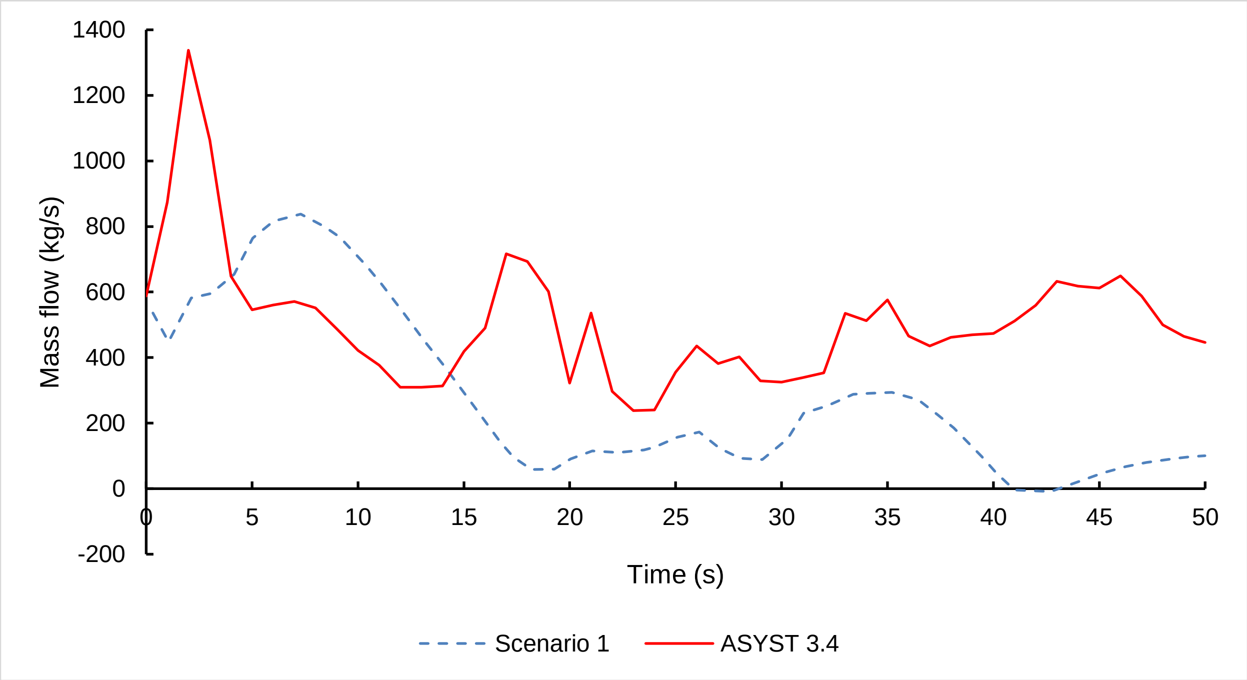


**Figure 3-20: RCS flow (50 s)**

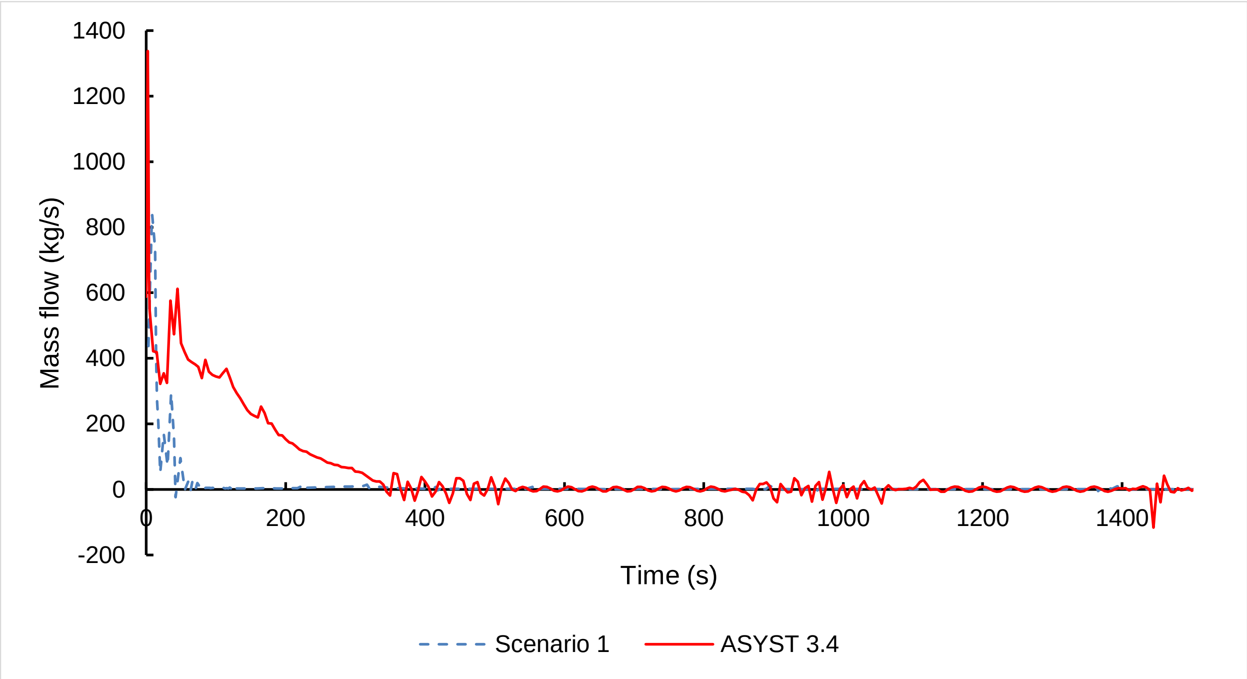


**Figure 3-21: RCS flow (1500 s)**

Figure 3-20 and Figure 3-21 show the reactor coolant system (RCS) flow for the first 50 s and 1500 s respectively. The RCS flow of Scenario 1 has an initial increase in the first ten s of the transient at which point it starts decreasing, with the flow reversing in the negative direction between 40 and 45 s. The RCS flow of ASYST 3.4 rapidly increases to a peak of 1337.55 kg/s at two seconds and decreases back to below 600 kg/s within five seconds. The flow is unstable during the first 50 s of the transient and a higher RCS flow is maintained during this period compared to Scenario 1. The RCS flow of Scenario 1 rapidly decreases in the first 100 s after which point a mass flow of less than 5 kg/s is maintained with occasional oscillations.

In contrast, the RCS flow of ASYST 3.4 is still high after 100 s (~350 kg/s) and gradually decreases to zero at ~ 350 s, at which point larger mass flow oscillations start to occur. These mass flow oscillations appear periodically up to 1500 s, after which point a steady mass flow of less than 2 kg/s is maintained for the remainder of the transient.

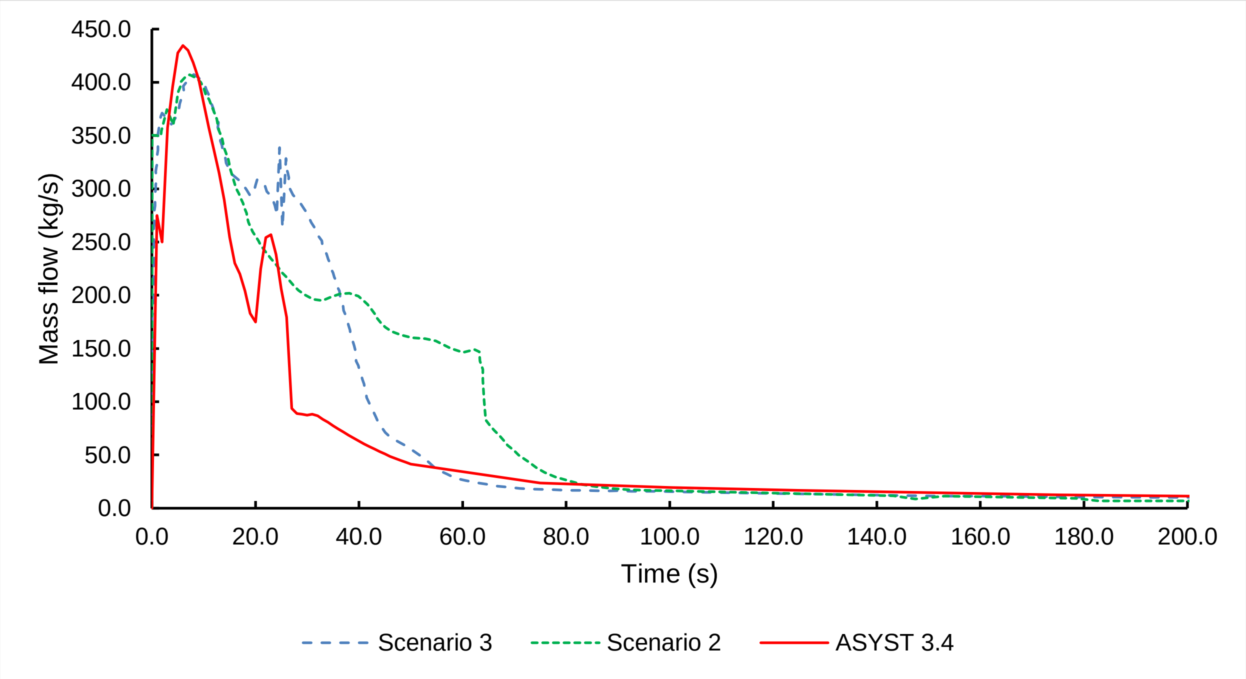


**Figure 3-22: Break flow**

Figure 3-22 shows the break flow through the RVV at the start of the transient. All three scenarios exhibit an initial peak in the break flow with ASYST 3.4 having a higher peak of 427.63 kg/s but a faster decrease in break flow. All three scenarios follow a different break flow profile after the initial peak flow, but the break flow is similar after 100 s. These differences can once again be attributed to the discrepancies in the RVV flow model, system parameters and CNV dimensions (Skolik *et al.*, 2021).

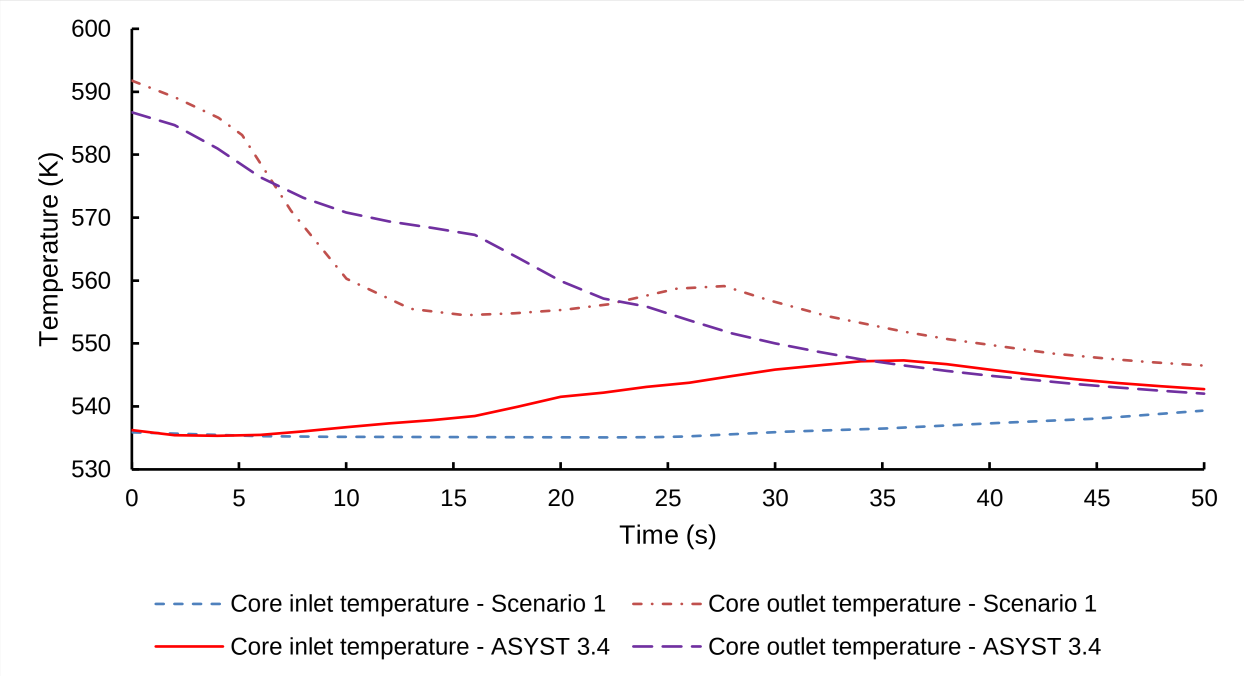


**Figure 3-23: RCS temperature (50 s)**

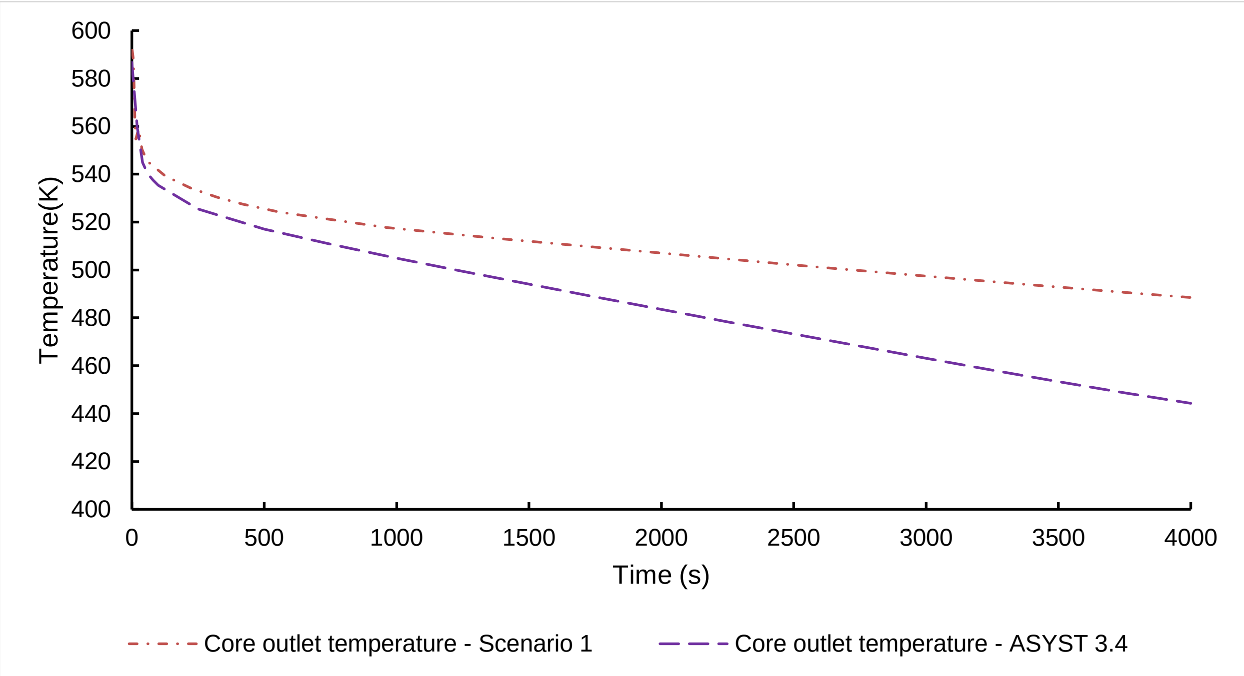


**Figure 3-24: RCS temperature (4000 s)**

Figure 3-23 and Figure 3-24 show the RCS temperature for the first 50 s and 4000 s of the transient, respectively. The reduction in RCS temperature is largely due to the depressurisation of the RPV at the start of the transient. The difference in core inlet and outlet temperature is reduced as the reactor power is reduced from 160 MW to the decay power of less than 15 MW after 10 s. The ASYST 3.4 core outlet temperature rapidly decreases while the core inlet temperature increases, and the temperatures equalise at 35 s and 546 K. The core inlet and outlet temperature of Scenario 1 has a more gradual change and equalises beyond 50 s. Over a period of 4000 s the ASYST 3.4 core outlet temperature has a more significant decrease compared to that of Scenario 1. This downward trend is similar to the pressure response of the ASYST 3.4 RPV as seen in Figure 3-17 and Figure 3-19.

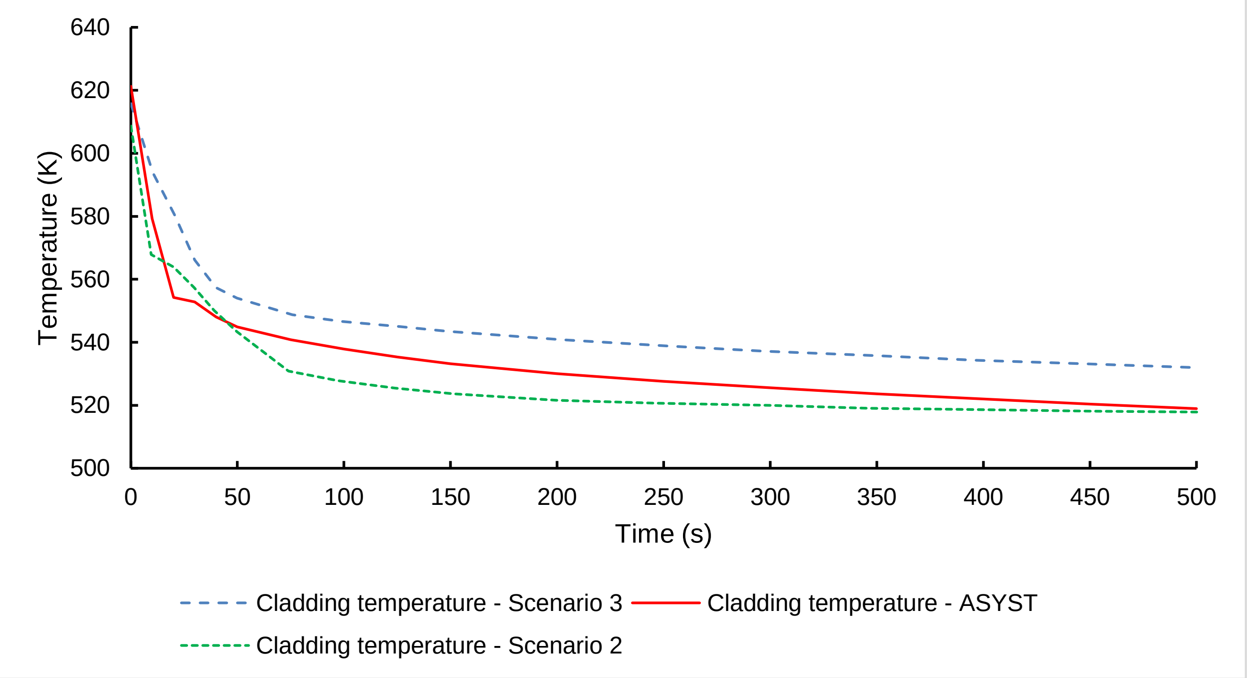


**Figure 3-25: Cladding temperature**

Figure 3-25 shows the cladding temperature for the first 500 s of the transient. The ASYST 3.4 temperature rapidly decreases in the first 20 s of the transient, after which it stabilises and falls in between the cladding temperatures of Scenarios 2 and 3 at ~75 s. A downward trend is then observed and the temperatures of ASYST 3.4 and Scenario 2 are similar after 500 s. The trend of the cladding temperature for all three scenarios is very similar to the trend of the RPV pressure shown in Figure 3-17. Thus, a link can be drawn from the RPV pressure response which influences the RCS temperature and by extension the cladding temperature.

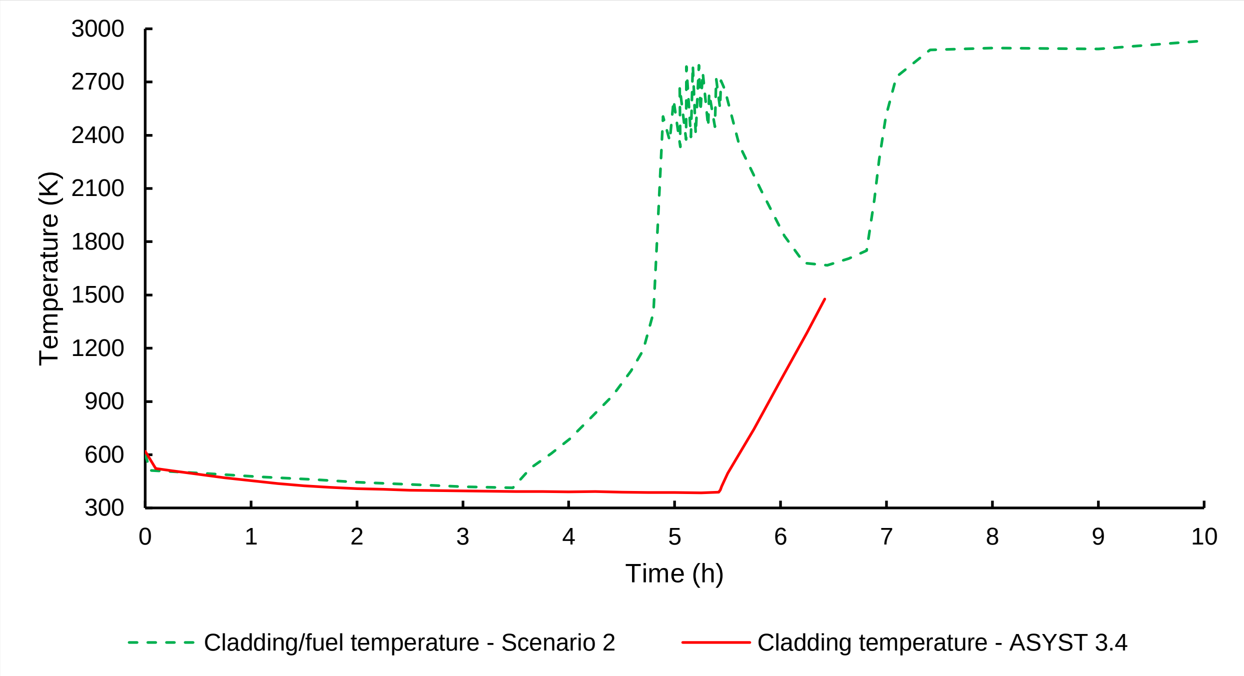


**Figure 3-26: Cladding/fuel temperature until failure**

Figure 3-26 shows the cladding/fuel temperature for Scenario 2 for 10 h and the cladding temperature of ASYST 3.4 up to the point of cladding failure. In Scenario 2 the cladding temperature starts to increase after 3.5 h due to the reduction in coolant level and the core becoming uncovered. After 4.5 h the cladding reaches a temperature of 1477 K at which point oxidation produces heat of up to 24 MW and the temperature rapidly increases. The melting point of the cladding is reached after 4.8 h at 2200 K from which point onward the maximum fuel temperature is shown. The temperature continues to increase to ~ 2700 K at 5.4 h and then decreases to ~ 1650 K after 6.3 h. However, continued oxidation of the cladding and the loss of coolable geometry results in an increase in the maximum fuel temperature to 2800 K after 7 h and a temperature of ~ 2900 K is maintained for the remainder of the 24 h transient (Skolik *et al.*, 2021).

The cladding temperature of ASYST 3.4 is lower than that of Scenario 2 during the first 3.5 h of the transient. This is most likely due to the differences in RPV pressure during this period resulting in lower RCS temperatures and lower cladding temperatures. The point where the cladding temperature starts to increase due to the reduction in coolant level occurs at 5.4 h. This is delayed by 1.9 h compared to Scenario 2. This difference can be traced back to the RPV pressure response as this resulted in lower RCS temperatures and a reduction in the boiloff rate of coolant in the RPV. A higher RCS flow is also maintained during the initial stages of the transient. From the point of the core becoming uncovered the cladding temperature steadily increases until the failure point of the cladding is reached at 1477 K after 6.42 h. Oxidation of Zr-alloy starts at 1173 K with a failure point of 1477 K due to this oxidation, according to safety standards set by the Nuclear Regulatory Commission (Yu *et al.*, 2020).

## 3.5 Conclusion

A model of one NPM was developed with a full primary loop and CNV, and a partial secondary loop and UHS pool. The model is based on data taken from the NuScale FSAR (NuScale Power LLC., 2020d, 2020c, 2020b, 2020e) and various articles from literature (Fakhraei *et al.*, 2020; Skolik *et al.*, 2021). The model is geometrically similar to a NPM and other models of an NPM. However, simplifications were made to several areas of the model. The core of the model was simplified to a three-channel model, with a hot, average, and bypass channel. No neutronic analysis was done and a predetermined power profile of the core was used. The two SG bundles were simplified to a single pipe. This is the only section of the secondary loop which is included in the model due to it being the only section which interacts with the primary loop, and inlet and outlet conditions of this section is known. Only one twelfth of the UHS pool is included as only one of twelve of the NPMs in a NPP are modelled. All additional components which are not critical for the steady state operation and transient progression of the model are excluded. This includes the DHRS and all valves of the ECCS excluding one RVV.

The model was verified for both steady state operation and a selected accident transient. Verification was done with data taken from the NuScale FSAR (NuScale Power LLC., 2020d, 2020c, 2020b, 2020e) as well as various articles in open literature (Fakhraei *et al.*, 2020; Skolik *et al.*, 2021). The steady state parameters of the model in the current study agrees with the steady state parameters given by the FSAR, except for the core inlet temperature which results in a large error in the core temperature rise. This is however acceptable because the core inlet temperature agrees with that of the study by Fakhraei *et al.* (2020), which has a similar primary coolant flow, and Skolik *et al.* (2021) was only able to achieve the core inlet temperature given by the FSAR with a lower primary coolant flow. The transient behaviour of the model in the current study is characterised by a faster decrease in RPV pressure compared to results from the FSAR and Skolik *et al.* (2021). This most likely leads to the lower RCS temperatures and subsequent lower cladding temperatures throughout the transient. These differences in RPV pressure are attributed to discrepancies in the RVV flow model, RPV and CNV dimensions and RPV and CNV initial conditions. Despite these differences, the general behaviour of the model is the same as that of Skolik *et al.* (2021), with the coolant level in the RPV gradually decreasing until the core becomes uncovered, resulting in core damage. Thus, the model is suitable for evaluating the use of ATF cladding materials.

# CHAPTER 4: RESULTS AND DISCUSSION

With the completion of the NuScale SMR reference model development and verification, the evaluation of ATF cladding materials in the NuScale SMR can be performed. Steady state performance of the NuScale SMR with ATF cladding will be evaluated. This is of interest as the primary coolant flow in the NuScale SMR is driven by natural circulation. The heat produced in the core and the heat removed by the SG creates a density difference in the riser and downcomer. Thus, the heat transfer from the nuclear fuel to the coolant through the cladding is of importance. A worst-case scenario accident transient will also be evaluated, which is the inadvertent opening of a RVV with subsequent failure of the ECCS and DHRS. This accident transient is selected as it is one of the accidents with the highest core damage frequency, even though the probability of this accident occurring is very low at ~ $10^{-11}$/reactor-year (Skolik *et al.*, 2021). ATF cladding is used with the goal of increasing the coping time and decreasing the PFCT and PCT during the transient.

Simulations of the NuScale SMR were done with Zr-alloy cladding in Chapter 3.4 to verify the model. The Zr-alloy cladding will now be replaced with FeCrAl and SiC to compare the corresponding results. Changes to the model only include the selection of another cladding material (changing the thermophysical properties) and changing the wall roughness in the fuel channels to that of the corresponding cladding material. All other aspects of the model remain the same.

## 4.1 Steady state operation

The steady state parameters of the NuScale SMR model with ATF cladding materials can be seen in Table 4-1. The parameters are compared with the corresponding parameters obtained in the simulations with Zr-alloy cladding with a percentage change calculated. The simulations were allowed to run for 10000 s to ensure a steady state condition. The core power, RPV pressure, SG inlet temperature and pressure, and the SG feedwater flow rate are used as input parameters or controlled by the reactor control system, and thus these parameters remain the same.

The core inlet and outlet temperatures for all three cladding materials remain the same, with the largest change being the core temperature rise with the FeCrAl cladding being less than 0.2 %. The SG outlet temperature showed a negligible change with the use of the ATF cladding materials. Some minor changes can be seen in the coolant flow rate which is most likely due to the changes in surface roughness of the cladding materials which were set to 1.61 µm for Zr-alloy, 4.53 µm for FeCrAl, and 1.0 µm for SiC.

The largest differences in the use of ATF cladding compared to Zr-alloy can be seen in the PCT and PFCT. These changes are due to the differences in thermophysical properties of the cladding materials shown in Figure 3-12. FeCrAl has a 2.24% decrease in PCT compared to Zr-alloy. While FeCrAl and Zr-alloy have a similar thermal conductivity at this temperature range, there is a large difference in the volumetric heat capacity of the two materials. The higher volumetric heat capacity of FeCrAl indicates the material requires more energy to achieve the same temperature as Zr-alloy. The energy remains the same between the two simulations and thus the PCT is lower in the case of FeCrAl which is a good result. SiC shows a 1.27 %

increase in the PCT compared to that of Zr-alloy. Although SiC has the highest specific heat capacity of all three cladding materials, the volumetric heat capacity is more in line with that of Zr-alloy due to the lower density of SiC compared to Zr-alloy and FeCrAl. The higher PCT is a result of the lower thermal conductivity of SiC compared to Zr-alloy, especially at high temperatures.

The PFCT with FeCrAl shows a 0.017 % or 0.17 °C increase compared to that of Zr-alloy. This is most likely because of the slightly lower thermal conductivity of FeCrAl compared to Zr-alloy. In the case of SiC, the PFCT showed an increase of 0.86 % or 8.26 °C. This is due to the large decrease in thermal conductivity of SiC compared to Zr-alloy. In general, there are no large differences in the thermal hydraulic performance of the NuScale SMR when substituting Zr-alloy cladding with FeCrAl or SiC cladding. The only change of importance is the increase in PFCT with the use of SiC cladding. It is unlikely that this small change in temperature would have a large effect on the operation of NuScale SMR. However, this should be taken into consideration when performing Multiphysics calculations of the NuScale SMR core.

**Table 4-1: ATF cladding steady state parameters.**

| Parameter | Zr-alloy | FeCrAl | % change | SiC | % change |
|---|---|---|---|---|---|
| Core thermal power (MW) | 159.00 | 159.00 | - | 159.00 | - |
| Core outlet temperature (K) | 586.73 | 586.78 | +0.008 | 586.72 | -0.002 |
| Core inlet temperature (K) | 536.24 | 536.19 | -0.009 | 536.25 | +0.002 |
| Core temperature rise (K) | 50.49 | 50.59 | +0.19 | 50.47 | -0.04 |
| SG secondary inlet temperature (K) | 421.87 | 421.87 | - | 421.87 | - |
| SG secondary outlet temperature (K) | 579.76 | 579.75 | -0.001 | 579.76 | - |
| RPV pressurizer pressure (MPa) | 12.75 | 12.75 | - | 12.75 | - |
| Normal steam pressure (MPa) | 3.51 | 3.51 | - | 3.51 | - |
| Average coolant flow rate (kg/s) | 587.31 | 586.19 | -0.19 | 587.56 | +0.042 |
| Average SG feedwater flow rate (kg/s) | 67.07 | 67.07 | - | 67.07 | - |
| Peak cladding temperature (K) | 621.27 | 607.36 | -2.24 | 629.18 | +1.27 |
| Peak fuel centreline temperature (K) | 962.83 | 963.00 | +0.017 | 971.09 | +0.86 |

## 4.2 Accident transient

In general, transient results with the two ATF claddings remain the same as the transient results with Zr-alloy cladding. The transient sequence of events shown in Table 3-16 are the same when substituting Zr-alloy cladding with FeCrAl or Sic cladding, except for the time and temperature at which core damage occurs.  The RPV and CNV pressures shown in Figure 3-17 and Figure 3-18 respectively, remains the same with FeCrAl and SiC cladding.

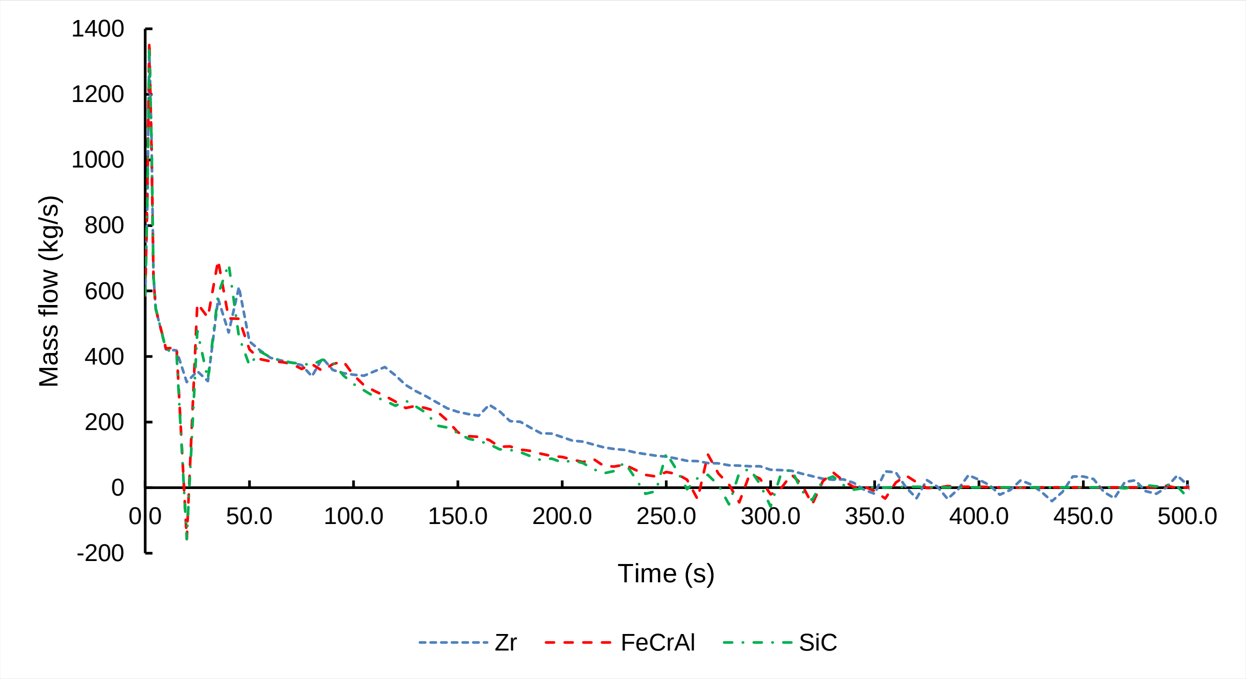


**Figure 4-1: RCS flow with ATF cladding**

The RCS flow with the three cladding materials can be seen in Figure 4-1. A decrease in the RCS flow is visible at a time of 20 s for all three cladding materials. However, where the RCS flow with Zr-alloy decreases to ~ 320 kg/s at this point, the RCS flow turns in the negative direction down to roughly negative 156 kg/s in both cases with FeCrAl and SiC cladding. After this point the RCS flow in the case of FeCrAl and SiC returns to a similar value as that of the Zr-alloy and the RCS flow in all three cases follow a similar trend. The point at which the RCS flow reaches zero and flow oscillations start is reached earlier with the two ATF claddings, with FeCrAl at 260 s and SiC at 240 s compared to Zr-alloy at 350 s. The differences in RCS flow are attributed to the differences in thermophysical properties and surface roughness of the three cladding materials. FeCrAl has a higher surface roughness compared to Zr-alloy which leads to higher flow resistance. The driving force of the natural circulation could also be reduced by the high volumetric heat capacity of FeCrAl and the low thermal conductivity of SiC. The reduction in heat transferred to the coolant could reduce the buoyancy forces which drives natural circulation. The RCS flow for all three cladding materials is roughly the same for the remainder of the transient.

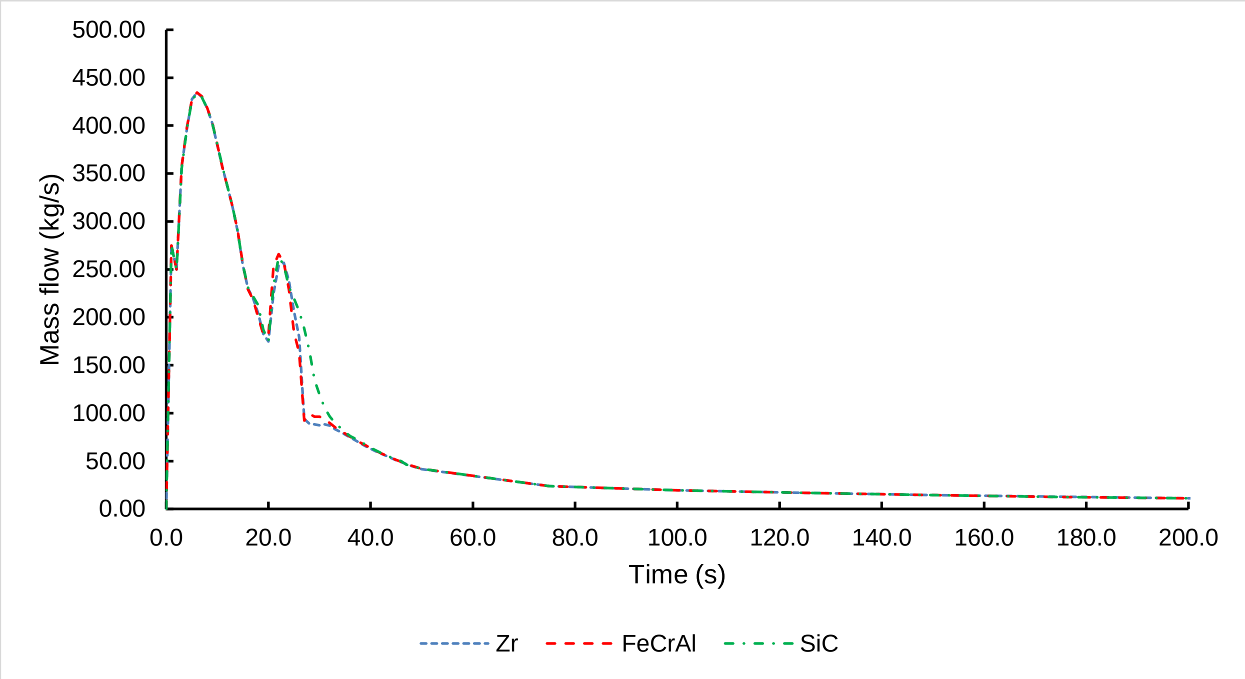


**Figure 4-2: Break flow with ATF cladding**

The break flow for all three cladding materials can be seen in Figure 4-2. All three cases are nearly the same for the first 20 s at which point they start to diverge. This coincides with the large difference seen in the RCS flow at this time. However, the values converge again at ~ 35 s and remain the same for the remainder of the transient. Similar trends were observed in the RCS temperature and cladding temperature during this period. During the interval of 20 to 35 s the difference in core inlet temperature between the three cases was less than two degrees, with the core outlet temperature having a difference of less than one degree. The maximum difference in cladding temperature during this period is also less than two degrees. After 35 s these values converge and remain similar for the remainder of the transient.

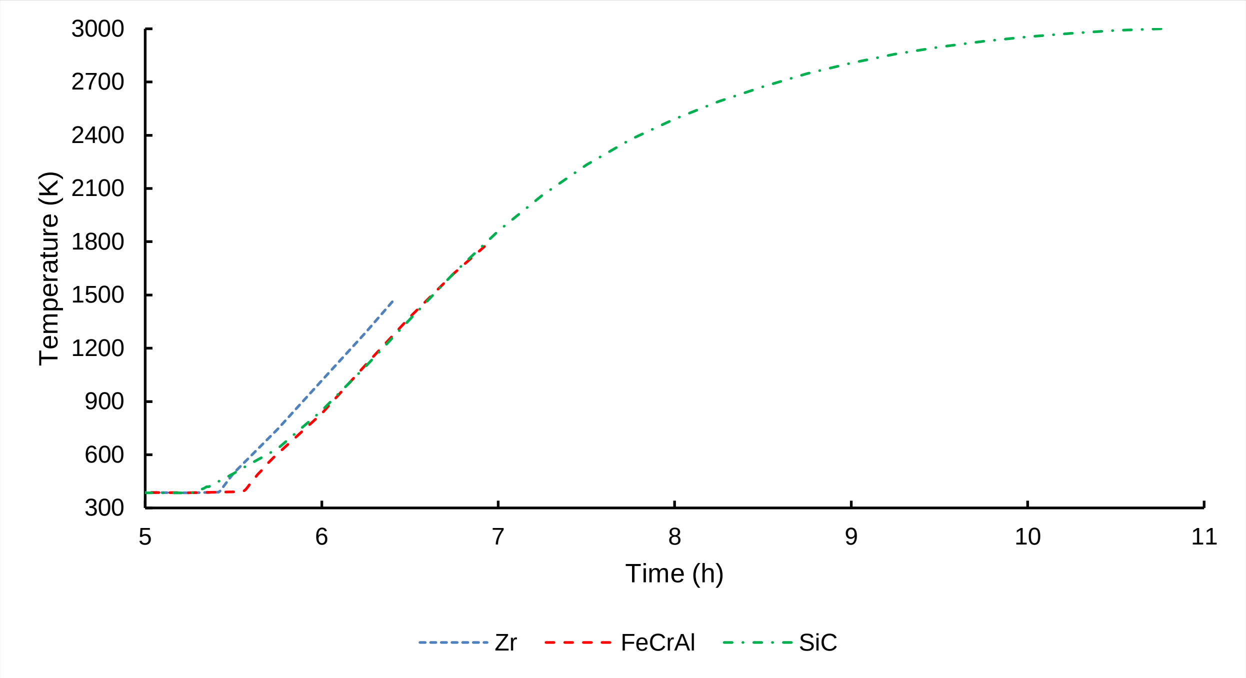


**Figure 4-3: Cladding temperature of ATF materials**

The maximum cladding temperatures for the three cladding materials up to the point of failure is shown in Figure 4-3. The temperature differences between the three cladding materials during steady state operation decreases within the first 50 s of the transient, and the temperatures are the same throughout the first five hours of the transient. The temperature increases due to the core becoming uncovered, occurred at 5.3 h for SiC, 5.4 h for Zr-alloy and 5.55 h for FeCrAl. The temperature increase in SiC starts earlier due to the maximum temperature occurring in the tenth axial node (topmost node) of the hot channel. As the coolant level decreases this is the first node to become uncovered. The maximum cladding temperature of FeCrAl occurs in the eighth axial node of the hot channel.

A discrepancy is seen in the maximum cladding temperature of Zr-alloy as this occurs in the eighth axial node of the average channel and not the hot channel as expected. This is most likely due to the coolant level being lower in the average channel than in the hot channel. A similar trend is seen in the maximum cladding temperature of FeCrAl, where the PCT is in the average channel during initial stages of the temperature increase. The PCT in the hot and average channels with FeCrAl intersect at 6.56 h and 1439 K, from which point onward the PCT is in the hot channel. In the case of Zr-alloy, the transient is terminated due to failure of the cladding before this intersection point is reached. A possible solution would be to add crossflow between the fuel channels to ensure that the coolant level is equal between the two channels.

The time of failure of Zr-alloy is at 6.42 h at a temperature of 1477 K as discussed in Section 3.4.2. The PCT with Zr-alloy in the hot channel at this point is 1441 K. The failure point of FeCrAl cladding is 6.92 h from the start of the transient at a temperature of 1773 K. This is a 0.5-hour additional grace time compared to the point of failure of Zr-alloy. It is important to note that the failure point of FeCrAl is the melting point of this material, while the failure point of Zr-alloy is 1477 K due to oxidation. Also, the point where the temperature increases due to the core being uncovered is delayed by 0.15 h, most likely due to the differences in thermophysical properties and surface roughness. In the case of SiC, the trend at which temperature increases closely follows that of FeCrAl up to the point of failure of FeCrAl. Due to the high melting point of SiC, the transient progresses past the time of failure of FeCrAl with a continued increase in cladding temperature. The failure point is reached after 10.77 h at a temperature of 3000 K. Although this temperature occurred in the tenth axial node of the hot channel, all nodes that are uncovered at this point have temperatures within ten degrees of the hottest node. The point of failure of SiC is delayed by 4.35 h compared to Zr-alloy which adds significant grace time for this ATF. In all cases the core temperature remains under the melting point of $UO_2$.

A summary of the time and temperature at which the cladding materials fail with a percentage increase in grace time, can be seen in Table 4-2. FeCrAl showed a 7.79 % increase in the grace time, which agrees with prior studies. In the study by Yu *et al.* (2020), a 8.4 % increase in grace time was seen when using FeCrAl, while SiC did not fail within the simulation time. Gurgen and Shirvan (2018) also showed that the use of FeCrAl improved grace time by 10.3 % during short term SBO and 16.4% during long term SBO accident transients. SiC improved the grace time by 67.76% due to its high melting temperature.

**Table 4-2: Cladding failure time and temperature**

| Cladding | Failure point (K) | Time to failure (h) | % increase |
|---|---|---|---|
| Zr-alloy | 1477.0 | 6.42 | - |
| FeCrAl | 1773.0 | 6.92 | 7.79 |
| SiC | 3000.0 | 10.77 | 67.76 |

## 4.3 Conclusion

Evaluation of ATF cladding in the NuScale SMR was completed at steady state operation as well as a worst-case scenario accident transient. The use of ATF cladding materials had no significant influence on the steady state performance of the NuScale SMR. The most significant change in steady state parameters was the increase in PFCT by 0.86 % with SiC cladding which should be considered in Multiphysics calculations. The use of ATF cladding also had little effect on the transient progression of the accident transient and most parameters were unchanged in the first five hours. The key advantage ATF materials provided was the increased failure temperature of the cladding. This increased the coping time of the accident by 0.5 h or 7.79 % with FeCrAl cladding and 4.35 h or 67.76 % with SiC cladding.

# CHAPTER 5: CONCLUSION

## 5.1 Conclusions

The goal of the current study was to find ways of improving safety in LWRs based on the accident that occurred at the Fukushima NPP in March 2011. Two major factors contributing to the severity of that accident was the failure of active cooling systems due to a SBO, and oxidation of the cladding material which led to hydrogen explosions. Thus, various systems and new reactor concepts designed around passive safety were considered. Various ATF cladding materials were also considered which have higher oxidation resistance and a higher melting temperature compared to Zr-alloy. A system was to be selected which enhanced the passive safety of LWRs but can still benefit from the use of ATF. The evaluation of the selected system with ATF cladding materials was performed.

The two ATF cladding materials selected for this study was FeCrAl alloy and a SiC composite. These materials are among the most prominent ATF cladding materials in nuclear research. Both materials offer a large increase in oxidation resistance compared to Zr-alloy. FeCrAl has favourable thermophysical properties compared to Zr-alloy. However, FeCrAl has a large neutron absorption cross-section which negatively impacts the neutron economy of the reactor. On the other hand, SiC has a small neutron absorption cross-section and a high melting point, while having less favourable thermophysical properties.

The NuScale SMR was selected as the system to be evaluated for this study. This reactor is a natural circulation SMR, meaning that the primary coolant flow is only driven by buoyancy forces in both steady state operation and accident scenarios. The SMR has additional safety features such as the ECCS and DHRS. The SMR was chosen as it was the furthest along in its development among other light water SMRs, and specifications of the reactor was readily available. Furthermore, although the reactor has excellent safety features and can mitigate most accident scenarios, there exists a worst-case scenario accident which has a high core damage frequency. In this case the reactor could benefit from the use of ATF cladding materials to prolong the coping time and decrease the PFCT and PCT. Thus, a thermal-hydraulic evaluation of ATF materials in the NuScale SMR was performed.

A model of the NuScale SMR was created using ASYST 3.4, which is a modified RELAP5/MOD3 code. Specifications of the NuScale SMR was taken from the NuScale FSAR and further supplemented with data from literature. The model boundary determined that a full primary loop and CNV be modelled with a partial secondary loop and UHS pool. Several simplifications were made to the model such as the core and steam generator. The model was verified for steady state operation and the selected accident transient using data from the NuScale FSAR and various articles from literature. Most steady state parameters of the current model agree with values given by the FSAR except for the core inlet temperature. However, this was found to be acceptable when comparing results with corresponding results found in literature (Fakhraei *et al.*, 2020; Skolik *et al.*, 2021).

Transient results were verified using results from the FSAR and Skolik *et al.* (2021). The current model tended to have faster depressurisation of the RPV compared to the model by Skolik *et al.* (2021), which led to lower RCS temperatures and thus lower cladding temperatures throughout the first hours of the transient. These discrepancies could be attributed to differences in the valve flow model, RPV and CNV dimensions, and initial conditions. This also resulted in a delay of where the cladding temperature started to increase due to the core being uncovered, as well as the point of failure of the cladding material. However, the behaviour of the current model during the accident transient was as expected. Therefore, the model was deemed to be suitable for use in evaluating ATF claddings in the NuScale SMR.

The majority of the steady state parameters remain the same or have negligible change when substituting Zr-alloy cladding with FeCrAl or SiC. The largest changes are seen in the PCT and PFCT. A 2.24 % decrease is seen in the PCT when using FeCrAl which might be beneficial. A 1.27 % increase is seen in the PCT when using SiC. However, SiC has the highest melting temperature of all three cladding materials considered. A negligible increase in PFCT is seen with FeCrAl. An increase of 0.86 % in PFCT is seen when using SiC. This remains well within the operational conditions for $UO_2$ fuel. However, this should be taken into consideration when performing Multiphysics calculations of the NuScale SMR core with SiC cladding.

Some differences are seen between cladding materials in the first 50 s of the transient. The RCS flow in the cases of FeCrAl and SiC show a large and sudden change in direction at ~ 20 s. However, these values quickly return to match the RCS flow trend of Zr-alloy. Minor changes are seen in the break flow and RCS temperature in the period of 20 to 35 s. These discrepancies are attributed to differences in thermophysical properties and surface roughness of the cladding materials. Negligible changes are seen in the RPV pressure, RCS temperature and cladding temperature throughout the first five hours of the transient.

The transient was set to run up to the point of failure of the cladding materials. This occurred at a time of 6.42 h from the start of the transient for Zr-alloy. The failure temperature of Zr-alloy was set to 1477 K due to oxidation. The key advantage in the use of ATF cladding materials was the increased failure temperature. The failure temperature of FeCrAl is 1773 K which was reached at a time of 6.92 h, providing an additional 0.5 h or 7.79 % grace time. The failure temperature of SiC is 3000 K, which resulted in failure at 10.77 h, adding a significant 4.35 h or 67.76 % to the grace time.

Thus, the use of ATF cladding materials in the NuScale SMR had little effect on the steady state operation of the reactor. A slight increase was seen in the PFCT while using SiC cladding in steady state conditions, which should be considered when performing Multiphysics calculations. The behaviour of the reactor remained the same during the accident transient when using ATF cladding, except for some discrepancies within the first 50 s. Zr-alloy failed after a period of 6.42 hours. The higher failure point of ATF claddings prolonged the grace time. SiC had the largest effect, prolonging the grace time by 4.35 h or 67.76 %. SiC also has many other advantages not evaluated in the current study such as an increased oxidation resistance and a decrease in the thermal neutron absorption cross-section. It is therefore recommended to use SiC as ATF cladding in the NuScale SMR to enhance the safety during accident scenarios.

## 5.2 Recommendations

Based on the current study the following recommendations are made for future studies:

### 5.2.1 Improvements to the current model

Oxidation of Zr-alloy cladding is a large risk to the safety of LWRs. Not only does the oxidation reaction produce hydrogen which could lead to hydrogen explosions, but the reaction also produces a large amount of heat leading to a reduction in the grace time during accidents (Skolik *et al.*, 2021). The current model can be improved by adding models for oxidation and melting of fuel elements.

The current model uses a predetermined power profile for the power produced by the core for both the steady state operation and the selected accident transient. This could be improved by using the reactor kinetics model of ASYST 3.4, which would have a better prediction of the actual core power.

Discrepancies were seen in the location of the PCT and PFCT. At the point of failure of Zr-alloy the maximum temperatures were seen in the average channel and not the hot channel as expected. This is most likely due to a difference in the coolant level between the hot and average channel. A possible solution would be to add crossflow between the fuel channels.

As seen in Figure 4-1, the RCS flow in the case of FeCrAl and SiC shows a large and sudden change in the flow direction at a time of ~ 20 seconds. This anomaly is not fully understood and should be investigated in future studies.

Discrepancies were seen in the SA factor of the SG heat structure. Future studies should investigate methods to address this issue, such as improving the estimation of the SA factor and using heat transfer coefficients better suited for helical coil SGs. Other modelling approaches such as a zig-zag pattern pipe or a vertical straight pipe should also be investigated.

It is unclear whether the radiation heat transfer model was active in the CNV during the steady state operation of the reactor. In future studies it can be ensured that the radiation heat transfer model is active and the effects of this on the operation of the reactor could be evaluated.

Future studies should include a more detailed investigation into the heat transfer coefficients on the outer surface of the cladding such that a comparison can be made between various cladding materials.

The current model was purpose built to perform evaluation of the steady state operation of the reactor, along with one worst-case scenario accident transient. The model can be expanded to evaluate other accident transients. This may require the addition of the DHRS and the remaining ECCS valves. The model boundary in the current study determined that only a partial secondary loop is necessary. This can be expanded to form the complete secondary loop. This may also require expansion of the control system, with the refinement of areas such as the core power, pressurizer heating elements and various trip signals being necessary.

Results from the current study showed an increase of the PFCT while using SiC cladding under steady state conditions. It is also known that the microscopic thermal neutron absorption cross sections of the three cladding materials in the current study are different, which influences the neutron economy of the reactor (Mustafa, 2021). Due to these factors, the core power distribution used in the current study might not be accurate when substituting cladding materials. For this reason, it is recommended that Multiphysics calculations of the NuScale SMR core with the selected cladding materials be performed to determine a more accurate core power distribution for each cladding material. Multiphysics calculations can also be used to perform neutronic, thermal-hydraulic and burnup analyses.

The thermophysical properties of Helium was taken from EES in the current study. However, it was assumed that the thermophysical properties are valid for a temperature range of 300 K to 3300 K, even though it is stated that the equations of state for Helium in EES is only valid up to 1500 K. This was done as there were no data sets available for the thermophysical properties of Helium over the required temperature range and at the required pressure. Future studies can focus on the development of equations of state for helium over larger temperature ranges.

### 5.2.2 Thermal-hydraulic codes

Results from the current study was generated by running the input code with ASYST 3.4.0 (Build 03/2019). This included all results shown in Chapter 3 and 4. However, most of the model development was done using ASYST-RHYS 4.1.0 (Build 12/2018). The RHYS GUI simplified the building of the model by providing “drag and drop” functionality for adding components. With ASYST integration, simulations could be run from within RHYS. RHYS also provided features such as real-time visualisation of variables in component volumes, and plotting of data while simulations are running.

The steady state operation of the NuScale SMR was accurately predicted by ASYST-RHYS 4.1.0. However, several thermal-hydraulic errors occurred during the accident transient. The first error occurred at a time of $\sim$ 20 s from the start of the transient. This is during depressurisation of the RPV before the RPV and CNV pressure equalises. The error would occur in the top volume of the pressurizer, which is connected to the CNV through the RVV. The error message indicated that the liquid pressure coefficient of expansion (kappaf) was negative. Various methods of resolving this issue were tried, such as changing the valve parameters, changing the CNV pressure, changing the nodalisation of the pressurizer and decreasing the minimum and maximum time step. The only way this error could be circumvented was increasing the coolant level in the pressurizer from 50 % to 100 %. This allowed the transient to progress past the initial depressurisation of the RPV.

Other errors occurred due to flow oscillations. As was seen in Figure 3-21, the RCS flow would gradually decrease during the first 350 s of the transient. Once the RCS flow reached zero, flow oscillations would start and would periodically occur up to a time of 1500 s. In the case of simulations done with ASYST-RHYS 4.1.0, the RCS flow would have a more gradual decrease, reaching zero at a time of 600 – 700 s from the start of the transient. Flow oscillations would start at this point. However, these oscillations were much larger in both amplitude and frequency compared to the results shown in Figure 3-21. The oscillations also progressed past 1500 s unlike the results shown in Figure 3-21. The amplitude of the oscillations was initially ~ 100 kg/s, but would gradually increase throughout the transient to beyond 500 kg/s. The simulation would typically fail within the first two hours of the transient. The error message given in most cases was a thermodynamic property error, or more specifically a vapor phase property error. The location of the error was at the coolant level which typically was in the upper riser or middle riser at the time of the failure. As with the previous error, various methods were used for resolving the error such as different nodalisation and decreasing the minimum and maximum time step. However, these errors were not resolved.

The errors discussed in this section prohibited the completion of the current study using ASYST-RHYS 4.1.0. Simulations were completed with ASYST 3.4.0. The input file generated by ASYST-RHYS 4.1.0 was used in ASYST 3.4.0 with no changes made to the file. No errors occurred in the simulations with ASYST 3.4.0, and the results of these simulations are shown in Chapter 3 and 4. Further investigation of the discrepancies between ASYST 3.4.0 and ASYST-RHYS 4.1.0 is required.

# BIBLIOGRAPHY


Allison, C.M., Hohorst, J.K., Ezzidi, A., Naitoh, M. and Pericas, R. (2020), "Development and Preliminary Assessment of the new ASYST - ISA Integral Analysis BEPU Code using the PBF SFD-ST Bundle Heating and Melting Experiment , a Typical BWR Under Fukushima-Daiichi-Accident-Like Thermal Hydraulic Conditions and PWR for a Steam Lin", *Proceedings of ICAPP 2020 15-19 March 2020 – Abu Dhabi (UAE)*, No. December, pp. 1–13.

Ansys. (2023), "CFX", available at: https://www.ansys.com/products/fluids/ansys-cfx.

Arblaster, J.W. (2013), "Thermodynamic properties of zirconium", *Calphad: Computer Coupling of Phase Diagrams and Thermochemistry*, Elsevier, Vol. 43, pp. 32–39, doi: 10.1016/j.calphad.2013.07.015.

Butt, H.N., Ilyas, M., Ahmad, M. and Aydogan, F. (2016), "Assessment of passive safety system of a Small Modular Reactor (SMR)", *Annals of Nuclear Energy*, Vol. 98, pp. 191–199, doi: 10.1016/j.anucene.2016.07.018.

Deng, Y., Shirvan, K., Wu, Y. and Su, G. (2018), "Probabilistic view of SiC/SiC composite cladding failure based on full core thermo-mechanical response", *Journal of Nuclear Materials*, Elsevier B.V, Vol. 507, pp. 24–37, doi: 10.1016/j.jnucmat.2018.04.023.

El-Sahlamy, N.M., Hassan, M.I., Khedr, A.S. and D'Auria, F. (2022), "Study of rod ejection accident at hot zero power condition in a PWR using RELAP5", *Progress in Nuclear Energy*, Elsevier Ltd, Vol. 144 No. December 2021, p. 104100, doi: 10.1016/j.pnucene.2021.104100.

Energy Education Canada. (2018), "Boiling water reactor - Energy Education", available at: https://energyeducation.ca/encyclopedia/Boiling_water_reactor (accessed 15 June 2021).

Erfaninia, A., Hedayat, A., Mirvakili, S.M. and Nematollahi, M.R. (2017), "Neutronic-thermal hydraulic coupling analysis of the fuel channel of a new generation of the small modular pressurized water reactor including hexagonal and square fuel assemblies using MCNP and CFX", *Progress in Nuclear Energy*, Elsevier Ltd, Vol. 98, pp. 213–227, doi: 10.1016/j.pnucene.2017.03.025.

F-Chart Software. (2023), "Engineering Equation Solver", available at: https://fchartsoftware.com/ees/.

Fakhraei, A., Faghihi, F., Amin-mozafari, M. and Sadegh-noedoost, A. (2020), "Annals of Nuclear Energy Safety analysis of an advanced passively-cooled small modular reactor during station blackout scenarios and normal operation with", *Annals of Nuclear Energy*, Elsevier Ltd, Vol. 143, p. 107470, doi: 10.1016/j.anucene.2020.107470.

Fakhraei, A., Faghihi, F., Rabiee, A. and Safarinia, M. (2021), "Coolant flow rate instability during extended station blackout accident in NuScale SMR: Two approaches for improving flow stability", *Progress in Nuclear Energy*, Elsevier Ltd, Vol. 131 No. November 2020, p. 103602, doi: 10.1016/j.pnucene.2020.103602.

Gurgen, A. and Shirvan, K. (2018), "Estimation of coping time in pressurized water reactors for near term accident tolerant fuel claddings", *Nuclear Engineering and Design*, Vol. 337 No. 2013, pp. 38–50, doi: 10.1016/j.nucengdes.2018.06.020.

He, S., Cai, J., Chen, Z. and Liu, R. (2019), "Thermal hydraulic analysis of accident tolerant fuels for Reactivity-Initiated-Accident in PWR with different coolant channel geometries", *Nuclear Engineering and Design*, Elsevier, Vol. 351 No. May, pp. 131–142, doi: 10.1016/j.nucengdes.2019.05.028.

Hoffer, N. V., Sabharwall, P. and Anderson, N. (2011), "Modeling a Helical-coil Steam Generator in RELAP5-3D for the Next Generation Nuclear Plant", No. January, pp. 1–53.

IAEA, I.A.E.A. (2015), "The Fukushima Daiichi Accident Report by the Director General", *Director General*, pp. 1–222.

Idaho National Engineering Laboratory. (1995), *RELAP5 / MOD3 Code Manual*, Vol. 5.

Idaho National Laboratory. (2023), "RELAP5-3D", available at: https://relap53d.inl.gov/SitePages/Home.aspx.

Information Systems Laboratories. (2022), "SNAP".

Innovative Systems Software. (2023), "ASYST", available at: http://www.relap.com/software.html.

Jung, J., An, S.M.O., Ha, K.S. and Kim, H.Y. (2015), "Evaluation of heat-flux distribution at the inner and outer reactor vessel walls under the in-vessel retention through external reactor vessel cooling condition", Vol. 7, pp. 3–10, doi: 10.1016/j.net.2014.11.005.

Katoh, Y., Ozawa, K., Shih, C., Nozawa, T., Shinavski, R.J., Hasegawa, A. and Snead, L.L. (2014), "Continuous SiC fiber, CVI SiC matrix composites for nuclear applications: Properties and irradiation effects", *Journal of Nuclear Materials*, Elsevier B.V., Vol. 448 No. 1–3, pp. 448–476, doi: 10.1016/j.jnucmat.2013.06.040.

Kim, D.J. and Choi, D.J. (1997), "Microhardness and surface roughness of silicon carbide by chemical vapour deposition", *Journal of Materials Science Letters*, Vol. 16 No. 4, pp. 286–289, doi: 10.1023/A:1018549001328.

Lee, D., Elward, B., Brooks, P., Umretiya, R., Rojas, J., Bucci, M., Rebak, R.B., *et al.* (2021), “Enhanced flow boiling heat transfer on chromium coated zircaloy-4 using cold spray technique for accident tolerant fuel (ATF) materials”, *Applied Thermal Engineering*, Elsevier Ltd, Vol. 185 No. November 2020, p. 116347, doi: 10.1016/j.applthermaleng.2020.116347.

Lee, S.K., Liu, M., Brown, N.R., Terrani, K.A., Blandford, E.D., Ban, H., Jensen, C.B., *et al.* (2019), “Comparison of steady and transient flow boiling critical heat flux for FeCrAl accident tolerant fuel cladding alloy, Zircaloy, and Inconel”, *International Journal of Heat and Mass Transfer*, Elsevier Ltd, Vol. 132, pp. 643–654, doi: 10.1016/j.ijheatmasstransfer.2018.11.141.

Los Alamos National Laboratory. (2023), “The MCNP® Code”, available at: https://mcnp.lanl.gov/.

Marcel, C.P., Acuña, F.M., Zanocco, P.G. and Delmastro, D.F. (2013), “Stability of self-pressurized, natural circulation, low thermo-dynamic quality, nuclear reactors: The stability performance of the CAREM-25 reactor”, *Nuclear Engineering and Design*, Vol. 265, pp. 232–243, doi: 10.1016/j.nucengdes.2013.08.057.

Marcel, C.P., Furci, H.F., Delmastro, D.F. and Masson, V.P. (2013), “Phenomenology involved in self-pressurized, natural circulation, low thermo-dynamic quality, nuclear reactors: The thermal-hydraulics of the CAREM-25 reactor”, *Nuclear Engineering and Design*, Elsevier B.V., Vol. 254, pp. 218–227, doi: 10.1016/j.nucengdes.2012.09.005.

Mascari, F., Vella, G., Woods, B.G., Welter, K., Pottorf, J., Young, E., Adorni, M., *et al.* (2011), “Sensitivity analysis of the MASLWR helical coil steam generator using TRACE”, *Nuclear Engineering and Design*, Elsevier B.V., Vol. 241 No. 4, pp. 1137–1144, doi: 10.1016/j.nucengdes.2010.05.002.

Moorthi, A., Kumar Sharma, A. and Velusamy, K. (2018), “A review of sub-channel thermal hydraulic codes for nuclear reactor core and future directions”, *Nuclear Engineering and Design*, Elsevier, Vol. 332 No. March, pp. 329–344, doi: 10.1016/j.nucengdes.2018.03.012.

Mustafa, S.S. (2021), “Investigation of the safety features of advanced PWR assembly using SiC , Zr , FeCrAl and SS - 310 as cladding materials”, pp. 1–19.

Naitoh, M., Hosoda, S. and Allison, C.M. (2005), “Assessment of Water Injection As Severe Accident Management Using Sampson Code”, *13 Th ICONE, Beijing, China*.

NuScale Power LLC. (2019), “Enclosure 1 : ‘ Subchannel Analysis Methodology ’, TR-0915-17564-P-A , Revision 2 , proprietary version Enclosure 2 : ‘ Subchannel Analysis Methodology ’, TR-0915-17564-NP-A , Revision 2 , nonproprietary version Enclosure 3 : Affidavit of Thomas A . Bergm”.

NuScale Power LLC. (2020a), “NuScale Standard Plant Design Certification Application: Introduction and General Description of the Plant”, No. July.

NuScale Power LLC. (2020b), “NuScale Standard Plant Design Certification Application: Chapter 4 Reactor”, No. July.

NuScale Power LLC. (2020c), “NuScale Standard Plant Design Certification Application: Chapter 5 Reactor Coolant System and Connecting System Part 2 – Tier 2 Revision 5”, No. July.

NuScale Power LLC. (2020d), “NuScale Standard Plant Design Certification Application: Chapter 6 Engineered Safety Features”, No. July, pp. 97–117, doi: 10.14325/mississippi/9781617031243.003.0006.

NuScale Power LLC. (2020e), “NuScale Standard Plant: Design Certification Application: Chapter 15: Transient and Accident Analyses, Rev. 5, July 2020”, No. July.

Popov, S.G., Carbajo, J.J., Ivanov, V.K. and Yoder, G.L. (2000), “Thermophysical Properties of MOX and UO2 Fuels Including the Effects of Irradiation”, Vol. 0 No. 1, pp. 1–14.

Porhemmat, M.H., Faghihi, F. and Rabiee, A. (2016), “Primary loop analysis for a PWR contains Passive Core Cooling System; LOCA and clad rising temperature”, *Annals of Nuclear Energy*, Elsevier Ltd, Vol. 91, pp. 8–21, doi: 10.1016/j.anucene.2015.09.031.

Prabhanjan, D.G., Raghavan, G.S.V. and Rennie, T.J. (2002), “Comparison of heat transfer rates between a straight tube heat exchanger and a helically coiled heat exchanger”, *International Communications in Heat and Mass Transfer*, Vol. 29 No. 2, pp. 185–191, doi: 10.1016/S0735-1933(02)00309-3.

Qiu, B., Wang, J., Deng, Y., Wang, M., Wu, Y. and Qiu, S.Z. (2020), “A review on thermohydraulic and mechanical-physical properties of SiC, FeCrAl and Ti3SiC2 for ATF cladding”, *Nuclear Engineering and Technology*, Elsevier Ltd, Vol. 52 No. 1, pp. 1–13, doi: 10.1016/j.net.2019.07.030.

Reyes, J.N., Groome, J., Woods, B.G., Young, E., Abel, K., Yao, Y. and Yoo, Y.J. (2007), “Testing of the multi-application small light water reactor (MASLWR) passive safety systems”, *Nuclear Engineering and Design*, Vol. 237 No. 18, pp. 1999–2005, doi: 10.1016/j.nucengdes.2007.01.014.

Skolik, K., Allison, C., Hohorst, J., Malicki, M., Perez-Ferragut, M., Pieńkowski, L. and Trivedi, A. (2021), “Analysis of loss of coolant accident without ECCS and DHRS in an integral pressurized water reactor using RELAP/SCDAPSIM”, *Progress in Nuclear Energy*, Vol. 134 No. December 2020, doi: 10.1016/j.pnucene.2021.103648.

Special Metals Corporation. (2019), “Inconel® Alloy 690”, available at:

https://www.specialmetals.com/documents/technical-bulletins/inconel/inconel-alloy-690.pdf.

Sun, D.C., Li, Y., Xi, Z., Zan, Y.F., Li, P.Z. and Zhuo, W.B. (2017), “Experimental evaluation of safety performance of emergency passive residual heat removal system in HPR1000”, *Nuclear Engineering and Design*, Vol. 318, pp. 54–60, doi: 10.1016/j.nucengdes.2017.04.003.

Umretiya, R. V., Vargas, S., Galeano, D., Mohammadi, R., Castano, C.E. and Rojas, J. V. (2020), “Effect of surface characteristics and environmental aging on wetting of Cr-coated Zircaloy-4 accident tolerant fuel cladding material”, *Journal of Nuclear Materials*, Elsevier B.V, Vol. 535, p. 152163, doi: 10.1016/j.jnucmat.2020.152163.

US NRC. (2008), “TRACE V5.0 Theory Manual”, p. 696.

US NRC. (2014), “Material Property Correlations: Comparisons between FRAPCON-3.5, FRAPTRAN-1.5, and MATPRO. NUREG/CR-7024 Revision 1. PNNL-19417 Revision 1”.

US NRC. (2020), “Standard design approval for the NuScale power plant based on the NuScale standard plant design certification application”, No. Dc.

Wu, D., Gui, M., Zhang, R., Zhang, J., Ye, T., Yang, H., Peng, J., *et al.* (2020), “Preliminary optimization of emergency core cooling system with accident-tolerant fuels”, *Annals of Nuclear Energy*, Vol. 142, doi: 10.1016/j.anucene.2020.107411.

Yu, H., Chen, Z. and Cai, J. (2020), “Accident tolerant fuel thermal hydraulic behaviors evaluation during loss of coolant accident in CPR1000”, *Annals of Nuclear Energy*, Elsevier Ltd, Vol. 139, p. 107273, doi: 10.1016/j.anucene.2019.107273.

Zhao, Y., Peng, M. and Xia, G. (2020), “Safety evaluation of the flashing-driven natural circulation IPWR against Loss-of-Feedwater accident”, *Annals of Nuclear Energy*, Elsevier Ltd, Vol. 142, p. 107408, doi: 10.1016/j.anucene.2020.107408.

Zhao, Y., Peng, M., Xu, Y., Xia, G. and Wang, C. (2019), “Analysis of the transient performance of the flashing-driven natural circulation IPWR”, *Annals of Nuclear Energy*, Elsevier Ltd, Vol. 132, pp. 381–390, doi: 10.1016/j.anucene.2019.04.059.

## APPENDIX A: ASYST 3.4 INPUT FOR NUSCALE SMR MODEL

```
$-------------------MISCELLANENOUS Cards-----------------
100 new transnt
102 si si
104 ncmpress
105 20.0 80.0
110 air
115 1.0
120 180010000 -0.5 h2o Primary 0
121 601010000 0.0 h2o CNV 0
122 210010000 0.0 h2o SG2 0
$-------------------TIME STEP Cards-----------------
201 96400.0 1.0e-10 0.1 39 10 100 500
$-------------------Trip Component Cards-----------------
*-----------------Trip Component 401-----------------*
401 p 145020000 lt null 0 12.75e6 n
*-----------------Trip Component 402-----------------*
402 time 0 gt null 0 10000.0 l
*-----------------Trip Component 403-----------------*
403 p 145020000 gt null 0 11.03e6 n
*-----------------Trip Component 404-----------------*
404 p 145020000 gt null 0 11.03e6 n
*-----------------Trip Component 405-----------------*
405 time 0 gt null 0 1.0e9 n
*-----------------Trip Component 601-----------------*
601 401 and 403 n
$-------------------Hydraulic Components Cards-----------------
-
*-----------------ANNULUS 150-----------------*
1500000 annu150 annulus
1500001 10
1500101 2.9798 10
1500201 0.0 9
1500301 0.764 10
1500401 0.0 10
1500501 0.0 10
1500601 -90.0 10
1500801 0.3e-6 0.066 10
1500901 2.0 2.0 9
1501001 100100 10
1501101 100 9
1501201 3 12.75e6 580.0 0.0 0.0 0.0 10
1501300 0
1501301 0.0 0.0 0.0 9
*-----------------ANNULUS 160-----------------*
1600000 annu001 annulus
1600001 1
1600101 1.826 1
1600301 2.87 1
1600401 0.0 1
1600501 0.0 1
1600601 -90.0 1
1600801 15.0e-6 0.0 1
1601001 100000 1
1601201 3 12.76e6 531.0 0.0 0.0 0.0 1
*-----------------ANNULUS 170-----------------*
```

```
1700000 annu002 annulus
1700001 1
1700101 1.82593 1
1700301 2.4 1
1700401 0.0 1
1700501 0.0 1
1700601 90.0 1
1700801 15.0e-6 0.0 1
1701001 100000 1
1701201 3 12.76e6 531.0 0.0 0.0 0.0 1
*-----------------BRANCH 140-----------------*
1400000 brch019 branch
1400001 3 0
1400101 5.704 0.382 0.0 0.0 90.0 0.382 15.0e-6 0.0 0
1400200 3 12.75e6 587.0
1401101 135050002 140010001 0.0 0.0 0.0 100
1402101 140010001 150010001 0.0 0.0 0.0 100
1403101 140010002 145010001 0.0 0.0 0.0 100
1401201 0.0 0.0 0.0
1402201 0.0 0.0 0.0
1403201 0.0 0.0 0.0
*-----------------PIPE 124-----------------*
1240000 pipe001 pipe
1240001 12
1240101 0.024586 12
1240201 0.024586 11
1240301 0.2 12
1240401 0.0 12
1240501 0.0 12
1240601 90.0 12
1240801 1.61e-6 0.011 12
1240901 1.5 1.5 11
1241001 100100 12
1241101 0 11
1241201 3 12.5e+6 580.0 0.0 0.0 0.0 12
1241300 0
1241301 0.0 0.0 0.0 11
*-----------------PIPE 125-----------------*
1250000 pipe125 pipe
1250001 12
1250101 0.8851 12
1250201 0.8851 11
1250301 0.2 12
1250401 0.0 12
1250501 0.0 12
1250601 90.0 12
1250801 1.61e-6 0.011 12
1250901 1.5 1.5 11
1251001 100100 12
1251101 0 11
1251201 3 12.5e+6 580.0 0.0 0.0 0.0 12
1251300 0
1251301 0.0 0.0 0.0 11
*-----------------PIPE 126-----------------*
1260000 pipe001 pipe
1260001 12
1260101 0.084 12
1260201 0.084 11
1260301 0.2 12
1260401 0.0 12
```

```
1260501 0.0 12
1260601 90.0 12
1260801 1.61e-6 0.22 12
1260901 1.5 1.5 11
1261001 100000 12
1261101 0 11
1261201 3 12.5e+6 500.0 0.0 0.0 0.0 12
1261300 0
1261301 0.0 0.0 0.0 11
*-----------------PIPE 130-----------------*
1300000 pipe001 pipe
1300001 1
1300101 2.313 1
1300301 2.87 1
1300401 0.0 1
1300501 0.0 1
1300601 90.0 1
1300801 15.0e-6 0.0 1
1301001 0 1
1301201 3 12.75e6 580.0 0.0 0.0 0.0 1
*-----------------PIPE 135-----------------*
1350000 pipe135 pipe
1350001 5
1350101 1.43 5
1350201 0.0 4
1350301 1.528 5
1350401 0.0 5
1350501 0.0 5
1350601 90.0 5
1350801 15.0e-6 0.0 5
1350901 1.65 1.65 4
1351001 100000 5
1351101 100 4
1351201 3 12.75e6 580.0 0.0 0.0 0.0 5
1351300 0
1351301 0.0 0.0 0.0 4
*-----------------PIPE 145-----------------*
1450000 pipe003 pipe
1450001 6
1450101 3.354 1
1450102 5.704 2
1450103 5.704 5
1450104 3.8276 6
1450201 0.0 5
1450301 0.525 5
1450302 0.67 6
1450401 0.0 6
1450501 0.0 6
1450601 90.0 6
1450801 15.0e-6 0.0 6
1450901 1.0 1.0 5
1451001 1000 6
1451101 0 5
1451201 3 12.75e6 600.0 0.0 0.0 0.0 3
1451202 4 12.75e6 600.0 1.0 0.0 0.0 6
1451300 0
1451301 0.0 0.0 0.0 5
*-----------------PIPE 220-----------------*
2200000 pipe001 pipe
2200001 10
```

```
2200101 0.23198 10
2200201 0.0 9
2200301 2.42 10
2200401 0.0 10
2200501 0.0 10
2200601 16.56626 10
2200801 0.3e-6 0.01463 10
2200901 0.05 0.5 9
2201001 100 10
2201101 0 9
2201201 4 3.45e6 421.0 1.0 0.0 0.0 10
2201300 0
2201301 0.0 0.0 0.0 9
*-----------------PIPE 501-----------------*
5010000 pipe003 pipe
5010001 7
5010101 8.43 1
5010102 2.82 2
5010103 9.12 3
5010104 8.25 6
5010105 14.69 7
5010201 0.0 6
5010301 0.35 1
5010302 2.9 2
5010303 2.87 3
5010304 3.82 5
5010305 3.677 6
5010306 4.0 7
5010401 0.0 7
5010501 0.0 7
5010601 90.0 7
5010801 15.0e-6 0.0 7
5010901 1.0 1.0 6
5011001 0 7
5011101 0 6
5011201 4 5.0e3 300.0 1.0 0.0 0.0 7
5011300 0
5011301 0.0 0.0 0.0 6
*-----------------PIPE 601-----------------*
6010000 pipe004 pipe
6010001 8
6010101 567.74 8
6010201 0.0 7
6010301 3.82 2
6010302 3.25 3
6010303 2.87 4
6010304 3.82 6
6010305 3.667 7
6010306 4.0 8
6010401 0.0 8
6010501 0.0 8
6010601 90.0 8
6010801 15.0e-6 0.0 8
6010901 1.0 1.0 7
6011001 0 8
6011101 0 7
6011201 3 100.0e3 310.0 0.0 0.0 0.0 7
6011202 4 100.0e3 310.0 0.5 0.0 0.0 8
6011300 0
6011301 0.0 0.0 0.0 7
```

```
*-----------------PIPE 602-----------------*
6020000 pipe004 pipe
6020001 4
6020101 567.74 4
6020201 0.0 3
6020301 5.0 4
6020401 0.0 4
6020501 0.0 4
6020601 90.0 4
6020801 0.0 0.0 4
6020901 0.0 0.0 3
6021001 0 4
6021101 0 3
6021201 4 100.0e3 300.0 1.0 0.0 0.0 4
6021300 0
6021301 0.0 0.0 0.0 3
*-----------------SINGLE JUNCTION 1-----------------*
0010000 sngj001 sngljun
0010101 130010002 135010001 0.0 0.0 0.0 0
0010201 0 0.0 0.0 0.0
*-----------------SINGLE JUNCTION 13-----------------*
0130000 sngj003 sngljun
0130101 180010002 124010001 0.0 2.0 2.0 100
0130201 0 0.0 0.0 0.0
*-----------------SINGLE JUNCTION 14-----------------*
0140000 sngj004 sngljun
0140101 124120002 130010001 0.0 2.0 2.0 100
0140201 0 0.0 0.0 0.0
*-----------------SINGLE JUNCTION 15-----------------*
0150000 sngj005 sngljun
0150101 180010002 125010001 0.0 2.0 2.0 100
0150201 0 0.0 0.0 0.0
*-----------------SINGLE JUNCTION 16-----------------*
0160000 sngj006 sngljun
0160101 125120002 130010001 0.0 2.0 2.0 100
0160201 0 0.0 0.0 0.0
*-----------------SINGLE JUNCTION 17-----------------*
0170000 sngj007 sngljun
0170101 180010002 126010001 0.0 2.0 2.0 100
0170201 0 0.0 0.0 0.0
*-----------------SINGLE JUNCTION 18-----------------*
0180000 sngj008 sngljun
0180101 126120002 130010001 0.0 2.0 2.0 100
0180201 0 0.0 0.0 0.0
*-----------------SINGLE JUNCTION 2-----------------*
0020000 sngj002 sngljun
0020101 160010002 170010002 0.0 0.0 0.0 0
0020201 0 0.0 0.0 0.0
*-----------------SINGLE JUNCTION 202-----------------*
2020000 sngj001 sngljun
2020101 230010002 235010001 0.0 0.0 0.0 0
2020201 0 0.0 0.0 0.0
*-----------------SINGLE JUNCTION 21-----------------*
0210000 sngj001 sngljun
0210101 150100002 160010001 0.0 0.0 0.0 0
0210201 0 0.0 0.0 0.0
*-----------------SINGLE JUNCTION 22-----------------*
0220000 sngj001 sngljun
0220101 170010001 180010002 0.0 1.0 1.0 100
0220201 0 0.0 0.0 0.0
```

```
*-----------------SINGLE JUNCTION 651-----------------*
6510000 sngj004 sngljun
6510101 601080002 602010001 0.0 0.0 0.0 0
6510201 0 0.0 0.0 0.0
*-----------------SINGLE VOLUME 180-----------------*
1800000 sgvl001 snglvol
1800101 4.719 0.5 0.0 0.0 90.0 0.5 15.0e-6 0.0 0
1800200 3 12.5e6 580.0
*-----------------SINGLE VOLUME 210-----------------*
2100000 sgvl006 snglvol
2100101 0.23198 1.0 0.0 0.0 0.0 0.0 0.0 0.0 0
2100200 3 3.45e6 421.0
*-----------------SINGLE VOLUME 230-----------------*
2300000 sgvl019 snglvol
2300101 0.23198 1.0 0.0 0.0 0.0 0.0 0.0 0.0 0
2300200 3 3.45e6 421.0
*-----------------TMDP-VOLUME 205-----------------*
2050000 tmdvol tmdpvol
2050101 0.1 1.0 0.0 0.0 0.0 0.0 0.0 0.0 0
2050200 3
2050201 0.0 3.45e+6 421.872
*-----------------TMDP-VOLUME 235-----------------*
2350000 tmdvol tmdpvol
2350101 01.0 1.0 0.0 0.0 0.0 0.0 0.0 0.0 0
2350200 4
2350201 0.0 3.45e+6 421.0 0.0
*-----------------TMDP-JUNCTION 201-----------------*
2010000 tmdj001 tmdpjun
2010101 205010002 210010001 0.1
2010200 1 0 time 210010000
2010201 0.0 67.068 0.0 0.0
2010202 10000.0 67.068 0.0 0.0
2010203 10000.0 0.0 0.0 0.0
*-----------------VALVE 19-----------------*
0190000 valve valve
0190101 220100002 230010001 0.0 0.0 0.0 0
0190201 0 0.0 0.0 0.0
0190300 trpvlv
0190301 404
*-----------------VALVE 3-----------------*
0030000 valve valve
0030101 145060002 501070001 0.016 0.0 0.0 110
0030201 0 0.0 0.0 0.0
0030300 trpvlv
0030301 402
*-----------------VALVE 6-----------------*
0060000 valve valve
0060101 210010002 220010001 0.016 0.0 0.0 100
0060201 0 0.0 0.0 0.0
0060300 trpvlv
0060301 404
$-------------------Heat Structure Cards-----------------
*-----------------Heat Structure 10-----------------*
10010000 10 10 2 0 0.0 0
10010100 0 1
10010101 4 0.00405765
10010102 2 0.0041402
10010103 3 0.0047498
10010201 1 4
10010202 -2 6
```

```
10010203 -3 9
10010301 1.0 4
10010302 0.0 6
10010303 0.0 9
10010401 600.0 10
10010501 0 0 0 1 52.8 10
10010601 124020000 10000 1 1 52.8 10
10010701 10 0.0012805 0.0 0.0 1
10010702 10 0.0027109 0.0 0.0 2
10010703 10 0.0033032 0.0 0.0 3
10010704 10 0.0036504 0.0 0.0 4
10010705 10 0.0038240 0.0 0.0 5
10010706 10 0.0037527 0.0 0.0 6
10010707 10 0.0036882 0.0 0.0 7
10010708 10 0.0032973 0.0 0.0 8
10010709 10 0.0026523 0.0 0.0 9
10010710 10 0.0013306 0.0 0.0 10
10010800 0
10010801 0.0 10.0 10.0 0.0 0.0 0.0 0.0 1.0 10
10010900 0
10010901 0.01248 10.0 10.0 0.0 0.0 0.0 0.0 1.0 10
*-----------------Heat Structure 11-----------------*
10011000 10 10 2 0 0.0 0
10011100 0 1
10011101 4 0.00405765
10011102 2 0.0041402
10011103 3 0.0047498
10011201 1 4
10011202 -2 6
10011203 -3 9
10011301 1.0 4
10011302 0.0 6
10011303 0.0 9
10011401 600.0 10
10011501 0 0 0 1 1900.8 10
10011601 125020000 10000 1 1 1900.8 10
10011701 10 0.042144 0.0 0.0 1
10011702 10 0.089219 0.0 0.0 2
10011703 10 0.10871 0.0 0.0 3
10011704 10 0.12014 0.0 0.0 4
10011705 10 0.12585 0.0 0.0 5
10011706 10 0.12350 0.0 0.0 6
10011707 10 0.12138 0.0 0.0 7
10011708 10 0.10852 0.0 0.0 8
10011709 10 0.087291 0.0 0.0 9
10011710 10 0.043791 0.0 0.0 10
10011800 0
10011801 0.0 10.0 10.0 0.0 0.0 0.0 0.0 1.0 10
10011900 0
10011901 0.01248 10.0 10.0 0.0 0.0 0.0 0.0 1.0 10
*-----------------Heat Structure 12-----------------*
10012000 10 2 2 0 0.007315 0
10012100 0 1
10012101 1 0.00795
10012201 5 1
10012301 0.0 1
10012401 500.0 2
10012501 220100000 -10000 1 1 6125.0 10
10012601 150010000 10000 1 1 6125.0 10
10012701 0 0.0 0.0 0.0 10
```

```
10012800 0
10012801 0.0 10.0 10.0 0.0 0.0 0.0 0.0 1.0 10
10012900 0
10012901 0.0 10.0 10.0 0.0 0.0 0.0 0.0 1.0 10
*-----------------Heat Structure 13-----------------*
10013000 10 5 2 0 0.55741 0
10013100 0 1
10013101 4 0.60821
10013201 4 4
10013301 0.0 4
10013401 550.0 5
10013501 135010000 0 1 1 0.764 1
10013502 135010000 0 1 1 0.764 2
10013503 135020000 0 1 1 0.764 3
10013504 135020000 0 1 1 0.764 4
10013505 135030000 0 1 1 0.764 5
10013506 135030000 0 1 1 0.764 6
10013507 135040000 0 1 1 0.764 7
10013508 135040000 0 1 1 0.764 8
10013509 135050000 0 1 1 0.764 9
10013510 135050000 0 1 1 0.764 10
10013601 150100000 -10000 1 1 0.764 10
10013701 0 0.0 0.0 0.0 10
10013800 0
10013801 0.0 10.0 10.0 0.0 0.0 0.0 0.0 1.0 10
10013900 0
10013901 0.0 10.0 10.0 0.0 0.0 0.0 0.0 1.0 10
*-----------------Heat Structure 14-----------------*
10014000 1 5 2 0 0.55741 0
10014100 0 1
10014101 4 0.60821
10014201 4 4
10014301 0.0 4
10014401 550.0 5
10014501 130010000 10000 1 1 2.87 1
10014601 160010000 10000 1 1 2.87 1
10014701 0 0.0 0.0 0.0 1
10014800 0
10014801 0.0 10.0 10.0 0.0 0.0 0.0 0.0 1.0 1
10014900 0
10014901 0.0 10.0 10.0 0.0 0.0 0.0 0.0 1.0 1
*-----------------Heat Structure 15-----------------*
10015000 1 2 2 0 0.0 0
10015100 0 1
10015101 1 0.01
10015201 4 1
10015301 1.0 1
10015401 580.0 2
10015501 0 0 0 1 50.0 1
10015601 145020000 0 1 1 50.0 1
10015701 1 1.0 0.0 0.0 1
10015800 0
10015801 0.0 10.0 10.0 0.0 0.0 0.0 0.0 1.0 1
10015900 0
10015901 0.0 10.0 10.0 0.0 0.0 0.0 0.0 1.0 1
*-----------------Heat Structure 16-----------------*
10016000 1 2 2 0 1.219 0
10016100 0 1
10016101 1 1.337
10016201 4 1
```

```
10016301 0.0 1
10016401 550.0 2
10016501 180010000 0 1 1 0.5 1
10016601 501020000 0 1 1 0.5 1
10016701 0 0.0 0.0 0.0 1
10016800 0
10016801 0.0 10.0 10.0 0.0 0.0 0.0 0.0 1.0 1
10016900 0
10016901 0.0 10.0 10.0 0.0 0.0 0.0 0.0 1.0 1
*-----------------Heat Structure 17-----------------*
10017000 1 2 2 0 1.219 0
10017100 0 1
10017101 1 1.337
10017201 4 1
10017301 0.0 1
10017401 550.0 2
10017501 170010000 0 1 1 2.4 1
10017601 501020000 0 1 1 2.4 1
10017701 0 0.0 0.0 0.0 1
10017800 0
10017801 0.0 10.0 10.0 0.0 0.0 0.0 0.0 1.0 1
10017900 0
10017901 0.0 10.0 10.0 0.0 0.0 0.0 0.0 1.0 1
*-----------------Heat Structure 18-----------------*
10018000 1 2 2 0 1.321 0
10018100 0 1
10018101 1 1.432
10018201 4 1
10018301 0.0 1
10018401 550.0 2
10018501 160010000 0 1 1 2.87 1
10018601 501030000 0 1 1 2.87 1
10018701 0 0.0 0.0 0.0 1
10018800 0
10018801 0.0 10.0 10.0 0.0 0.0 0.0 0.0 1.0 1
10018900 0
10018901 0.0 10.0 10.0 0.0 0.0 0.0 0.0 1.0 1
*-----------------Heat Structure 19-----------------*
10019000 5 2 2 0 1.321 0
10019100 0 1
10019101 1 1.432
10019201 4 1
10019301 0.0 1
10019401 550.0 2
10019501 150100000 -10000 1 1 0.764 5
10019601 501040000 0 1 1 0.764 1
10019602 501040000 0 1 1 0.764 2
10019603 501040000 0 1 1 0.764 3
10019604 501040000 0 1 1 0.764 4
10019605 501040000 0 1 1 0.764 5
10019701 0 0.0 0.0 0.0 5
10019800 0
10019801 0.0 10.0 10.0 0.0 0.0 0.0 0.0 1.0 5
10019900 0
10019901 0.0 10.0 10.0 0.0 0.0 0.0 0.0 1.0 5
*-----------------Heat Structure 20-----------------*
10020000 5 2 2 0 1.321 0
10020100 0 1
10020101 1 1.432
10020201 4 1
```

```
10020301 0.0 1
10020401 550.0 2
10020501 150050000 -10000 1 1 0.764 5
10020601 501050000 0 1 1 0.764 1
10020602 501050000 0 1 1 0.764 2
10020603 501050000 0 1 1 0.764 3
10020604 501050000 0 1 1 0.764 4
10020605 501050000 0 1 1 0.764 5
10020701 0 0.0 0.0 0.0 5
10020800 0
10020801 0.0 10.0 10.0 0.0 0.0 0.0 0.0 1.0 5
10020900 0
10020901 0.0 10.0 10.0 0.0 0.0 0.0 0.0 1.0 5
*-----------------Heat Structure 21-----------------*
10021000 1 2 2 0 1.321 0
10021100 0 1
10021101 1 1.432
10021201 4 1
10021301 0.0 1
10021401 550.0 2
10021501 140010000 0 1 1 0.382 1
10021601 501060000 0 1 1 0.382 1
10021701 0 0.0 0.0 0.0 1
10021800 0
10021801 0.0 10.0 10.0 0.0 0.0 0.0 0.0 1.0 1
10021900 0
10021901 0.0 10.0 10.0 0.0 0.0 0.0 0.0 1.0 1
*-----------------Heat Structure 22-----------------*
10022000 6 2 2 0 1.321 0
10022100 0 1
10022101 1 1.432
10022201 4 1
10022301 0.0 1
10022401 550.0 2
10022501 145010000 10000 1 1 0.525 6
10022601 501060000 0 1 1 0.525 1
10022602 501060000 0 1 1 0.525 2
10022603 501060000 0 1 1 0.525 3
10022604 501060000 0 1 1 0.525 4
10022605 501060000 0 1 1 0.525 5
10022606 501060000 0 1 1 0.525 6
10022701 0 0.0 0.0 0.0 6
10022800 0
10022801 0.0 10.0 10.0 0.0 0.0 0.0 0.0 1.0 6
10022900 0
10022901 0.0 10.0 10.0 0.0 0.0 0.0 0.0 1.0 6
*-----------------Heat Structure 23-----------------*
10023000 1 2 2 0 1.638 0
10023100 0 1
10023101 1 1.715
10023201 4 1
10023301 0.0 1
10023401 300.0 2
10023501 501010000 0 1 1 0.35 1
10023601 601030000 0 1 1 0.35 1
10023701 0 0.0 0.0 0.0 1
10023800 0
10023801 0.0 10.0 10.0 0.0 0.0 0.0 0.0 1.0 1
10023900 0
10023901 0.0 10.0 10.0 0.0 0.0 0.0 0.0 1.0 1
```

```
*-----------------Heat Structure 24-----------------*
10024000 1 2 2 0 1.638 0
10024100 0 1
10024101 1 1.715
10024201 4 1
10024301 0.0 1
10024401 300.0 2
10024501 501020000 0 1 1 2.9 1
10024601 601030000 0 1 1 2.9 1
10024701 0 0.0 0.0 0.0 1
10024800 0
10024801 0.0 10.0 10.0 0.0 0.0 0.0 0.0 1.0 1
10024900 0
10024901 0.0 10.0 10.0 0.0 0.0 0.0 0.0 1.0 1
*-----------------Heat Structure 25-----------------*
10025000 1 2 2 0 2.165 0
10025100 0 1
10025101 1 2.248
10025201 4 1
10025301 0.0 1
10025401 300.0 2
10025501 501030000 0 1 1 2.87 1
10025601 601040000 0 1 1 2.87 1
10025701 0 0.0 0.0 0.0 1
10025800 0
10025801 0.0 10.0 10.0 0.0 0.0 0.0 0.0 1.0 1
10025900 0
10025901 0.0 10.0 10.0 0.0 0.0 0.0 0.0 1.0 1
*-----------------Heat Structure 26-----------------*
10026000 2 2 2 0 2.162 0
10026100 0 1
10026101 1 2.248
10026201 4 1
10026301 0.0 1
10026401 300.0 2
10026501 501040000 10000 1 1 3.82 2
10026601 601050000 10000 1 1 3.82 2
10026701 0 0.0 0.0 0.0 2
10026800 0
10026801 0.0 10.0 10.0 0.0 0.0 0.0 0.0 1.0 2
10026900 0
10026901 0.0 10.0 10.0 0.0 0.0 0.0 0.0 1.0 2
*-----------------Heat Structure 27-----------------*
10027000 1 2 2 0 2.162 0
10027100 0 1
10027101 1 2.248
10027201 4 1
10027301 0.0 1
10027401 300.0 2
10027501 501060000 0 1 1 3.667 1
10027601 601070000 0 1 1 3.667 1
10027701 0 0.0 0.0 0.0 1
10027800 0
10027801 0.0 10.0 10.0 0.0 0.0 0.0 0.0 1.0 1
10027900 0
10027901 0.0 10.0 10.0 0.0 0.0 0.0 0.0 1.0 1
*-----------------Heat Structure 28-----------------*
10028000 1 2 2 0 2.162 0
10028100 0 1
10028101 1 2.248
```

```
10028201 4 1
10028301 0.0 1
10028401 300.0 2
10028501 501070000 0 1 1 4.0 1
10028601 601080000 0 1 1 4.0 1
10028701 0 0.0 0.0 0.0 1
10028800 0
10028801 0.0 10.0 10.0 0.0 0.0 0.0 0.0 1.0 1
10028900 0
10028901 0.0 10.0 10.0 0.0 0.0 0.0 0.0 1.0 1
*-----------------Heat Structure 29-----------------*
10029000 12 2 2 0 0.9398 0
10029100 0 1
10029101 1 0.9906
10029201 4 1
10029301 0.0 1
10029401 550.0 2
10029501 126010000 10000 1 1 0.2 12
10029601 170010000 0 1 1 0.2 1
10029602 170010000 0 1 1 0.2 2
10029603 170010000 0 1 1 0.2 3
10029604 170010000 0 1 1 0.2 4
10029605 170010000 0 1 1 0.2 5
10029606 170010000 0 1 1 0.2 6
10029607 170010000 0 1 1 0.2 7
10029608 170010000 0 1 1 0.2 8
10029609 170010000 0 1 1 0.2 9
10029610 170010000 0 1 1 0.2 10
10029611 170010000 0 1 1 0.2 11
10029612 170010000 0 1 1 0.2 12
10029701 0 0.0 0.0 0.0 12
10029800 0
10029801 0.0 10.0 10.0 0.0 0.0 0.0 0.0 1.0 12
10029900 0
10029901 0.0 10.0 10.0 0.0 0.0 0.0 0.0 1.0 12
*-----------------Heat Structure 30-----------------*
10030000 12 2 2 0 0.0050419 0
10030100 0 1
10030101 1 0.0061214
10030201 3 1
10030301 0.0 1
10030401 500.0 2
10030501 124010000 10000 1 1 5.0 12
10030601 126010000 10000 1 1 5.0 12
10030701 0 0.0 0.0 0.0 12
10030800 0
10030801 0.0 10.0 10.0 0.0 0.0 0.0 0.0 1.0 12
10030900 0
10030901 0.0 10.0 10.0 0.0 0.0 0.0 0.0 1.0 12
*-----------------Heat Structure 31-----------------*
10031000 12 2 2 0 0.0050419 0
10031100 0 1
10031101 1 0.0061214
10031201 3 1
10031301 0.0 1
10031401 500.0 2
10031501 125010000 10000 1 1 180.0 12
10031601 126010000 10000 1 1 180.0 12
10031701 0 0.0 0.0 0.0 12
10031800 0
```

```
10031801 0.0 10.0 10.0 0.0 0.0 0.0 0.0 1.0 12
10031900 0
10031901 0.0 10.0 10.0 0.0 0.0 0.0 0.0 1.0 12
$-------------------Thermal Propertie Cards-----------------
*-----------------Thermal Propertie 1-----------------*
20100100 tbl/fctn 1 -1
20100101 300.0 8.790
20100102 400.0 7.620
20100103 500.0 6.697
20100104 600.0 5.952
20100105 700.0 5.337
20100106 800.0 4.824
20100107 900.0 4.388
20100108 1000.0 4.015
20100109 1100.0 3.693
20100110 1200.0 3.414
20100111 1300.0 3.173
20100112 1400.0 2.967
20100113 1500.0 2.793
20100114 1600.0 2.651
20100115 1700.0 2.540
20100116 1800.0 2.460
20100117 1900.0 2.409
20100118 2000.0 2.387
20100119 2100.0 2.392
20100120 2200.0 2.422
20100121 2300.0 2.475
20100122 2400.0 2.549
20100123 2500.0 2.641
20100124 2600.0 2.748
20100125 2700.0 2.869
20100126 2800.0 3.000
20100127 2900.0 3.140
20100128 3000.0 3.286
20100129 3100.0 3.436
20100151 2.593e6
20100152 2.889e6
20100153 3.068e6
20100154 3.183e6
20100155 3.257e6
20100156 3.303e6
20100157 3.329e6
20100158 3.342e6
20100159 3.349e6
20100160 3.355e6
20100161 3.365e6
20100162 3.384e6
20100163 3.414e6
20100164 3.461e6
20100165 3.526e6
20100166 3.615e6
20100167 3.728e6
20100168 3.868e6
20100169 4.038e6
20100170 4.238e6
20100171 4.470e6
20100172 4.735e6
20100173 5.034e6
20100174 5.365e6
20100175 5.731e6
```

```
20100176 6.129e6
20100177 6.559e6
20100178 7.019e6
20100179 7.508e6
*-----------------Thermal Propertie 2-----------------*
20100200 tbl/fctn 1 1
20100201 300.0 0.1574
20100202 1500.0 0.48
20100203 3300.0 0.8336
20100251 300.0 16512.0
20100252 500.0 9945.0
20100253 1500.0 3328.0
20100254 3300.0 1514.0
*-----------------Thermal Propertie 3-----------------*
20100300 tbl/fctn 1 1
20100301 300.0 12.68
20100302 400.0 14.04
20100303 500.0 15.29
20100304 600.0 16.49
20100305 700.0 17.67
20100306 800.0 18.88
20100307 900.0 20.17
20100308 1000.0 21.58
20100309 1100.0 23.16
20100310 1200.0 24.96
20100311 1300.0 27.03
20100312 1400.0 29.4
20100313 1500.0 32.12
20100351 300.0 1.84e6
20100352 400.0 1.98e6
20100353 640.0 2.17e6
20100354 1090.0 2.46e6
20100355 1093.0 3.29e6
20100356 1113.0 3.87e6
20100357 1133.0 4.03e6
20100358 1153.0 4.72e6
20100359 1173.0 5.35e6
20100360 1193.0 5.05e6
20100361 1213.0 4.06e6
20100362 1233.0 3.08e6
20100363 1248.0 2.34e6
20100364 2099.0 2.34e6
*-----------------Thermal Propertie 4-----------------*
20100400 tbl/fctn 1 1
20100401 273.15 40.707
20100402 323.15 40.848
20100403 373.15 40.707
20100404 423.15 40.565
20100405 473.15 40.075
20100406 523.15 39.512
20100407 573.15 38.617
20100408 623.15 37.822
20100409 673.15 36.880
20100410 723.15 35.813
20100411 773.15 34.810
20100412 823.15 33.827
20100413 873.15 32.744
20100414 923.15 31.458
20100415 973.15 29.234
20100416 1023.15 26.576
```

```
20100417 1073.15 26.148
20100418 1123.15 25.868
20100419 1173.15 26.504
20100420 1223.15 27.028
20100421 1273.15 27.52
20100422 1323.15 28.013
20100423 1373.15 28.492
20100424 1423.15 28.999
20100425 1473.15 29.602
20100426 1523.15 30.033
20100427 1573.15 30.611
20100428 1623.15 31.117
20100429 1673.15 31.652
20100430 1723.15 32.131
20100451 298.15 3.193e6
20100452 323.15 3.562e6
20100453 373.15 3.741e6
20100454 423.15 3.897e6
20100455 473.15 4.066e6
20100456 523.15 4.183e6
20100457 573.15 4.342e6
20100458 623.15 4.462e6
20100459 673.15 4.636e6
20100460 723.15 4.833e6
20100461 773.15 5.041e6
20100462 823.15 5.291e6
20100463 873.15 5.603e6
20100464 887.27 5.694e6
20100465 921.78 5.95e6
20100466 953.15 6.294e6
20100467 976.68 6.595e6
20100468 1003.35 7.291e6
20100469 1004.91 7.773e6
20100470 1030.01 12.853e6
20100471 1059.82 7.722e6
20100472 1086.48 5.005e6
20100473 1100.60 5.237e6
20100474 1173.15 5.356e6
20100475 1223.15 5.428e6
20100476 1273.15 5.512e6
20100477 1323.15 5.585e6
20100478 1373.15 5.663e6
20100479 1423.15 5.729e6
20100480 1473.15 5.797e6
20100481 1523.15 5.858e6
20100482 1573.15 5.937e6
20100483 1623.15 6.007e6
20100484 1673.15 6.074e6
20100485 1723.15 6.144e6
20100486 1773.15 5.962e6
*-----------------Thermal Propertie 5-----------------*
20100500 tbl/fctn 1 1
20100501 373.15 13.5
20100502 473.15 15.4
20100503 573.15 17.3
20100504 673.15 19.1
20100505 773.15 21.0
20100506 873.15 22.9
20100507 973.15 24.8
20100508 1073.15 26.6
```

```
20100509 1173.15 28.5
20100510 1273.15 30.1
20100551 373.15 3857490.0
20100552 473.15 4070430.0
20100553 573.15 4299750.0
20100554 673.15 4512690.0
20100555 773.15 4733820.0
20100556 873.15 4946760.0
20100557 973.15 5167890.0
20100558 1073.15 5389020.0
20100559 1173.15 5601960.0
20100560 1273.15 5823090.0
*-----------------Thermal Propertie 6-----------------*
20100600 tbl/fctn 1 1
20100601 300.0 12.21
20100602 350.0 12.86
20100603 400.0 13.51
20100604 450.0 14.16
20100605 500.0 14.80
20100606 550.0 15.43
20100607 600.0 16.06
20100608 650.0 16.69
20100609 700.0 17.31
20100610 750.0 17.93
20100611 800.0 18.54
20100612 850.0 19.15
20100613 900.0 19.76
20100614 950.0 20.35
20100615 1000.0 20.95
20100616 1050.0 21.54
20100617 1100.0 22.12
20100618 1150.0 22.70
20100619 1200.0 23.28
20100620 1250.0 23.85
20100621 1300.0 24.42
20100622 1350.0 24.98
20100623 1400.0 25.54
20100624 1450.0 26.09
20100625 1500.0 26.64
20100626 1550.0 27.18
20100627 1600.0 27.72
20100628 1650.0 28.26
20100629 1700.0 28.79
20100630 1750.0 29.31
20100631 1800.0 29.84
20100651 300.0 3.44e6
20100652 325.0 3.54e6
20100653 350.0 3.63e6
20100654 375.0 3.70e6
20100655 400.0 3.77e6
20100656 425.0 3.83e6
20100657 450.0 3.89e6
20100658 475.0 3.95e6
20100659 500.0 4.01e6
20100660 525.0 4.08e6
20100661 550.0 4.16e6
20100662 575.0 4.26e6
20100663 600.0 4.37e6
20100664 625.0 4.50e6
20100665 650.0 4.64e6
```

```
20100666 675.0 4.82e6
20100667 700.0 5.02e6
20100668 725.0 5.25e6
20100669 750.0 5.51e6
20100670 771.0 5.75e6
20100671 772.0 7.06e6
20100672 773.0 6.7e6
20100673 774.0 6.49e6
20100674 775.0 6.34e6
20100675 780.0 5.91e6
20100676 785.0 5.69e6
20100677 790.0 5.53e6
20100678 795.0 5.42e6
20100679 800.0 5.33e6
20100680 825.0 5.03e6
20100681 850.0 4.87e6
20100682 875.0 4.75e6
20100683 900.0 4.67e6
20100684 925.0 4.60e6
20100685 950.0 4.55e6
20100686 975.0 4.51e6
20100687 1000.0 4.47e6
20100688 1025.0 5.45e6
20100689 1050.0 4.42e6
20100690 1100.0 4.39e6
20100691 1150.0 4.38e6
20100692 1200.0 4.38e6
20100693 1300.0 4.42e6
20100694 1400.0 4.54e6
20100695 1500.0 4.73e6
20100696 1600.0 5.02e6
20100697 1700.0 5.41e6
20100698 1800.0 5.92e6
*-----------------Thermal Propertie 7-----------------*
20100700 tbl/fctn 1 1
20100701 300.0 10.55
20100702 359.01 11.68
20100703 478.56 11.34
20100704 559.27 11.07
20100705 677.29 10.79
20100706 758.07 10.07
20100707 877.6 9.81
20100708 959.11 9.26
20100709 1078.63 9.11
20100710 1159.34 8.89
20100711 1278.89 8.56
20100712 3000.0 8.56
20100751 300.0 1.75e6
20100752 405.2 2.23e6
20100753 506.16 2.5e6
20100754 606.87 2.67e6
20100755 707.48 2.8e6
20100756 808.03 2.91e6
20100757 908.53 3.0e6
20100758 1009.0 3.08e6
20100759 1109.43 3.14e6
20100760 1207.64 3.21e6
20100761 1308.05 3.26e6
20100762 1410.67 3.31e6
20100763 1508.83 3.35e6
```

```
20100764 1609.19 3.39e6
20100765 1709.53 3.42e6
20100766 1783.14 3.45e6
20100767 1907.98 3.47e6
20100768 2010.54 3.5e6
20100769 2110.83 3.51e6
20100770 2206.67 3.52e6
20100771 2309.19 3.53e6
20100772 2407.25 3.54e6
20100773 3000.0 3.54e6
$-------------------General Table Cards-----------------
*-----------------General Table 1-----------------*
20200100 power 601
20200101 0.0 0.0
20200102 0.0 800.0e3
*-----------------General Table 10-----------------*
20201000 power 402
20201001 0.0000 159.0e6
20201002 5.0 159.0e6
20201003 5.14 136.22e6
20201004 5.23 116.60e6
20201005 5.27 97.30e6
20201006 5.35 78.31e6
20201007 5.44 59.01e6
20201008 5.48 49.52e6
20201009 5.53 39.39e6
20201010 5.61 34.01e6
20201011 5.74 28.64e6
20201012 5.87 25.16e6
20201013 6.39 21.36e6
20201014 7.08 16.61e6
20201015 8.24 15.66e6
20201016 9.4 14.71e6
20201017 10.73 14.08e6
20201018 12.54 13.13e6
20201019 15.38 12.18e6
20201020 17.66 11.87e6
20201021 19.98 11.23e6
20201022 30.04 9.97e6
20201023 40.02 8.70e6
20201024 49.91 8.07e6
20201025 145.5 5.94e6
20201026 436.4 3.95e6
20201027 727.3 3.48e6
20201028 1382.0 2.94e6
20201029 1891.0 2.68e6
20201030 2618.0 2.38e6
20201031 3491.0 2.15e6
20201032 4436.0 1.98e6
20201033 5455.0 1.89e6
20201034 6691.0 1.86e6
20201035 9164.0 1.83e6
20201036 11273.0 1.77e6
20201037 13763.0 1.71e6
20201038 16946.0 1.64e6
20201039 21527.0 1.52e6
20201040 28655.0 1.35e6
20201041 36073.0 1.18e6
20201042 43127.0 1.01e6
20201043 50327.0 0.96e6
```

```
20201044 57527.0 0.91e6
20201045 64655.0 0.85e6
20201046 71855.0 0.82e6
20201047 79273.0 0.75e6
20201048 86255.0 0.72e6
$-------------------PLOT Cards-----------------
20300010 mflowj 1000000 1 mflowj 220010000 1
20300020 p 145060000 1 p 501070000 1
20300030 httemp 1000807 1 httemp 1000907 1
$-------------------ADDITIONAL PLOTS Cards------------------
20800001 httemp 1000501
20800002 httemp 1000507
20800003 httemp 1000701
20800004 httemp 1000707
20800005 httemp 1000801
20800006 httemp 1000807
20800007 httemp 1000901
20800008 httemp 1000907
20800009 httemp 1001001
20800010 httemp 1001007
20800011 httemp 1100501
20800012 httemp 1100507
20800013 httemp 1100701
20800014 httemp 1100707
20800015 httemp 1100801
20800016 httemp 1100807
20800017 httemp 1100901
20800018 httemp 1100907
20800019 httemp 1101001
20800020 httemp 1101007
20800021 httemp 2400102
```